Beam asymmetry in the reaction channel $\gamma p \to \eta \Delta^+$ at GlueX

A Thesis

Submitted to the Faculty of Graduate Studies and Research

in Partial Fulfillment of the Requirements

for the Degree of

Doctor of Philosophy

in

Physics

University of Regina

by

Varun Neelamana

Regina, Saskatchewan

August, 2024

UNIVERSITY OF REGINA

FACULTY OF GRADUATE STUDIES AND RESEARCH

SUPERVISORY AND EXAMINING COMMITTEE

Varun Neelamana, candidate for the degree of **Doctor of Philosophy in Physics,** has presented a thesis titled, ***Beam asymmetry in the reaction channel γp→ηΔ + at Glue X,*** in an oral examination held on **June 3, 2024**. The following committee members have found the thesis acceptable in form and content, and that the candidate demonstrated satisfactory knowledge of the subject material.

External Examiner:	Dr. Dan Watts, University of York
Supervisor:	Dr. Zisis Papandreou, Department of Physics
Committee Member:	Dr. George Lolos, Department of Physics
Committee Member:	Dr. Garth Huber, Department of Physics
Committee Member:	Dr. Justin R. Stevens, Adjunct Professor, Department of Physics
Committee Member:	Dr. Joyce McBeth, Department of Geology
Chair of Defense:	Dr. Chris Oriet, Faculty of Graduate Studies and Research

ABSTRACT

Photoproduction mechanisms studied in the GlueX experiment allows the mapping of light mesons in unprecedented detail with particular interest in exotic meson candidates. This is achieved by impinging an 8.2-8.8 GeV linearly polarized photon beam on a liquid hydrogen target. The measurement of beam asymmetry Σ will help constrain quasi-particle t-channel exchange processes using Regge theory. Understanding the photoproduction exchange mechanisms is a crucial ingredient in establishing hybrid and exotic photoproduced light meson states. Σ is extracted from the azimuthal angular distribution between the meson production plane and the polarized photon beam. In particular, we will report results on the beam asymmetry measurements for η in the reaction γ p $\rightarrow \eta\ \Delta^+$. This reaction with a recoiling Δ^+ will allow for comparison and validation of theoretical calculations and provide additional validation of the η asymmetry with a recoiling proton. The different isospin of the Δ^+ imposes additional restrictions that further constrain allowed Regge exchanges. The results were similar to η-proton i.e $\Sigma \approx 1$ but showed a deviation from theoretical models of the $\eta - \Delta^+$ especially towards higher t values. This may help guide modifications to these models for production and exchange processes involving η meson.

ACKNOWLEDGMENTS

I would like to acknowledge and give my warmest thanks to my supervisor Dr. Zisis Papandreou who made this work possible. His guidance and advice carried me through all the stages of my thesis work.

I would also like to thank Dr. Jon Zarling who provided his invaluable expertise and support throughout my work.

I also want to express my thanks to members of Gluex collaboration for their technical support on my study.

I would like to thank members of my PhD committee for their valuable feedback and guidance.

To all my friends and colleagues at University of Regina, I'm grateful to each of you for a memorable time spent and making me feel home away from home especially during my initial years of Ph.D.

Lastly, I would also like to give special thanks to my wife and my family for their continuous support and understanding when undertaking my research and writing my thesis.

Dedicated to my family

Contents

List of Figures

List of Tables

List of Acronyms/Abbreviations

ADC	Analog-toDigital Converter
BCAL	Barrel Calorimeter
CALWG	Calorimetry Working Group
CDC	Central Drift Chamber
CEBAF	Continuous Electron Beam Acclerator facility
CL	Confidence level
DIRC	Detection of Internally Reflected Cherenkov light
FCAL	Forward Calorimeter
FDC	Forward calorimeter
FP	Front panel
GTP	Global Trigger Processor
JLab	Thomas Jefferson National Accelerator Facility
JPAC	Joint Physics Analysis Center
KinFit	Kinematic Fit
LED	Light Emitting Diode
LQCD	Lattice Quantum Chromodynamics
LV	Low Voltage
MC	Monte Carlo
MM	Missing Mass
PDF	Probability Density Function
PMT	Photomultiplier Tube
PS	Pair Spectrometer
PSPP	Pedestal Subtracted Pulse Peak
QCD	Quantum Chromodynamics
QED	Quantum Electrodynamics

SDME	Spin Density Matrix Element
SiPM	Silicon Photomultiplier
SM	Standard Model
ST	Start Counter
TAGH	Tagger Hodoscope
TAGM	Tagger Microscope
TOF	Time Of Flight
TPOL	Triplet Polarimeter
VME	Versa Module Eurocard

Chapter 1

Introduction

The search for fundamental constituents of matter and their interaction has been a long quest in subatomic physics. The previous century saw technological advancements like particle accelerators which helped in this endeavor. Although this quest continues, collisions of accelerated highly energetic particles have shed light on understanding the force that binds particles like protons and neutrons inside a nucleus of an atom with the exchange of a pion particle. This strong force is a result of interactions between fundamental particles called quarks and gluons. Quarks are the constituents of hadrons e.g., (proton,neutron) having three quarks, mesons e.g., (pion) having two quarks. Gluons act as a "glue" in binding these quarks. States that do not consist of only two or three quark states and cannot be described by the current quark model are called as exotic.

The purpose of Gluonic Excitation (GlueX) experiment at Thomas Jefferson National Accelerator Facility (JLab) in Newport News, Virginia, USA, is to study the interactions between the quarks and gluons and search for evidence of exotic mesons [1]. Studying simple mesons and known resonances is therefore one among the initial steps towards GlueX's main objectives, along with improving the matching between simulation and data for simple reactions. It is difficult and time consuming to precisely calculate the detector acceptance. So, initially, we extracted physics quantities like beam asymmetry which cancels out the detector acceptance, and provides information on the production mechanism.

This chapter provides a summary of the developments that are significant to our analysis followed by a description of the theoretical framework. Chapter 2 provides a description of the GlueX experiment including the detectors and their functioning. Chapter 3 describes the service contribution of the author to the collaboration which includes gain monitoring of one of the sub detectors and the measurement of radiation damage caused over time. The data analysis done is discussed in Chapter 4, while Chapter 5 gives detailed description of the method used for the analysis. Chapter 6 covers the Monte Carlo simulation studies used for the analysis. Chapter 7 contains the results along with the systematic studies and finally Chapter 8 contains the

conclusions and future directions of this particular research.

1.1 The standard model

At present there are four fundamental interactions known to exist in nature: gravitational, electromagnetic, weak and strong. The present complete standard model (SM) is shown in Figure 1.1, whose ultimate goal is to give a description of the universe and its behavior at a fundamental level [2]. The model is based on a quantum mechanical framework which has not yet been successfully extended to gravitation. The subatomic particles are generally classified by their mass, electric charge and spin as shown in Figure 1.1. According to the mass-energy equivalence principle described by the equation $E = Mc^2$, the unit of mass can also be given in terms of energy and speed of light, i.e. eV/c^2 which will be used throughout this thesis. The electron volts *(eV)* is the unit of energy which is equal to the energy carried by 1 electron accelerated in a potential of 1 V. Generally while talking about subatomic particles eV/c^2 is so small of mass to use so instead much larger units MeV/c^2 or GeV/c^2 .

In terms of spin, the particles can be classified broadly into fermions (half integer spin) and bosons (integer spin). 'Spin' here is a principal quantum number of a particle and it refers to the quantized intrinsic angular momentum. At a fundamental level, fermions can be further classified into six types of quarks and leptons. The theory used to explain the interaction between these particles is Quantum Field Theory (QFT) [2]. According to QFT, the particles are excited states of the underlying fields. Thus the SM consists of fermionic fields describing matter and gauge fields describing fundamental forces.

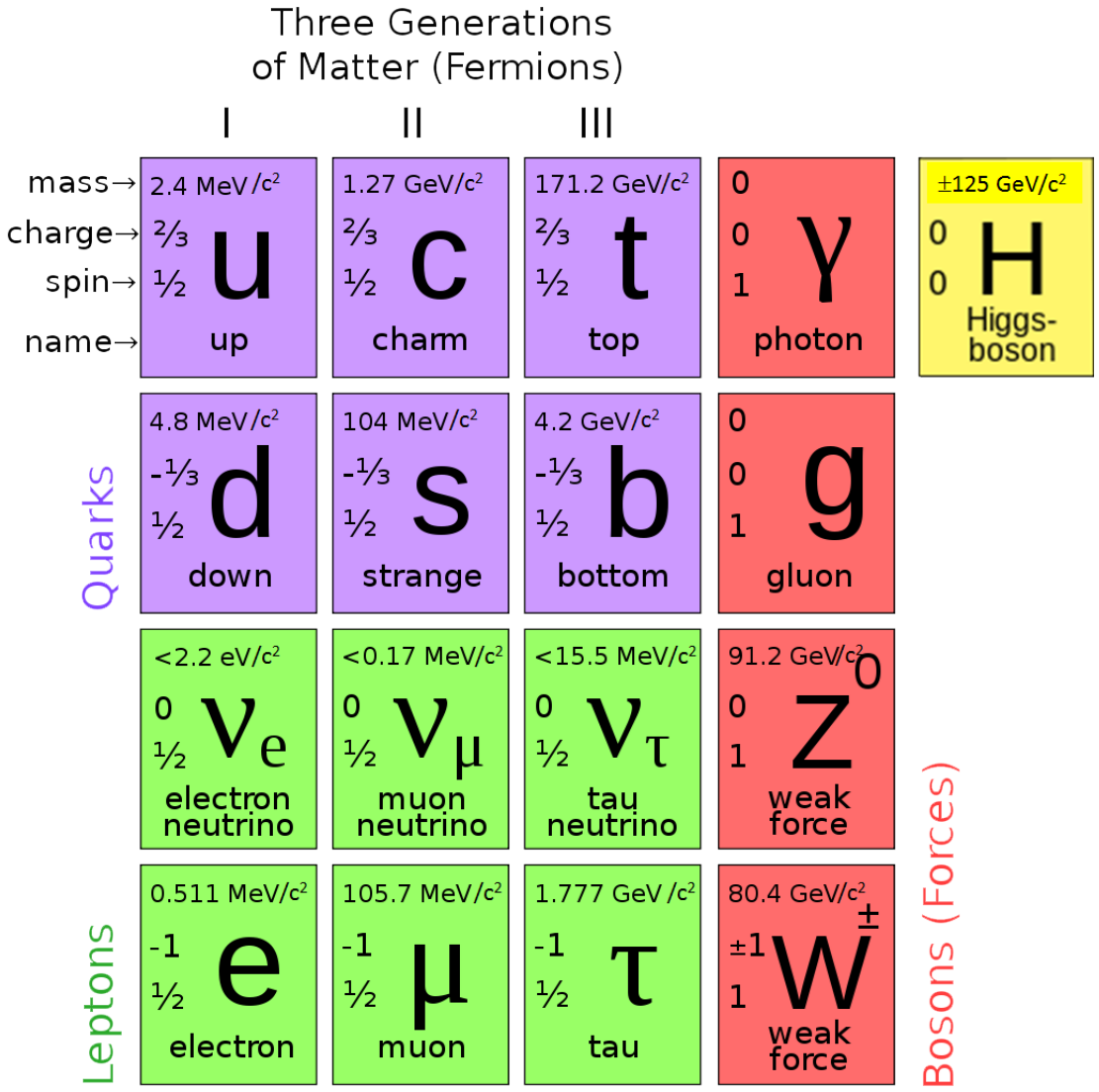

Figure 1.1: Illustration of the standard model, showing the fundamental particles and their interactions (forces). Image source: [3].

The interaction of electrically charged particles and currents, as well as electric and magnetic fields, is described by electromagnetism. The mediating particle or gauge boson is the photon. The interactions between photons and electrically charged particles are described by quantum electrodynamics (QED).

The weak nuclear force governs nuclear decay is carried by the $W^{\pm}$ and the Z bosons, and it affects particles with weak charge, such as quarks and leptons. The neutrinos are chargeless and can therefore only interact through the weak force. It was unified with electromagnetism to give electroweak theory [4].

The strong interaction which describes the interaction between quarks mediated by

gluons will be described in detail in next section. The latest addition to the SM is the Higgs boson which is a manifestation of the Higgs field. It is crucial for the generation of mass of the fundamental particles in the SM.

1.2 The strong interaction

The proton was discovered in 1919 [5] and a decade later the neutron was also detected [6]. Since they shared similar characteristics, they were considered to be the same particle, termed nucleon, but in a different state. As a result, the concept of isospin, a quantum number related to the strong force, was established. Quantum numbers required to adequately explain the diverse aspects of the strong force increased along with the number of newly found particles. The proton was grouped together with the other numerous new particles by the baryon number, B. Mesons and baryons were likewise separated, with the former having B=0 and the latter having B=1. In order to account for some of these new particles' extended lifetimes, strangeness, S was introduced. As a result, quarks and three quark flavors (now known as up, down, and strange quarks) were introduced, and the Special Unitary group of order 3 SU(3) formalism was used to describe hadrons in general. This couldn't quite explain the constituents of particles later discovered such as Δ^{++} and Ω^{-} . The Δ^{++} baryon was made up of three up quarks with all spin aligned, and the Ω^{-} baryon consisted of three strange quarks with all spin aligned. Since quarks are fermions, these two baryons would break Pauli's Exclusion Principle. Another gauge degree of freedom for the SU(3) gauge was proposed, and this one was termed as color charge [7]. The gauge boson that bound the different color charges was called the gluon. Thus, by highlighting symmetry among particular particles, a simple explanation of the processes taking place within the nucleon emerged.

In quantum mechanics, a wave function is a mathematical description of the quantum state. Since particles can exhibit wave nature, certain quantum numbers can describe the particle. Some of the relevant quantum numbers for the strong interaction

are listed below [8].

Isospin: Isospin, I, is the flavor symmetry between up and down quarks, which is slightly broken by the mass difference between the two quarks and their electromagnetic charge. The symmetrical behavior of protons and neutrons under the strong force was initially explained by this symmetry. The addition of isospin follows the similar mathematical methods as SU(2) symmetry of spin-1/2 particles.

Parity (P): The quantity parity describes how a particle's wave function behaves when the spatial coordinates are reversed., i.e.

$$\Pi\psi(x, y, z) = P\psi(-x, -y, -z)$$

where Π is the parity operator, ψ is the is the wave function, P is the eigenvalue and x, y, z are spatial coordinates.

Charge Conjugation (C): The operation that turns a particle into its anti-particle is called charge conjugation. For states that are eigenvectors of charge conjugation, the eigenvalue is 1.

***G*-Parity:** G-parity can be thought of as an extension of charge conjugation for charged particles. G-Parity is a 180° rotation of the particle's isospin and an inversion of its electrical charge.

Baryon Number: Baryon number, B, comes from the apparent conservation law for the number of baryons in an interaction. Baryons have a B of +1, antibaryons have a B of -1. In the quark model, quarks (antiquarks) have a baryon number of 1/3 (-1/3), and so mesons have a B of 0.

Flavor number: As depicted in Figure 1.1, quarks are spin 1/2 particles that come in six different types (or "flavours"). They are up, down, strange, charm, top and bottom. Quark flavor number, which is the number of each heavy quark type (heavier than up or down quarks) that makes up the meson, is conserved in strong interactions. The flavor numbers for the top, bottom, strange, and charm quarks are N_B, N_C, N_T, and N_S, respectively.

Color charge: A quark has three color charges: red, blue, or green. Furthermore,

every quark has a corresponding antiquark. They carry opposite charges but same mass of the corresponding quarks. These antiquarks are either antired, antiblue, or antigreen. The gluon is the spin 1 gauge boson associated with color charge. Since the color force is SU(3) in nature, there are eight different kinds of gluon color charge pairings. In electromagnetic interactions, photons lack electric charge. Gluons interact with one another, unlike photons. This is why QCD is significantly more complicated than electromagnetic and weak fields.

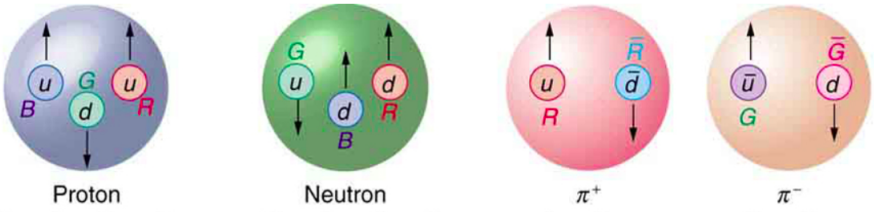

Figure 1.2: Depiction of hadrons according to quark picture. The first two depictions are examples of baryons (proton and neutron) consisting of three quarks while last two are examples of mesons (charged pions) consisting of quark-anti quark pair. The color charge is given R,G,B and spin alignments can also be seen.

As previously mentioned, everything in nature is observed to be color neutral. Combining a color with its anti-color, or all three colors combined, will produce neutrality. Hence, quarks and gluons always exist in bound states of two or more particles. Bound states with an odd number of quarks are referred to as baryons, and those with an even number of quarks as mesons.

Gellman [9] devised the Eight-fold way to bring some order to this massive collection of particles, sometimes known as the "particle zoo." Particles having the same spin and parity, or similar characteristics, were grouped together. They were plotted with varying degrees of hypercharge, $Y=B+S$, for the different rows, and from negative charge to positive charge on each row. The pseudoscalar meson octet of spin 0 is shown in Figure 1.3. The baryon decuplet of spin 3/2 is shown in Figure 1.4

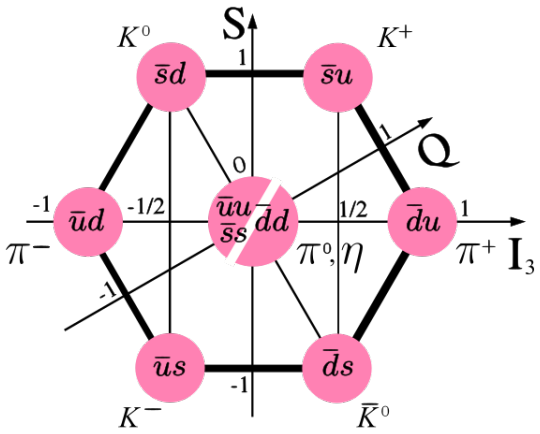

Figure 1.3: SU(3) spin-0 meson octet. The vertical axis is the strangeness (Y) of the baryon, the horizontal axis is organized by the third component of the isospin (I_3), and the diagonal lines are lines of constant electric charge (Q) [10].

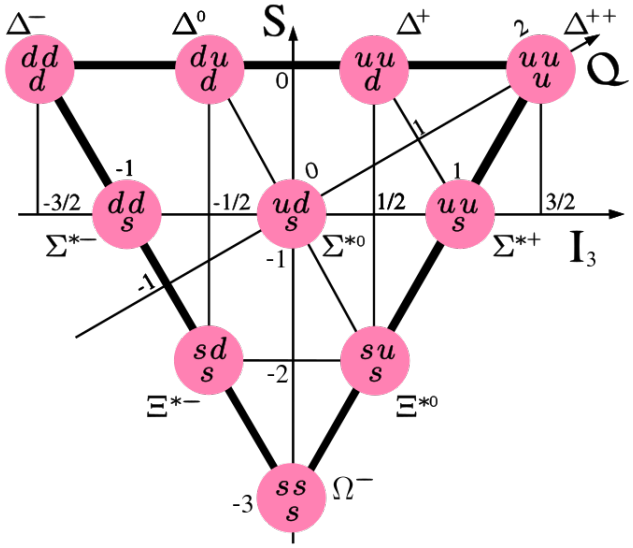

Figure 1.4: The spin-3/2 baryon decuplet. The vertical axis is the strangeness (S) of the baryon, the horizontal axis is organized by the third component of the isospin (I_3), and the diagonal lines are lines of constant electric charge (Q) [11].

1.2.1 Quantum Chromo Dynamics

Around the middle of the twentieth century a new theory called Quantum Electrodynamics (QED) based on quantum mechanics took shape, which described the electromagnetic force. Later the electromagnetic and weak forces were unified using a theory called electroweak theory [8]. In the subsequent decades Quantum Chromo Dynamics (QCD) was the established quantum field theory describing the strong force

within the Standard Model (SM) of particle physics, following elements of QED. The Lagrangian of QCD is given by [12]:

$$\mathcal{L}_{QCD} = \sum_{q} (\bar{\psi_{qi}} i\gamma^{mu} [\delta_{ij}\delta_{\mu} + ig(G^{\alpha}_{mu} t_{\alpha})_{ij}]\psi_{qj} - m_q \bar{\psi_{qi}}\psi_{qi}) - \frac{1}{4} G^{\alpha}_{\mu\nu} G^{\mu\nu}_{\alpha}$$

where the color fields tensor is given by

$$G^{\mu\nu}_{\alpha} = \delta^{\mu} G^{\alpha}_{\nu} - \delta^{\nu} G^{\alpha}_{\mu} - g f^{\alpha\beta\gamma} G^{\beta}_{\mu} G^{\gamma}_{\nu}$$

- g is the color charge.
- $G^{\alpha}_{\mu\nu}$ is the four potentialof the gluon fields (α=1,...8)
- t_{α} are 3x3 Gell-Mann matrices; generators of the SU(3) color group
- $f^{\alpha\beta\gamma}$ are the structure constants of the SU(3) color group
- ψ_i is the Dirac spinor of the quark field(i represents color)

.

Asymptotic freedom and confinement are two crucial aspects of QCD [8]. The concept of confinement describes the empirical conclusion that everything in nature is perceived to be color neutral. This implies that quarks, which are charged with color, are never seen by themselves. The force between two electrically charged particles decreases with the inverse square of the distance between the charges. The decrease in inverse square of the distance between the charges would result in a decrease in the number of field lines crossing a unit area halfway between the charges and perpendicular to the line connecting them [13]. In contrast, unlike in the case of electrical charges, the color field lines between a quark and an anti-quark do not completely fill the space. The field lines instead create flux tubes. Regardless of the distance between the quarks, a unit area positioned halfway between and perpendicular to the line connecting them intercepts a certain number of field lines. A constant force develops as a result between the quarks. Figure 1.5 qualitatively show the linear

behaviour of the potential which corresponds to a constant force between quarks and antiquarks. Thus confinement is explained by the fact that it requires infinite energy to separate the quarks to infinity.

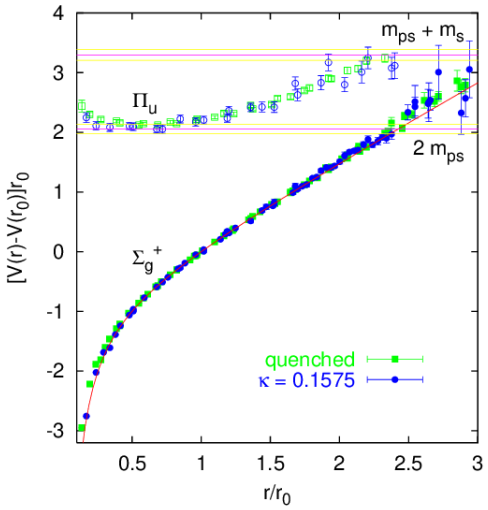

Figure 1.5: QCD- qaurk potential diagram as a function of distance r (fm) [14].

In the Figure 1.5, a recent Lattice QCD (LQCD) result of both the static potential (Σ_g^+) and the lowest hybrid excitation, in which the glue carries one unit of angular momentum is labelled by Π_u, are shown [14]. As seen in Figure 1.6, if two quarks were to be pulled apart, the energy in their binding would increase to the point where a new $q\overline{q}$ pair would be formed from the vacuum.

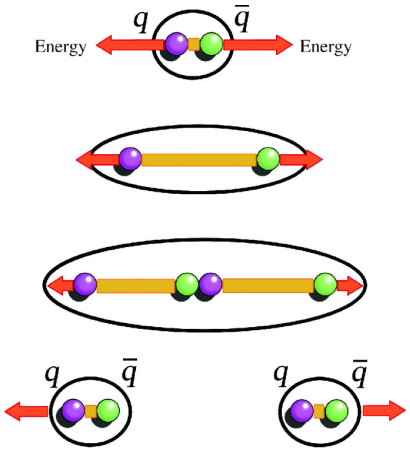

Figure 1.6: The depiction of formation of quark-anti quark pair with increase of separation of distance and energy. Source [15].

This is associated with the fact that, as Figure 1.7 illustrates, over large distances between the quarks, the strong coupling constant α_s is large. The strong coupling

constant α_s is given by $\frac{g^2}{4\pi}$, where g is the color charge. On the other hand, small α_s at very small distances explains asymptotic freedom, meaning that quarks appear to be almost free when they are very close to one another. When investigated at close ranges (high energy), α_s is sufficiently small enough to allow computations using perturbation theory. At far lower energies where α_s is large, perturbation theory is not applicable, necessitating the use of alternative methods like LQCD which will be discussed later in this chapter.

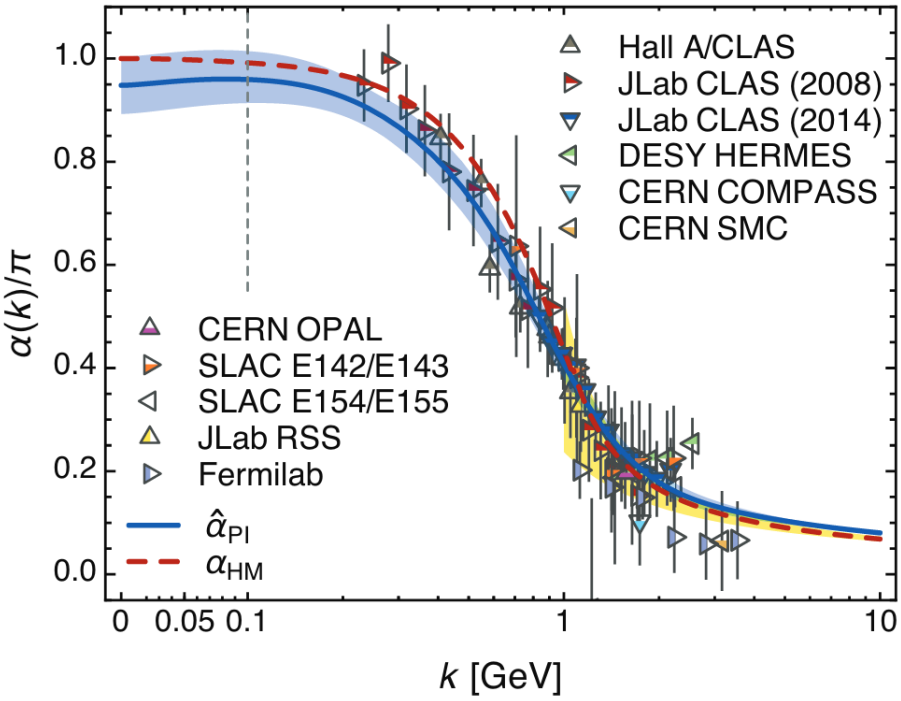

Figure 1.7: The strong coupling constant α_s measured as a function of the energy scale k [16].

1.3 Exotic Mesons

When two quarks are combined, their total angular momentum is given by

$$\overrightarrow{J} = \overrightarrow{L} + \overrightarrow{S}$$

The parity for a quark-antiquark $q\overline{q}$ pair is given as

$$P = (-1)^{L+1}$$

The charge conjugation eigenvalue for a $q\overline{q}$ pair is given as

$$C = (-1)^{L+S}$$

The $(-1)^L$ contribution arises from the spatial inversion in the angular dependence of the $q\overline{q}$ wave function. For a system of two fermions, the inversion of the spin wave functions results in a factor of $(-1)^{S+1}$, and the interchange of the q and $\overline{q}$ produces an extra contribution of (-1). Mesons with quantum numbers as shown in Table 1.1 are constructed following the above given rules.

Allowed quantum numbers for a meson			
	L=0	L=1	L=2
S=0	0^{-+}	1^{+-}	2^{+-}
S=1	1^{--}	0^{++},1^{++},2^{++}	1^{--},2^{--},3^{--}

Table 1.1: Allowed quantum numbers for a meson according to QCD [8].

The states that are missing in this table are 0^{+-},1^{-+}, 2^{+-}, 3^{-+}, ... These states are termed as states with exotic quantum numbers. Existence of these exotic meson states suggests a contribution to the quantum number apart from a $q\overline{q}$ pair.

Allowed quantum numbers for a meson					
State	Name	Alignment(s)	Wave(L)	J^{PC}	Mesons
$^1S_0$	pseudoscalar	anti-aligned(0)	S(0)	0^{-+}	$\pi\ \eta\ \eta'\ \kappa$
$^3S_1$	vector	aligned(1)	S(0)	1^{--}	$\rho\ \omega\ \phi\ \kappa*$
$^1P1$	pseudovector	anti-aligned(0)	P(1)	1^{+-}	$b_1\ h_1\ h_1'\ \kappa_1$
$^3P_0$	scalar	aligned(1)	P(1)	0^{++}	$a_0\ f_0\ f_0'\ \kappa*_0$
$^1S_0$	pseudoscalar	aligned(1)	p(1)	1^{++}	$a_1\ f_1\ f_1'\ \kappa*_1$
$^1S_0$	vector	aligned(1)	P(1)	2^{++}	$a_2\ f_2\ f_2'\ \kappa*_2$

Table 1.2: Meson states that can be formed following the quark-antiquark model and considering only S and P waves (L=0,1) [17].

One among the numerous models for meson states that could produce exotic quantum numbers is the hybrid meson. A Hybrid meson consists of a quark and antiquark held together by an excited gluon. Access to the exotic quantum numbers that are prohibited for a quark-antiquark pair is made possible by this gluonic excitation.

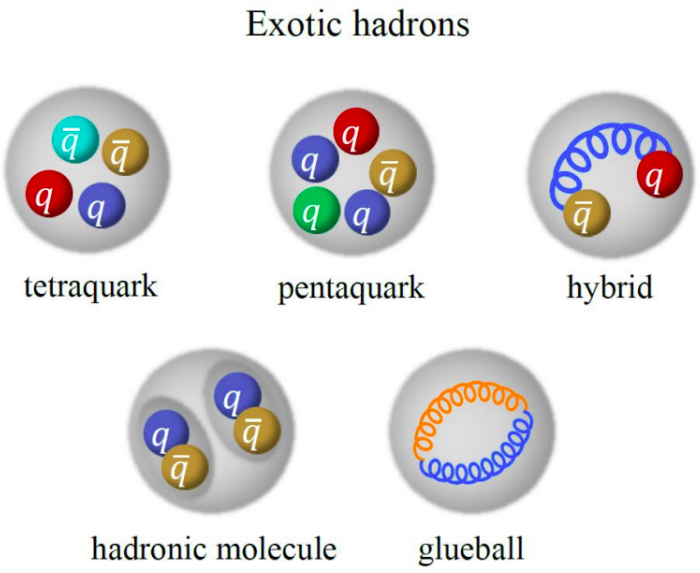

Figure 1.8: An illustration of exotic hadrons and their configurations.

1.3.1 LQCD prediction

One among the non-perturbative approaches for solving QCD is Lattice QCD (LQCD). It uses a grid or lattice of points in space and time and offers a technique for calculating interactions in the low energy (non-perturbative) regime [18]. Gluon fields serve as links between lattice points, and quark-gluon coupled fields are located on the lattice points, which are equally spaced apart in time as shown in Figure 1.9.

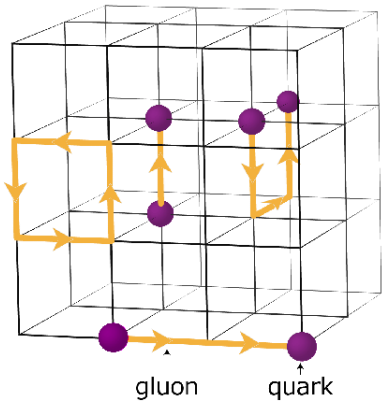

Figure 1.9: An illustration of Lattice QCD discretization. Source [19]

By taking the limit when the lattice spacing disappears, the continuous theory, or real QCD, emerges. The framework of this technique was developed in 1970's by Kenneth Wilson [20]. The computational power limits at the time resulted in systematic inaccuracies on predictions made using LQCD. The elimination of vacuum polarisation effects, also referred to as "quenching", is one way to simplify the calculation. Additionally, larger lattice spacing, fewer lattice sites, and frequently unphysically huge quark masses are used to reduce computation requirements. These all lead to substantial systematic errors in the extrapolation down to anticipated quark masses and vanishing lattice spacing.

The exponential growth of computing power and processing speeds have increased remarkably over past few decades. With the power of current computing, calculations on the lattice with ever-smaller lattice spacings and quark masses can be performed without quenching on large lattices. As a result, theoretical results were obtained that show good agreement with experimental results. A number of input parameters are required to do LQCD calculations, including the lattice spacing a, the quark masses, and the CP (charge conjugation parity) violating phase θ, which is usually set to 0 for lattice calculations. Quark masses are determined using data from experiments. The lattice mass, which for contemporary lattice computations is approximately 400 MeV [21], is typically given as the precision of the tuning. The masses or resonance characteristics of all other states, such as regular hadrons, hybrids with gluonic degrees of freedom, and glueballs, can be predicted after these input parameters have been

specified. Lattice results on some multiquark states (tetraquarks and pentaquarks) also exist [22]. The Hadron Spectrum Collaboration (HadSpec) has used lattice QCD calculations [18] to predict the isovector and isoscalar meson spectrum of states without open strangeness, shown in Figure 1.10.

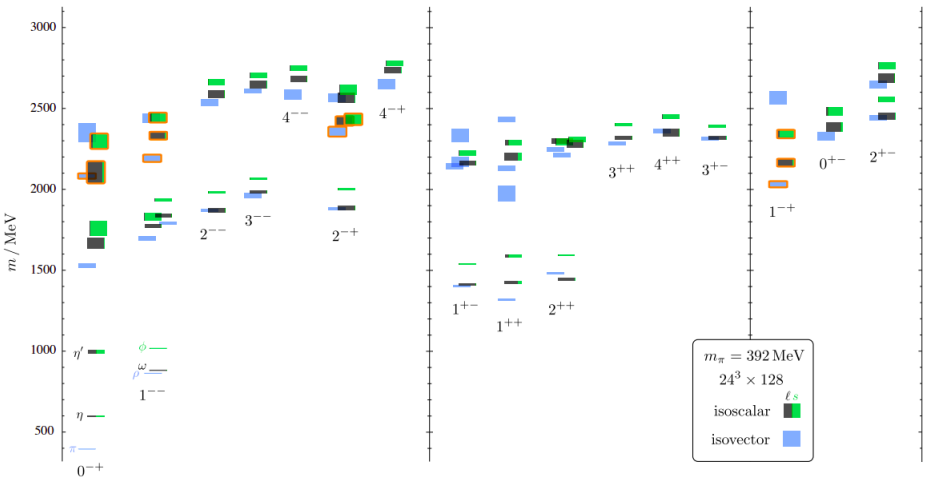

Figure 1.10: The meson spectrum using the LQCD, represented as state mass against quantum numbers (J^{PC}). The height of a state indicates the error on the mass. Octet/singlet mixing angle is indicated by black and green contributions to isoscalar mesons. Orange highlights indicate contenders for the lightest hybrid super multiplet. Source [18].

LQCD is a developing field and can now produce computations that are accurate. For example, LQCD was used for computing a proton's mass with an approximate error of 2% [23]. It is also helpful for many other applications, such as form factors for electroweak CKM matrix elements, hadronic contributions to muon anomalous magnetic moment, and the spectrum of light hadrons [12]. Within the light unflavored hadron spectrum, LQCD can reproduce established vector and pseudoscalar states. Figure 1.10 shows these states (i.e., π, η, ρ, ω, and ϕ) labeled. At greater masses, LQCD additionally predicts a number of extra states. In this picture, states that have a gluon contributing to their state are shown by orange color. It can be seen that some of these orange outlined states have exotic quantum numbers. A few predicted exotic states along with their predicted allowed decay modes and width are listed in Table 1.3. As shown in the table, the η meson is in the allowed decay modes of the lightest exotic multiplet π_1 and other exotic states (b_0, h_0, b_2 and h_2).

Allowed quantum numbers for a meson			
Name	J^{PC}	Total Width MeV PSS IKP	Allowed Decay Modes
π_1	1^{-+}	81-168, 117	$b_1\pi_1$, $\pi\rho$, πf_1, $\pi\eta$, $\pi\eta_0$, $\pi\eta(1295)$, ηa_1
η_1	1^{-+}	59-158, 107	πa_1, πa_2, ηf_1, ηf_2, $\eta\eta_0$, $\kappa\kappa_1^A$, $\kappa\kappa_1^B$
η_1'	1^{-+}	95-216, 172	$\eta\eta_0$, $\kappa\kappa_1^A$, $\kappa\kappa_1^B$, $\kappa\kappa^*$
b_0	0^{-+}	247-429, 665	$\pi\pi(1300)$, πh_1, ρf_1, η
h_0	0^{-+}	59-262, 94	πb_1, ηh_1, $\kappa\kappa(1460)$
h_0'	0^{-+}	259-490, 426	$\kappa\kappa(1460)$, $\kappa\kappa_1^A$, ηh_1,
b_2	2^{+-}	5-11, 248	πa_1, πa_2, πh_1, $\eta\rho$, ηb_1, ρf_1
h_2	2^{+-}	4-12, 166	$\pi\rho$, πb_1, $\eta\omega$, ωb_1
h_2'	2^{+-}	5-18, 79	$\kappa\kappa_1^A$, $\kappa\kappa_1^B$, $\kappa\kappa_2^*$

Table 1.3: A compilation of exotic quantum number hybrid approximate masses, widths, and decay predictions [17]. Masses are estimated from dynamical LQCD calculations with $m_\pi = 396\ MeV$ [21]. The PSS (Page, Swanson and Szczepaniak) and IKP (Isgur, Kokoski and Paton) model widths are from [24], with the IKP calculation based on the model in [25].

Lattice simulations reveal a rich spectrum of non-conventional mesons, and the confirmation of individuals in the lightest hybrid supermultiplet would all but verify the presence of mesons that are gluon degree of freedom contributors. Finding concrete proof of these and other hybrid states are the important goals for the experiments like GlueX.

1.4 Photoproduction

One method to produce exotic hybrid mesons is photoproduction, where a highly energetic photon interacts with the nuclear target. GlueX uses 8.2-8.8 GeV photon beam and proton inside liquid hydrogen (LH_2) as target. Another method could be to use hadron beam like a pion. According to theoretical predictions, an exotic quantum number is more likely to be produced by a photon beam than by a pion beam [13]. Figure 1.11 compares the two distinct approaches to producing a resonance X. In conventional mesons, gluons have been modeled as flux tubes, which are in the ground state. In this picture, the ($q\overline{q}$) is held together by a cylindrical tube of color

flux, and the binding energy is proportional to the tube length. An exotic meson can be described as a normal meson, but with an excitation of the gluonic flux tube. A normal meson that has had the gluonic flux tube excited is called an exotic meson. Since the two quarks in a pion beam have anti-aligned spins, an exotic meson can only be produced by aligning the spins and then excitation of a flux tube. It is more likely that a hybrid made using this technique won't have an exotic quantum number. It is possible to think of a photon beam (right, Figure 1.11) as a virtual $q\overline{q}$ pair whose spins are already aligned to generate a net spin S = 1. Therefore, an exotic quantum number can be produced with just a flux tube excitation [13].

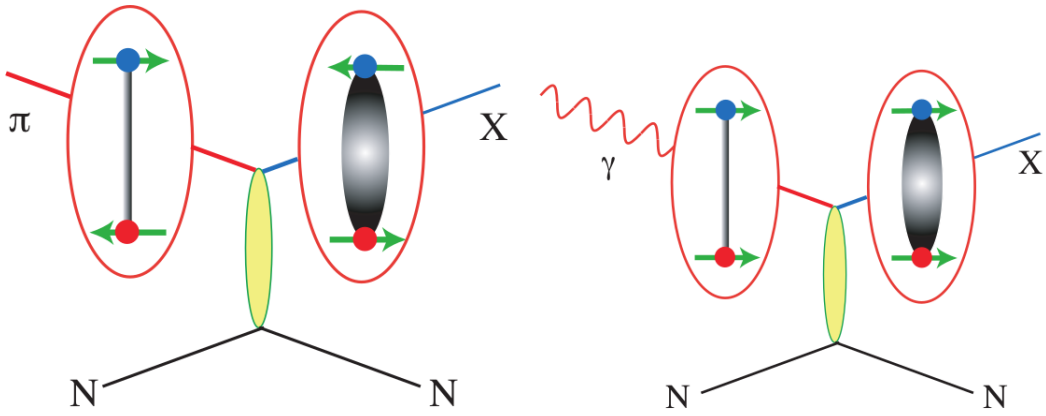

Figure 1.11: Prediction of behaviour of two distinct beams on nuclear target. Photon-probe (right) versus pion-probe (left). With its spin of 1, the photon-probe may have a higher probability of producing an exotic with spin 1. Source [13]

Since the photon is the force carrier in electromagnetic interaction, it cannot directly take part in strong interaction. But, it can couple to quarks at high enough energies, such those found in GlueX, and produce hadronic matter. This process can be explained using Vector Meson Dominance (VMD) model [13]. The photon and light vector mesons share the same J^{PC} of 1^{--}. According to VMD, the photon can be thought of as an off-shell (or virtual) vector meson. The photon cannot simply converted a vector meson in free space, as this violates conservation of four-momentum. But in GlueX the target proton can accept a small momentum kick from the photon. Thus the off-shell vector meson can suddenly become on-shell. This is a similar concept as that of pair production, where e^- e^+ pair cannot be produced from

a single photon in vaccum or free space but are only produced near nuclear matter while obeying conservation laws.

Nuclear targets heavier than hydrogen will have more nucleons. In this case, figuring out which nucleon the photon had interacted with will be difficult. Choosing of proton as target further helps in reducing this complication.

1.4.1 Mandelstam variables

While making use of relativistic kinematic quantities it is easier to deal with mandelstam variables which encode quantities like energy, momentum, and angles of four particles in a two-body scattering process in a Lorentz-invariant fashion. There are three possible "channels" for two body scattering reactions when there is only one virtual particle exchanged as shown in Figure 1.12

$$s = (p_1 + p_2)^2 = (p_3 + p_4)^2$$

$$t = (p_1 - p_3)^2 = (p_2 - p_4)^2$$

$$u = (p_1 - p_4)^2 = (p_2 - p_3)^2$$

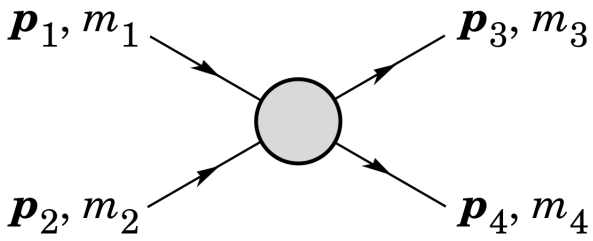

Figure 1.12: A two-to-two body scattering process depiction alongwith the kinematic variables.

At lower beam energies (about 100 MeV to 1 GeV), s channel processes dominate. This region of beam energy is often referred to as the resonance region. At higher energies, t channel processes dominate. This is the energy regime of GlueX. Here we see much smoother overall behavior as baryon resonances become less important

and more hadronic channels open up. For example Figure 1.13 shows scattering of 4 particles each having four-momenta P_1, P_2, P_3 and P_4.

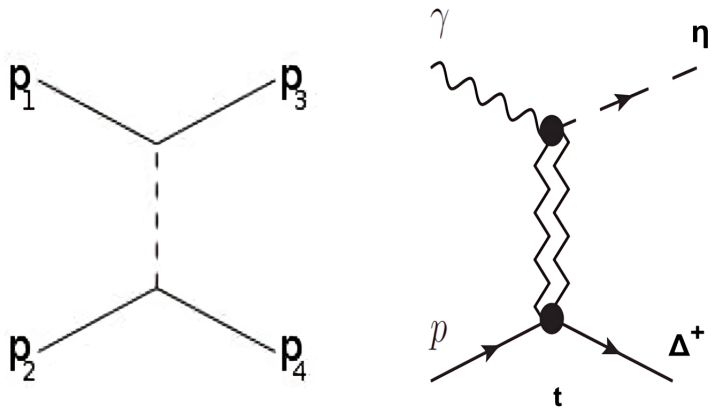

Figure 1.13: Exchange interaction diagram for the reaction γp $\rightarrow$ η Δ^+ where Mandelstam t is given by $t = (P_2 - P_4)^2 = (P_1 - P_3)^2$. The γp $\rightarrow$ ηp has a proton at the bottom instead of Δ^+.

Particle 1 transforms into particle 3 by emitting a virtual particle. Particle 2 absorbs the virtual particle and transforms into particle 4 as a result of this interaction. Given that particle 3 has momentum P_3 and particle 1 had momentum P_1 prior to emission, the difference between these two must have contributed to the virtual particle that was produced, which has (squared) momentum Mandelstam t and provides information on the production method. Here, it is the square of four momentum transferred between the proton and recoil baryon, and in this case Δ^+ for γp $\rightarrow$ η Δ^+, as shown in the diagram in Figure 1.13. The detailed theoretical description on these exchange of virtual particles is given in next section.

1.4.2 Psuedoscalar production

One of Gluex's main objectives is to perform a Partial Wave Analysis (PWA).[1] in order to determine J^{PC} of exotic mesons. But first, GlueX must be able to reconstruct pure samples of the final state mesons (π, η, ρ, η', ω, ϕ), which feature in exotic meson decay

[1]PWA is a method for tackling scattering problems in quantum mechanics that involves breaking down each wave into its component angular momentum components and solving them using boundary conditions.

products. Mesons with 0^{--} quantum numbers, or pseudoscalar states, are among the most frequently generated particles at GlueX. Since they are spin 0 particles, they provide a very useful system for measurement. These states are spineless, which is beneficial because it drastically lowers the complexity of the system and, eventually, the number of observables we have to measure.

1.5 Neutral Pseudoscalar Beam Asymmetry

As mentioned before, understanding the production mechanism of the η, η' mesons is crucial, since they are present in many expected exotic meson decay channels. Therefore, the first step toward the main goals at GlueX includes studying simple mesons and known resonances while improving matching between simulation and data for simple processes. An initial aim of GlueX analyses was to increase photoproduction statistics at GlueX energies of about 8-9 GeV and to measure quantities like the Σ beam asymmetry of particles, which is described in the following section.

1.5.1 Theoretical description

In medium-energy scattering experiments like GlueX, the beam-target interaction is dominated by production and decays of mesons. Regge phenomenology underlies such processes and provides the theoretical framework for studying medium energy scattering [26]. This approach does not directly use QCD, but uses more general principles of particle interactions: unitarity, analyticity, and crossing-symmetry. In Regge theory, the angular momentum can take any complex number value having both real and imaginary parts. The path taken in this complex plane is termed as Regge trajectories also referred as reggeons or Reggized exchanges [27]. These Reggeons have well-defined quantum numbers such as isospin and J^{PC}.

In this method the complex quantities known as "amplitudes" are used. These amplitudes describe the full set of initial and outgoing helicity states for an incoming photon and proton, and outgoing meson and proton. Helicity is defined for a particle

as the projection of its intrinsic spin onto the direction of its momentum. Thus, we incorporate the spin information of incoming and outgoing particles. For now, we assume the photon is fully linearly polarized. Later, the partial polarization of GlueX will be incorporated.

For this scattering reaction with a set of two incoming and outgoing helicity states considered, there are are four independent complex amplitudes required to fully encode the reaction [27]. These amplitudes have specific values of CP (i.e. the product of C and P) along with another property, naturality. Naturality is defined by $\eta = P(-1)^J = \pm 1$ =where P is parity. These amplitudes are labelled as F_1, F_2, F_3, and F_4 [28]. The specific values of quantum numbers are given below:

- $F_1 : CP = +1; \eta = +1$
- $F_2 : CP = -1; \eta = -1$
- $F_3 : CP = +1; \eta = +1$
- $F_4 : CP = +1; \eta = -1$

The cross section as a function of Mandelstam t is given (to leading order in mandelstam s) can be expressed in terms of these four amplitudes [27] by:

$$\frac{d\sigma}{dt} \approx \frac{1}{32\pi}\left[\frac{|F_3|^2 - t|F_1|^2}{4M^2 - t} + |F_2|^2 - t|F_4|^2\right] \tag{1.5.1}$$

Due to naturality addition, the linear polarization of photon beam results in an azimuthal angle ϕ dependence for these two classes of amplitudes as shown in Equation 1.5.1. In this coordinate system, x is normal to the production plane, z points along the path of the photon beam, and y is given by $z \times x$. The angle between x and the polarized photon's electric field is ϕ.

$$\frac{d\sigma}{dt} \approx \frac{1}{32\pi}\left[\frac{|F_3|^2 - t|F_1|^2}{4M^2 - t} sin^2(\phi) + |F_2|^2 - t|F_4|^2 \cos^2(\phi)\right] \tag{1.5.2}$$

According Stichel's Theorem [29], the total cross section can be expressed as the sum of components parallel and perpendicular to the reaction plane, or

$$\frac{d\sigma}{dt} = \frac{d\sigma_{\perp}}{dt} + \frac{d\sigma_{\parallel}}{dt} \tag{1.5.3}$$

Therefore, when polarization is perpendicular to the reaction plane, only the natural amplitudes ($\eta = +1$) contribute to the cross section, and when polarization is parallel, only the unnatural amplitudes (η = -1) contribute. For example, the production mechanism of η meson can be described by these Regge exchanges or amplitudes. This shown by t channel exchange interaction diagram for the reaction $\gamma p \rightarrow \eta p$ in Figure 1.14. The potential exchanges for η can be natural exchanges like vector exchanges ρ and ω or unnatural exchanges like pseudovector exchanges b and h. The relative contribution of ρ and ω mesons to b and h mesons can be found when a photon beam producing the η is linearly polarized, as it is at GlueX.

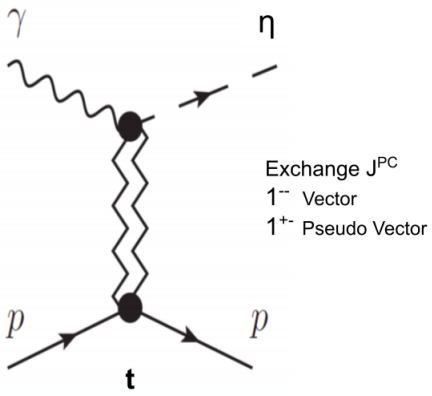

Figure 1.14: Exchange interaction diagram for the reaction $\gamma p \rightarrow \eta p$ where Mandelstam t is given by $t = (P_2 - P_4)^2 = (P_1 - P_3)^2$.

These components can be distinguished from one another because, in the case of a linearly polarized photon beam, the azimuthal angular dependences of natural and unnatural exchanges differ as shown in Equation 1.5.1. Defining a beam asymmetry is one technique to parameterize the relative contribution of natural and unnatural exchanges.

$$\Sigma = \frac{\left(\frac{d\sigma_{\perp}}{dt}\right) - \left(\frac{d\sigma_{\parallel}}{dt}\right)}{\left(\frac{d\sigma_{\perp}}{dt}\right) + \left(\frac{d\sigma_{\parallel}}{dt}\right)} \tag{1.5.4}$$

or using the underlying amplitudes,

$$\Sigma\frac{d\sigma}{dt} \approx \frac{1}{32\pi}\left[\frac{|F_3|^2 - t|F_1|^2}{4M^2 - t} + |F_2|^2 - t|F_4|^2\right] \tag{1.5.5}$$

The range of values for the beam asymmetry quantity Σ is from -1 to 1. Measuring $\Sigma = 1$ would suggest that only ρ and ω exchanges contribute to the reaction in the Regge exchange picture, whereas measuring Σ = -1 would suggest that only b and h mesons contribute.

For the case of partial polarization P_γ as that in GlueX, the differential cross section at fixed $s$and t can be written as

$$\sigma_{pol}(\phi, \phi_{lin}) = \sigma_0[1 - P_\gamma \Sigma cos(2(\phi - \phi_{lin}))] \tag{1.5.6}$$

where:

P_γ is magnitude of linear polarization, ϕ_{lin} is the direction of the beam polarization.

1.5.2 Previous measurements and motivation

We have discussed the theoretical description of how beam asymmetry Σ gives insight in beam-target exchange mechanism for photo production of η. In this section, we will briefly discuss the previous Σ measurements done at GlueX and motivation for this thesis work.

The Equation 1.5.6 forms an asymmetry histogram that is fitted directly. The quantity $\mathbf{\Sigma}$ is left as the only free parameter, which is extracted from the fit. This direct fitting method has been used for previous π^0 and η measurements done at GlueX. Results for π^0 and η are shown in Figure 1.15 and Figure 1.16 below. These were published in 2017 [30] and 2019 [31]. The asymmetry Σ is found to be very close to 1, indicating that ρ and ω exchanges dominate. These results are useful for informing searches for electrically neutral hybrid mesons. So far, the η beam asymmetry (Σ_η) has been measured using channel $\gamma p \to \eta p$, i.e. with a recoiling proton. It would be interesting to measure Σ_η with another recoiling baryon. Thus,

we turn to the Δ baryons to find a recoil partner. Previously in GlueX, Σ of the π^- was measured using a recoiling Δ^{++} [32]. The results are shown in Figure 1.17. The method used for π^- Δ^{++}, known as moment yield method, is different from the previous direct fitting method. Both these methods will be discussed in detail in Chapter 5

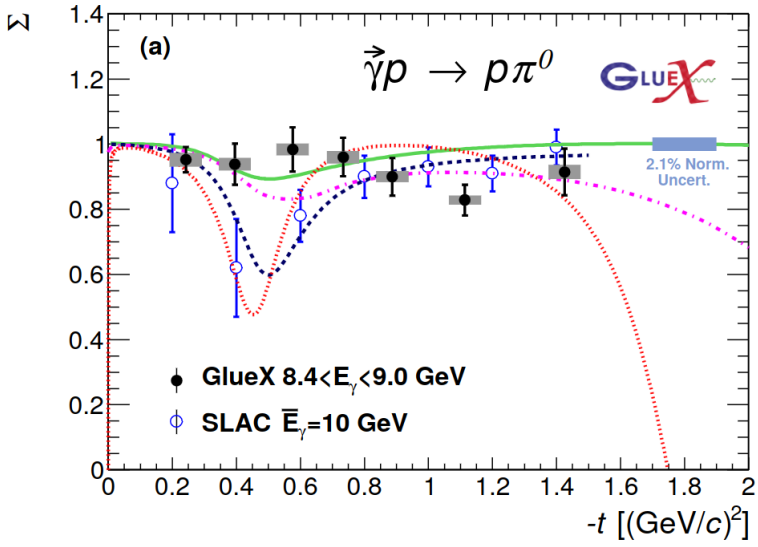

Figure 1.15: Beam asymmetry results for the reaction γp $\rightarrow\pi^0$p [30] along with various model predictions (Laget (pink dashed line) [33] [33], JPAC (green solid line) [34], Donnachie (blue dashed line) [35] and Goldstein (red closely dashed line) [36]).

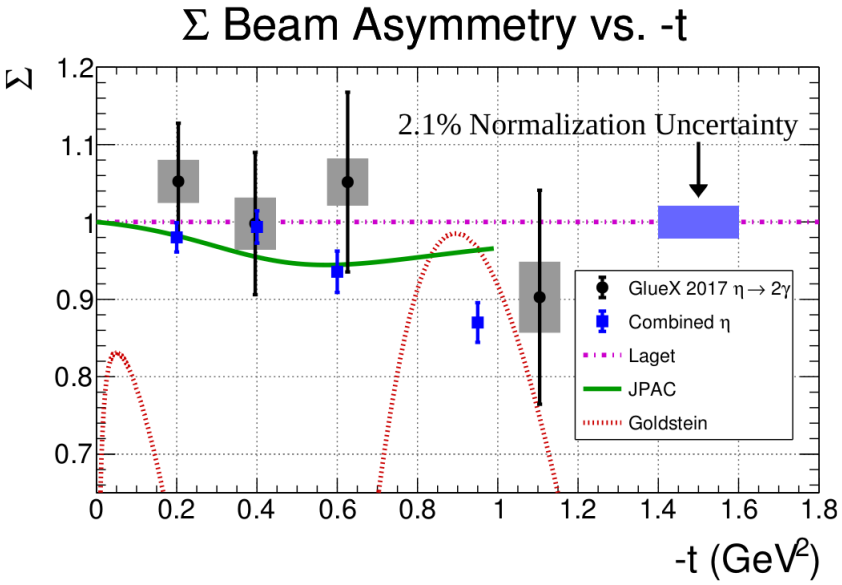

Figure 1.16: Beam asymmetry results for the reaction γp $\rightarrow$ ηp [31] along with various model predictions (Laget [33] [33], JPAC [34]and Goldstein [36])

.

The π^- Δ^{++} analysis using the moment yield method motivated a new analysis with a recoiling Δ baryon against a η by using the same method. By charge conservation the Δ^+ will be the recoiling baryon. So the channel will be $\gamma p \rightarrow \eta\ \Delta^+$ where η decays into two photons ($\eta \rightarrow \gamma\ \gamma$) and Δ^+ decays into proton and π^0 ($\Delta^+ \rightarrow p\ \pi^0$). This is the first time that Σ_η has been extracted using this particular channel, as no previous measurements were done and will be complementary to the existing ηp channel measurements.

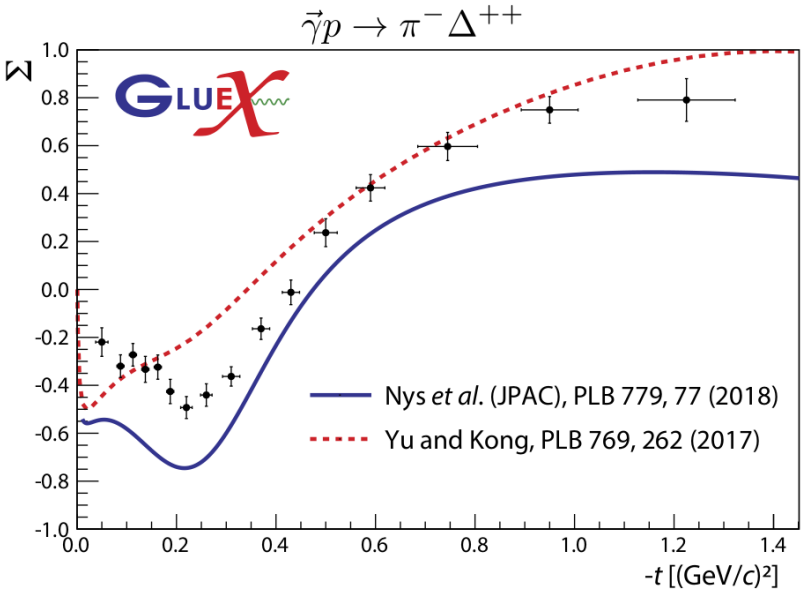

Figure 1.17: Beam asymmetry results for the reaction $\gamma p \rightarrow \pi^-\ \Delta^{++}$ [32].

1.5.3 Theoretical models

So far two separate theoretical models have been developed from JPAC and a Korean theory group are described in this section. The details of these two models are given in Chapter 7 along with the final results. The theoretical modeling for this channel is very similar to that of ηp using the Regge model. The Regge model incorporates s, t and u channel processes while accounting for gauge invariance. Since the final state is the Δ^+ baryon of isospin 3/2 there has to be some additional considerations. The exchange must have C = -1 from the $\gamma\eta$ vertex and I = 1 from the pΔ^+ vertex,

so the only exchanges are the ρ and the b mesons. V.Mathieu, of the JPAC theory collaboration, took the model for $\gamma p \to \pi^- \Delta^{++}$ [28] and adapted it for $\gamma p \to \eta \Delta^+$, as the two reactions have the same recoil baryon with spin 3/2 incorporated into the formalism. The theoretical curves are shown below.

JPAC model

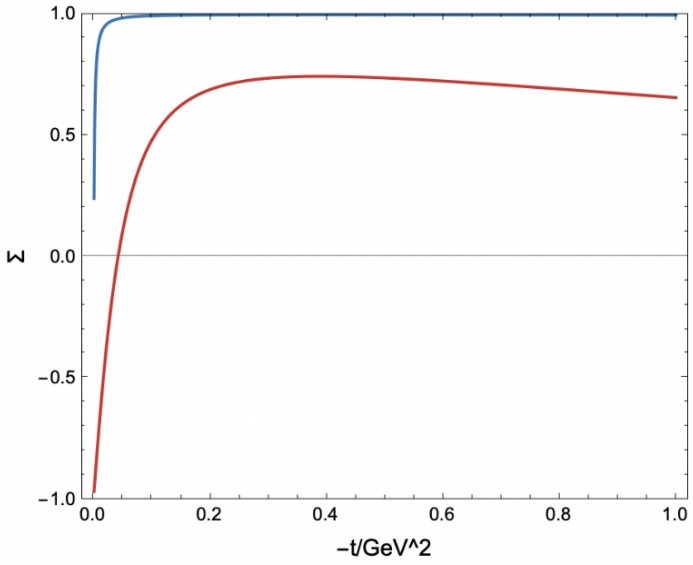

Figure 1.18: The theoretical curves provided by V.Mathieu (JPAC theory collaboration) [34].

The Yu-Kong group has also provided theoretical predictions using the same Regge formalism and exchanges [37]. The Yu-Kong group has two versions of their model as shown in Figure 1.20. The Regge propagator used contains a phase term, and these two versions either treat the ρ_0 and b_1 exchanges as having either a complex phase or non-degenerate one.

Yu-Kong model

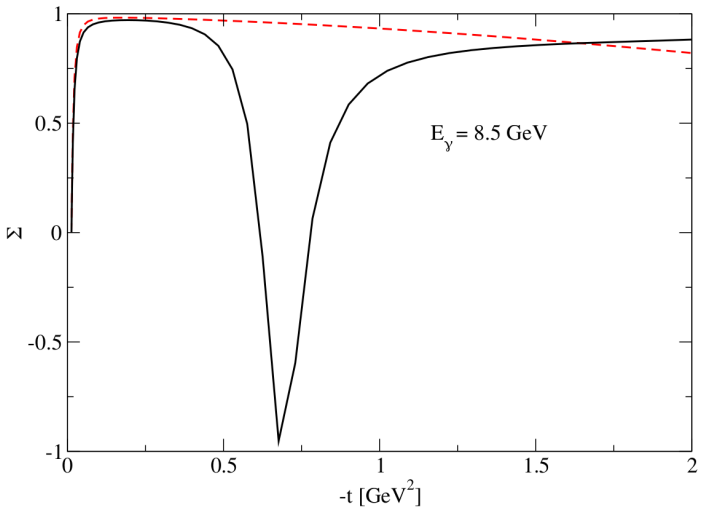

Figure 1.19: The theoretical curves provided by the Yu-Kong theory group [37]. Red-dashed results from both the ρ^0 and b_1 phases chosen complex, where as the solid curve represents the case of both the ρ^0 and b_1 non-degenerate phase. The x axis is t values, the y axis is Σ_η.

An exchange interaction diagram is shown below in Figure 1.20 with potential exchanges.

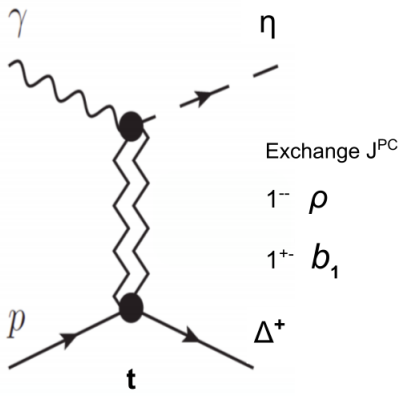

Figure 1.20: Exchange interaction diagram for the reaction $\gamma p \to \eta\Delta^+$, which is the topic of investigation for this thesis.

Chapter 2

GlueX Experiment

The US Department of Energy's Thomas Jefferson National Accelerator Facility (JLab) houses the Continuous Electron Beam Accelerator Facility (CEBAF) and four experimental halls A,B,C and D, with Hall D being the latest addition. The purpose of the Gluonic Excitation (GlueX) experiment at Hall D is to search for and map out the exotic hybrid meson spectrum using a 8.2-8.8 GeV linearly-polarized photon beam impinging on a proton target [38]. An overhead view of JLab is shown in Figure 2.1.

Figure 2.1: Aerial view of JLab. [39]

2.1 CEBAF

The CEBAF consists of a race track configuration with two parallel linear accelerators based on superconducting radio frequency (RF) technology. The whole setup comprises of a polarized electron source, an injector, two superconducting RF linear accelerators or LINACs, and several recirculating arcs. The accelerator forms a racetrack shape 1.4 km in length as shown in Figure 2.2.

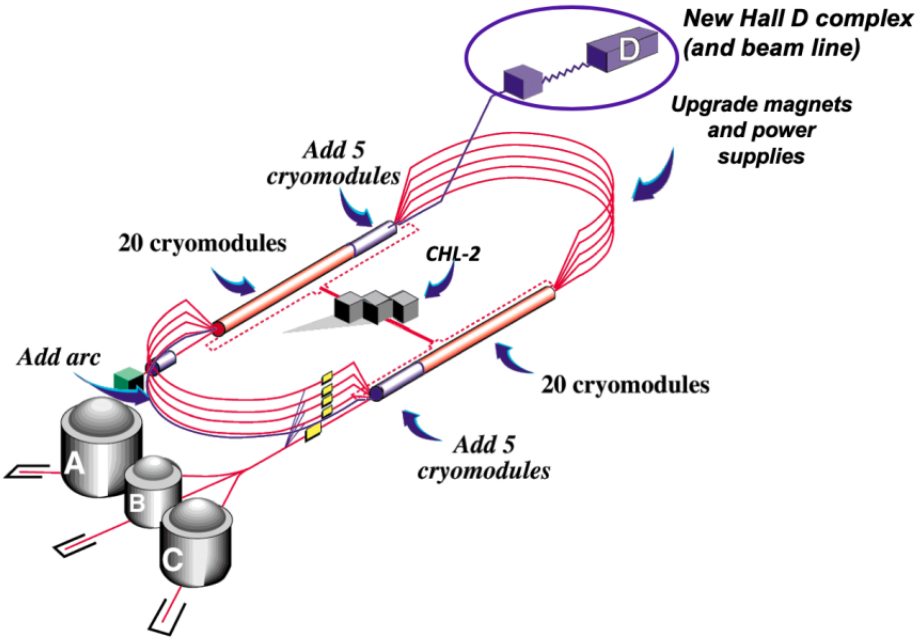

Figure 2.2: Schematic of the CEBAF accelerator showing the additions made during the 12-GeV project including the Hall D complex. [39]

At the injector site, a near-infrared laser light is shined on a gallium arsenide photocathode, which ejects electrons via the photoelectric effect. These are pulsed at a subharmonic of the natural frequency of 1497 MHz used in the CEBAF linear accelerators, producing bunches of polarized outgoing beam. The two linear accelerators in the CEBAF racetrack are superconducting RF devices, utilizing superconducting niobium cavities cooled to 2-4 K using liquid helium. The individual niobium cells are assembled in units of seven termed "cavities". These are then organized into groups of eight known as "cryomodules". These RF cavities consist of "cells" with standing RF-frequency waves set up to match the frequency and phase of incoming electron bunches. This results in a electric field gradient acting on each electron bunch which experiences an electric force due to negative charge behind and positive charge ahead as shown in Figure 2.3. Thus imparting an additional energy kick during acceleration. The net energy about 1.1 GeV, or roughly 2.7 MeV/m is imparted from each of the two LINACs.

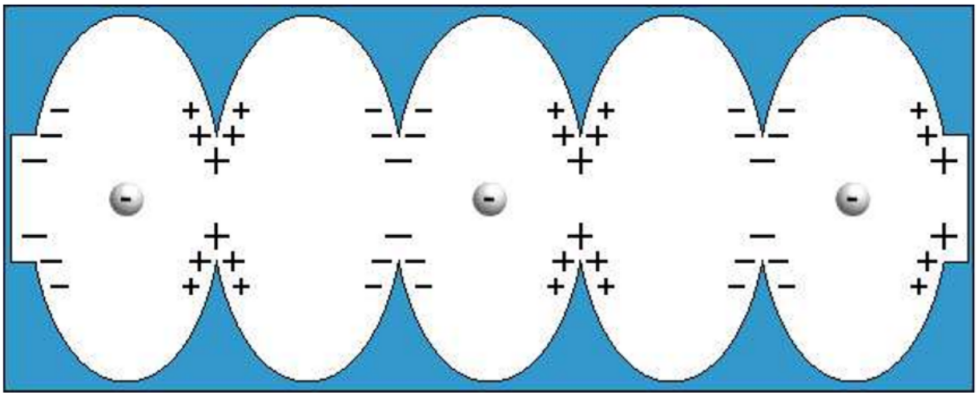

Figure 2.3: Image depicting electrons within an RF cavity of five cells. The electric fields accelerates the electrons along the direction of motion as shown above. [40]

In comparison to the use of non-superconducting copper cavities, which suffer from non-zero resistivity that requires much higher power consumption and significant cooling periods, the superconducting RF cavities allows Jefferson Lab to operate with more efficiency and lesser power consumption. However, for the operation of superconducting technology a large supply of liquid helium is required.

Before making it to the Hall D, the electrons have to travel around the CEBAF racetrack 5.5 times. Reusing the same linac multiple times increases the electrons' energy, adding about 2.2 GeV with each pass thus delivering around 12 GeV electrons. The currents to Hall D are 100-300 nA and for Hall B of the order 100 nA. Whereas to Hall A and Hall C, the current is of the order of μA. The plan for the JLab 12 GeV upgrade allowed for all four halls to run simultaneously. However, this option requires that at least one other hall must use 5th pass beam at a frequency of 249.5 MHz. The resulting beam delivered to Hall D is an essentially monoenergetic beam, delivered in bunches every 4.008 ns.

2.2 The Hall D beamline

The electron beam from the north LINAC enters the tagger hall of the Hall D complex where photoproduction occurs through coherent bremsstrahlung off a diamond crystal radiator. By using a tagger magnet and tagger hodoscope, the energies of the scattered

electrons and thereby the energies of the photons are measured or "tagged". The tagged photons then travel to the experimental hall. A collimator aids in centering the beam on target. The collimated beam passes first through triplet polarimeter which measures the beam polarization. Then it passes through pair spectrometer which measures photon flux. The photon beam then moves further downstream to finally interact with the liquid hydrogen target as shown in Figure 2.4. Details of the beam line and detectors will be discussed in this section.

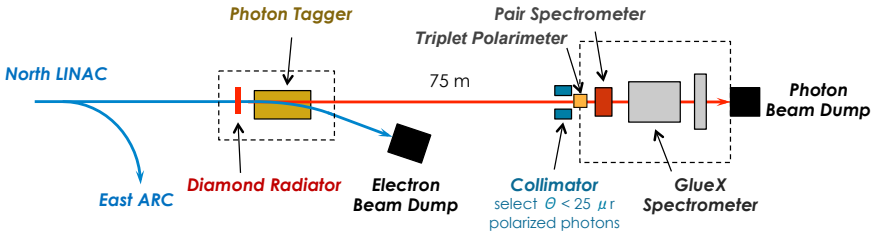

Figure 2.4: A schematic representation of the beam line and detectors. Source [38].

2.2.1 Radiator

The linearly polarized photon beam is produced via coherent bremsstrahlung process using a properly alligned 50 μm thick diamond crystal placed in the the electron beam. At the end of the of the LINAC there are two beam position monitors which monitor the electron beam position at the radiator [41]. When the incident electron beam is aligned in special orientations with the crystal lattice of the diamond radiator, a small number of these reciprocal lattice vectors can be picked out resulting in spectrum of photons composed of only a few distinct angles and energies. Depending on the energies involved and the angle at which photons exit the diamond, the beam is partially linearly polarized. A multi-axis goniometer as shown in Figure 2.5 holds the diamond radiator that produces coherent bremsstrahlung. It enables accurate movement and the diamond can be aligned to create optimal beam polarization at the appropriate photon beam energy. The orientation can be further modified such that only the lowest-energy photon peak dominates the spectra. Linear polarization parallel to the floor are referred to as PARA (0^0), PARA (-45^0), and perpendicular

to the floor as PERP (90^0), PERP (45^0). Thus a monochromatic, partially polarized photon beam is generated from an incident electron beam.

Figure 2.5: A picture of the goniometer. The diamond radiator is mounted in the centre. [41]

We can therefore preferentially select, or collimate, only very forward photons to reduce the relative number of incoherent bremsstrahlung photons and improve the overall polarization of beam to Hall D. A lead block 75 m downstream from the diamond radiator with a 5.0 mm diameter hole helps to select photons with $\theta <$ 25 μr. An example beam energy spectrum before and after collimation is given in Figure. After collimation, the degree of linear polarization for the outgoing photon beam around 9 GeV is about 40%.

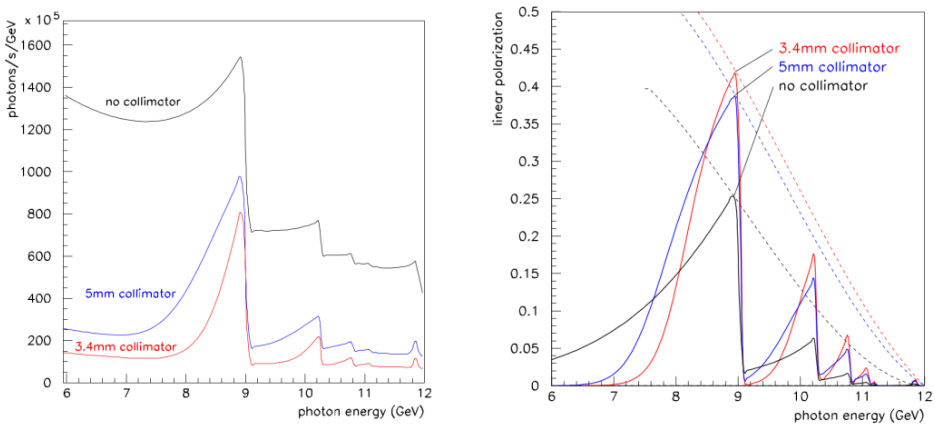

Figure 2.6: These plots show the enhancement of collimation on the distribution of the energy and the polarization fraction of the beam thus reducing unpolarized incoherent bremsstrahlung radiation. [41]

2.2.2 Tagger

In order to measure the energy of photons produced from the radiator, a tagging system comprising of tagger microscope (TAGM), tagger hodoscope (TAGH) and a 1.5 T tagger dipole magnet is used [42] as shown in Figure 2.7. The TAGM is a set of scintillation detectors read out by silicon photmultipliers (SiPMs) and measures energies between 8.1-9.1 GeV. The TAGH comprises of scintillation counters read out by photomultiplier tubes and measures energies from 3.05-8.10 and 9.10-11.78 GeV. The scattered electrons are bent in the tagger magnetic field and the radius of bending thereby momentum is measured by TAGH and TAGM. With the known energy of electron beam incident on the radiator and the momentum of scattered electron, the energy of the outgoing photon is calculated.

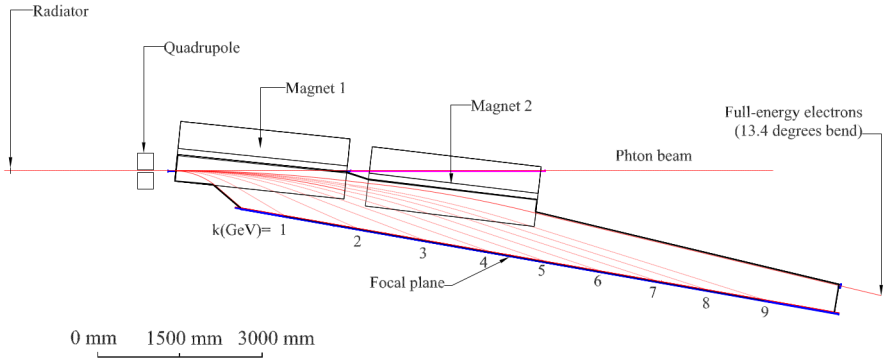

Figure 2.7: Schematic view of the tagger hodoscope and microscope. The bent electrons are shown in bent red lines which are then detected by focal plane detector arrays of TAGH and TAGM shown in blue. Source [13]

2.2.3 TPOL

Triplet polarimeter (TPOL) measures the polarization of the photon beam using the triplet photoproduction process: $\gamma\ e^-\ \rightarrow\ e^-\ e^+\ e^-$ This is a calculable QED process where the total cross section σ_t is given by [43],

$$\sigma_t = \sigma_0[1 - P\Sigma cos(2\phi)] \tag{2.2.1}$$

where σ_0 is the unpolarized cross section, P is the photon polarization, Σ is beam asymmetry of the process, ϕ is the azimuthal angle of the recoil electron relative to the plane of the photon's polarization. The photon γ scatters off an atomic e^- in a beryllium radiator. The scattered e^- is then detected in the TPOL [43] and the produced e^+ e^- pair is detected in the pair spectrometer. Measuring the azimuthal angular distribution ϕ, yields a measurement of the photon polarization P. A 75 μm thick Be converter is used as the electron target for the triplet scattering. The scattered electron is detected in a silicon detector that is disc shaped and segmented into 30 wedges as shown in Figure 2.8.

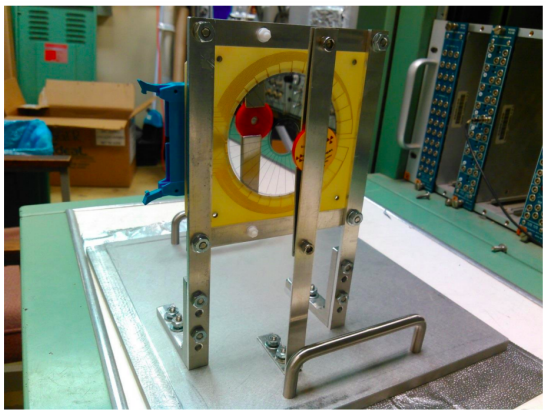

Figure 2.8: A photo of the TPOL face is shown with the disc shaped silicon detector. Source [13]

Measuring counts per azimuthal angle allows extraction of the linear polarization as a function of the beam energy which is shown in Figure 2.9.

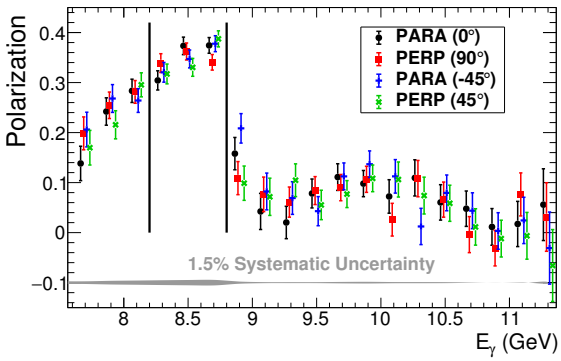

Figure 2.9: Plot displaying the photon beam's polarization fraction as a function of energy, as determined by the triplet polarimeter for the four polarization orientations for 2017 runperiod data: PARA (-45^0), PERP (45^0) on the right, and PARA (0^0, parallel to the floor), PERP (90^0, perpendicular to the floor) on the left [44].

2.2.4 Pair spectrometer

In order to measure the photon beam flux, the GlueX experiment uses a Pair Spectrometer (PS) by measuring the produced pairs from the beryllium foil converter of the TPOL [45]. The PS is located just after the TPOL and the e^+ e^- pairs originating from the TPOL foil are used for the measurement as shown in Figure 2.10.

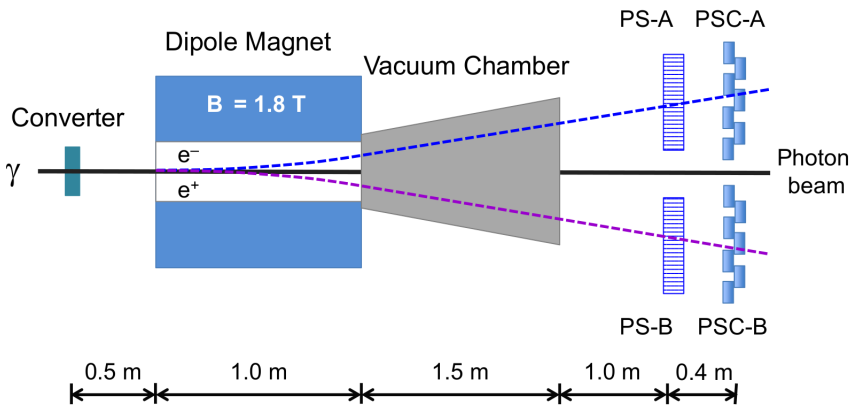

Figure 2.10: Diagrammatic representation of the pair spectrometer used at GlueX. Source [13]

A dipole magnet of about 1.8 T is used to bend the pair depending upon their energies into trajectories. These pairs are then detected by two identically instrumented arms of scintillating counters. Each of the arm consists a high granularity hodoscope with 290 scintillators (PS-A/B) read out by silicon photomultipliers (SiPM) and an array of sixteen scintillators (PSC-A/B) read out by photomultiplier tubes. These detectors are well optimized to provide a trigger signal and reduce background by performing coincidence between the e^+ e^- pair. The PS also measures the energies of the pairs, which provides energy calibration for the TAGM and TAGH.

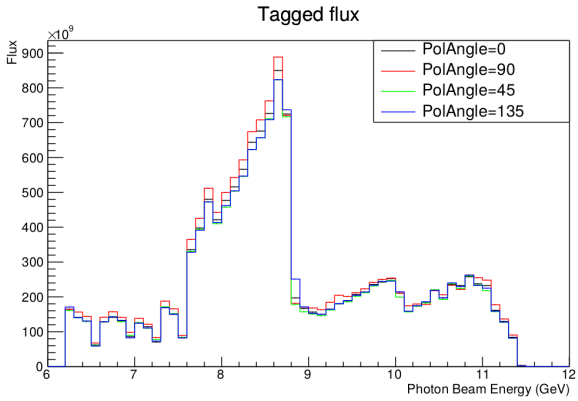

Figure 2.11: Photon beam flux as a function of beam energy for the four orientations for 2017 runperiod data.

2.3 GlueX spectrometer

The linearly polarized photon beam then impinges on the proton (i.e. liquid hydrogen) target at the center of the GlueX superconducting solenoid producing an array of particles. The charged and neutral particles thus produced are detected using a combination of timing and PID detectors, drift chambers and calorimetry as illustrated in Figure 2.12. These subsystems of GlueX spectrometer are discussed in detail in the following section.

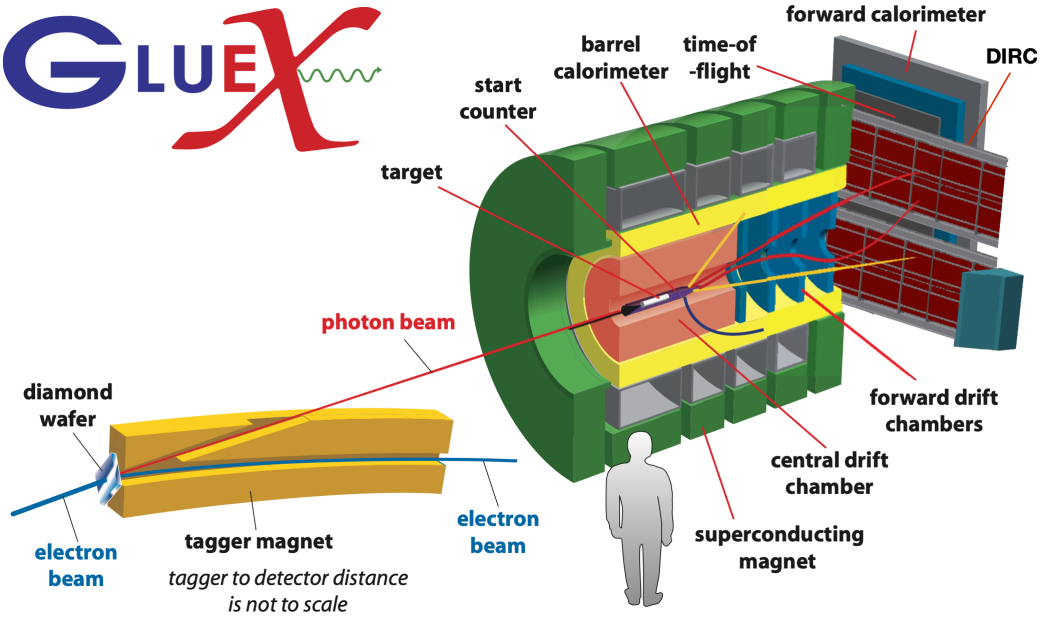

Figure 2.12: Illustration of GlueX Spectrometer. Source [38]

2.3.1 Solenoid

The solenoid magnet was originally built for the LASS experiment and operated at SLAC in the 1980s. Later it was refurbished for GlueX in the early 2000s.

The GlueX magnet is a superconducting solenoid with four coils that is operated at an operating current of 1350 A and a maximum magnetic field strength of 2T along the axial direction [39]. A liquid helium cryogenics system is used for cooling the superconducting coils. The charged particles produced bends and follows a helical path in this almost uniform magnetic field thus helping in particle identification which will be also discussed in the section of drift chambers.

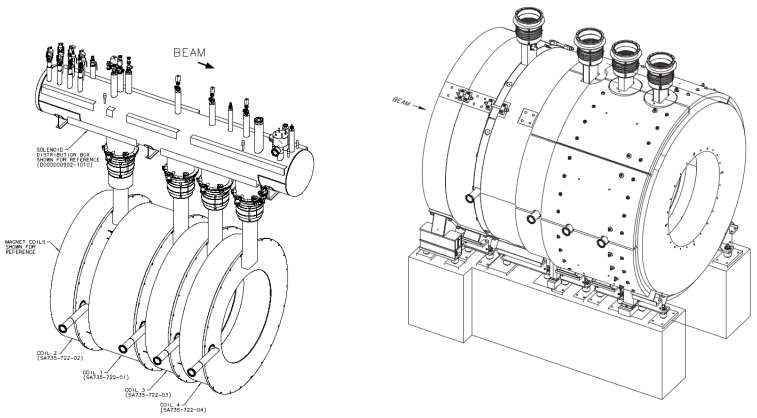

Figure 2.13: Illustration of the GlueX solenoid. The four individual coils in iron yokes are shown on the left. The assembled solenoid is shown on the right. [39]

2.3.2 Target

For the target proton, a liquid hydrogen target is used at GlueX. The gaseous hydrogen is cooled down to its liquid phase using a cooling system. This then fills a target cell of cylindrical shape that is about 30 cm long and about 1.6 cm in diameter shown in Figure 2.14. The liquid hydrogen target is kept at a density of $71.2 \pm 0.3\ mg/cm^3$ and at a temperature of 20.1 K. All of the target cell walls—aside from the entrance and exit windows, which are not aluminum—are composed of 100 μm thick aluminized polyimide foils. To stop bubbles from forming inside the cell, the target cell tapers significantly towards the forward section, forming a conical shape.

A schematic design of the target cell and the Start Counter is shown in Figure 2.15. During operational runs this entire setup on a cart is moved into the radial center of the barrel. Here the photons interact with the target and results in hadron production, for e.g. the formation of Δ^+ in the present analysis. For systematic studies in analyses, empty target runs are performed occasionally or opportunistically during the nominal running periods.

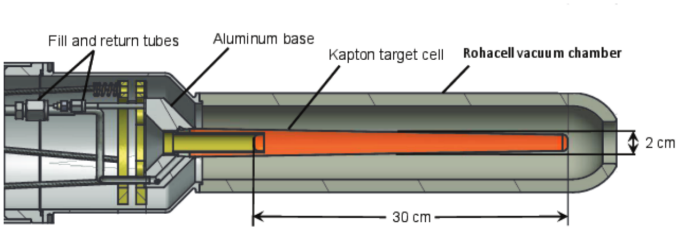

Figure 2.14: Diagram of target cell with liquid hydrogen contained in the orange-colored cone. The beam direction is from left side. Source [13]

2.3.3 Timing detectors and particle identification

Start counter

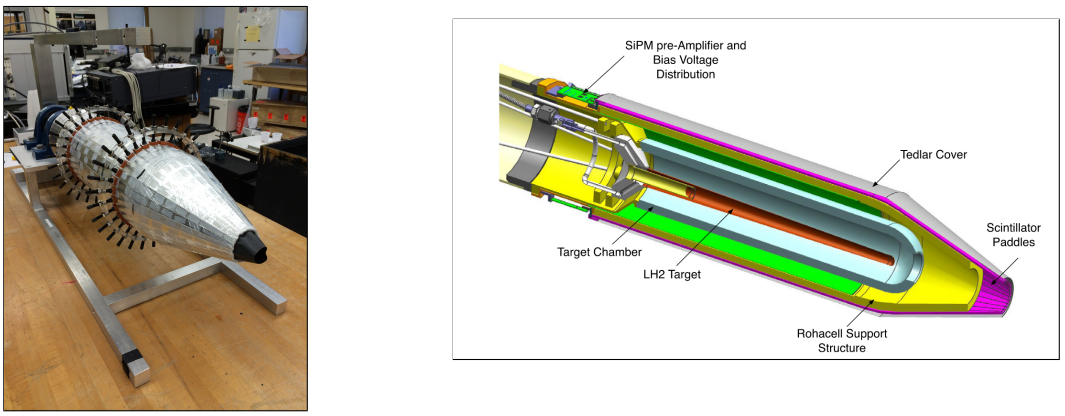

Figure 2.15: The liquid-hydrogen target assembly is surrounded by the GlueX Start Counter as shown above. The incident beam follows the central axis from left to right. [46]

The Start Counter (SC) consists of 30 scintillator strips that surround the GlueX target. In the forward direction, the strips follow a conical shape [46]. The strips are

read out using silicon photomultipliers and provide a timing signal with a precision of about 350 ps. The SC was designed to provide a time measurement close to the target that is precise enough to select from which 4 ns RF bucket the photon came. The SC is used to measure the energy loss dE/dx of charged particles as they pass through the scintillator of the SC and to determine the start time of an event that is consistent with tagged photons.

Time Of Flight (TOF)

Figure 2.16: The TOF detector in HallD mounted on its support frame. Source [38].

The time of flight (TOF) detector consists of a vertical upstream plane and a horizontal downstream plane each made from 46 plastic scintillating paddles arranged with an effective 2.52 x 2.52 m^2 area which helps to determine tracks two dimensionally and also measures the time taken by charged particles in the forward direction to arrive from the target [47]. The paddles are coupled to light guides and read out by PMTs on both ends. TOF is used to help identify and separate pions, kaons, and protons. For pions and protons, TOF can produce separation for momenta up to 4.5 GeV/c. It can also separate pions and kaons with momenta up to 2 GeV/c. Figure

2.17 shows a spectrum of calculated relativistic β factor against particle momentum which are used for PID.

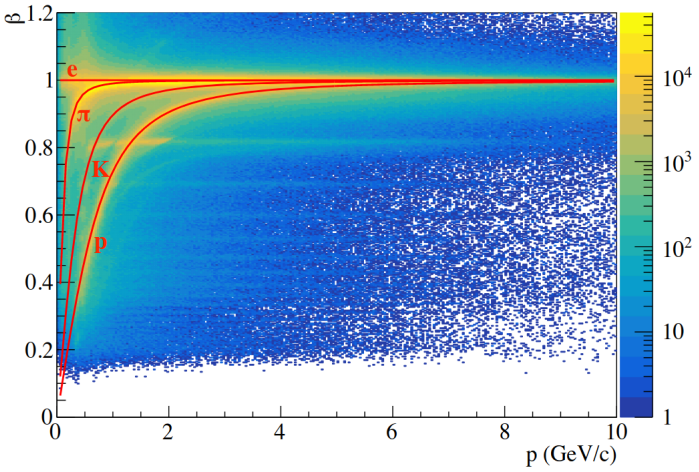

Figure 2.17: The Lorentz factor, β, measured for various particles is plotted against their momentum using 2017 data. The different yellow bands correspond to the different particles and the red curves are theoretical predictions.

2.3.4 Tracking using drift chambers

As mentioned in the section 2.3.1 the charged particles produced bends and follows a helical path in this almost uniform magnetic field. The drift chambers CDC and FDC helps to identify the radius of curvature i.e "tracking" the trajectory and thus determining the momentum of the particle.

Central Drift Chamber (CDC)

The CDC is a barrel shaped straw tube chamber comprising of 3522 tubes. These tubes have a diameter of 16 mm and are arranged in 28 layers with an alternating orientation of $\pm$ 6^0 relative to the beam axis as shown in Figure 2.18. Each straw tube consists of a 20 μm diameter gold-plated tungsten anode wire and 15.5 -mm inner diameter Mylar tube with a 100 nm layer of vapor-deposited aluminum as the cathode [48]. The active length of the CDC is 150 cm and it covers polar angles from 6^0 to 168^0 with optimal coverage from 29^0 to 132^0. The gas mixture used is 50% argon and 50% carbon dioxide at atmospheric pressure. The drift time characteristics of this mixture provide good position resolution . A small admixture (approximately

1%) of isopropanol is also used to prevent aging related loss of performance. When a charged particle travels through this gas, it ionizes the gas and generate electrons which "drifts" with a well defined velocity in the presence of an electric field. The anode wires are held at +2.1 KV during normal operation. As the freed electrons approach the wire, the high voltage further accelerates the electrons, causing a cascading effect by freeing more electrons on the way and thus producing an electric signal. The drift time taken for electrons give information on distance from a wire, which is then repeated for each straw hit and used to determine a best estimate of trajectory.

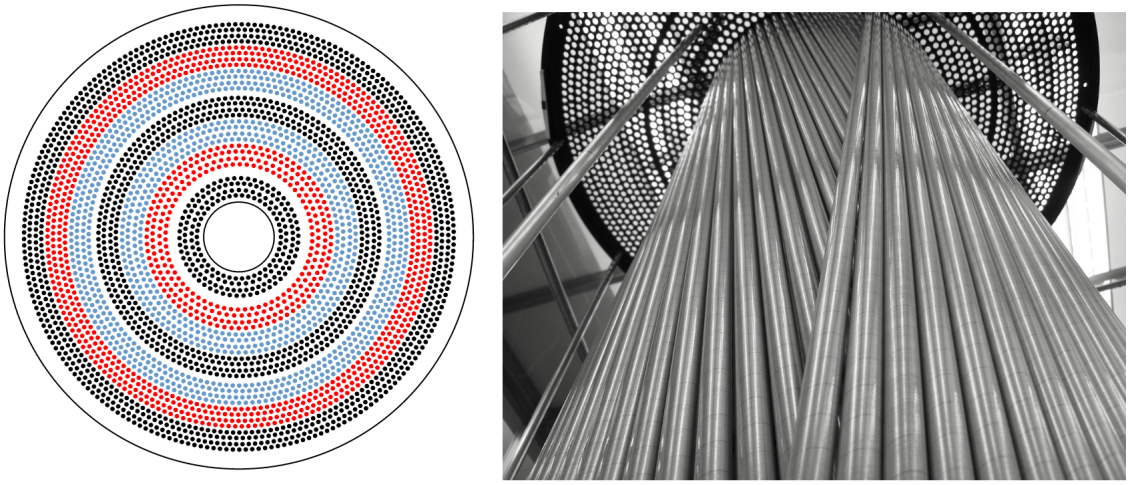

Figure 2.18: Left: figure showing CDC layers. Axial layers (parallel to beam axis) are shown in black. Stereo layers with a $+6^0$ offset are shown in red. Layers with a -6^0 offset are shown in blue. Right: figure shows two of the layers during construction of the detector. Source [13]

The CDC with the information on distance traveled, also gives the information on energy loss of charged particles thus together giving dE/dx i.e. the amount of energy lost by the charged particle per unit distance in the gas. This quantity is helpful for distinguishing between protons and lighter charged particles at low momenta.

Forward Drift Chamber (FDC)

The FDC detects particles emitted into polar angles as low as 1^0 and up to 10^0 with all the chambers, while having partial coverage up to 20^0 [49]. It consists of 24 disc-shaped planar drift chambers of 1 m diameter which are grouped into four packages, as shown in Figure 2.19. Each of the four FDC packages contain six sets of wires and planes, with each set in a package rotated 60^0 from its neighbors. This setup provides a spatial resolution of about 200 μm. A gas mixture of 40% argon and 60% carbon dioxide is used in the chamber. A positive high voltage of about 2.2 kV is applied to the sense wires and a negative high voltage of 0.5 kV to the field wires. The working principle is similar to that of CDC having the charged particle causing the drifting of electrons in the gas mixture and subsequent production and detection of electric signal.

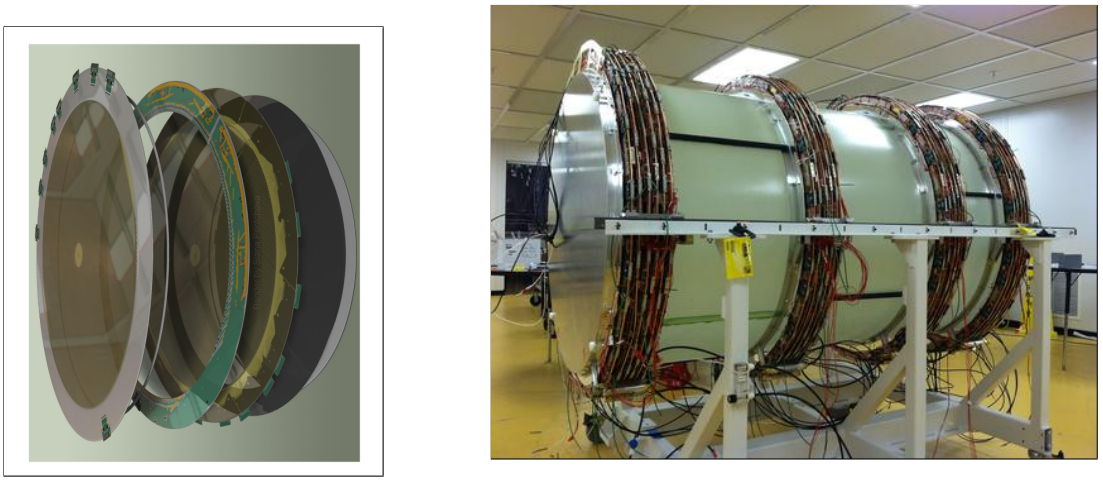

Figure 2.19: Left- Schematic representation of the FDC chamber showing the components. Right - The four mounted packages of FDC chamber. Source [13].

Forward tracking requires good multi-track separation due to the high particle density in the forward region. The additional cathode strips on both sides of the wire plane allow for a reconstruction of a space point on the track from each chamber as shown in Figure 2.20.

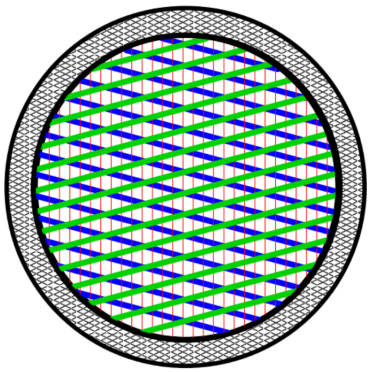

Figure 2.20: Front view of an FDC package. Red vertical lines represent the anode wires with the two cathode strip planes Upstream (green lines) and Downstream (blue lines) on either side of the wires rotated by $\pm 75^0$ with respect to the vertical. Source [13].

2.3.5 Calorimetry

Barrel Calorimeter (BCAL)

The BCAL is a cylindrical shell made up of 48 modules, as depicted in Figure 2.21.

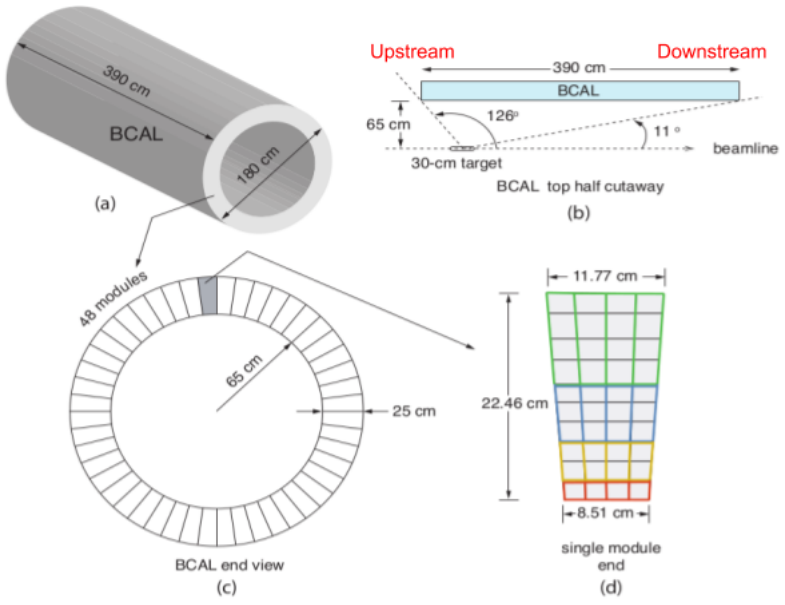

Figure 2.21: Sketch of Barrel Calorimeter readout. (a) A three-dimensional rendering of the BCAL; (b) top-half cutaway (partial side view) of a BCAL module showing its polar angle coverage and location with respect the GlueX LH2 target; (c) end view of the BCAL depicting all 48 azimuthal modules and (d) an end view of a single module showing the readout segmentation. Source [50].

Each module is made of alternating layers of scintillating fibers and lead. Particles hitting the fibers produce photons that travel through to silicon photo-multipliers (SiPMs) connected to the fibers on either side of the BCAL [50]. Each module is connected to a matrix of four sectors by ten layers of SiPMs. Layer 1 is made of the first inner layer of SiPMs. Layer 2 is summed over the next two layers, Layer 3 is summed over the following three layers and Layer 4 represents the sum over the outer four layers, as shown with different colours in panel (d). As a high energy photon enters the BCAL, it interacts primarily with the heavy lead nuclei through pair production. The produced electron-positron pair interacts again with the lead nuclei to produce bremsstrahlung photons, which then further pair produce electron -positron pairs, creating an electromagnetic shower. These excite the molecules in the scintillating fibers which emit optical photons on deexcitation. The energy loss of electrons and positrons in the shower is proportional to the scintillation light that is gathered, and this energy loss can be linked to the high energy photon that started the shower. The BCAL is between 15.3 and 67 radiation lengths thick, depending on the photon's incident angle. The SiPMs read out the light from a single shower, allowing the photon energy to be determined. Details on the SiPMs and the LED system to monitor the relative gains of the SiPms will be discussed in the next chapter. The energy resolution of the BCAL is given by the equation [50]:

$$\frac{\sigma_E}{E} = \frac{a}{\sqrt{E(GeV)}} \oplus b \oplus \frac{c'}{E(GeV} \tag{2.3.1}$$

where the symbol $\bigoplus$ means that the quantities are added in quadrature. The $\frac{\sigma_E}{E}$ term contains the combined effect of sampling fluctuations and photoelectron statistics, with the former dominating the resolution. This is commonly referred to as the stochastic term. The constant term, b originates from sources with uncertainties that scale with energy. These sources can be mechanical imperfections, material defects, segment-to-segment calibration variations, instability with time and shower leakage. The term $\frac{c'}{E(GeV}$ results from noise and pileup in high-rate environments.

Forward Calorimeter (FCAL)

As seen in Figure 2.22, the FCAL is a homogeneous electromagnetic calorimeter shaped like a wall in the forward region. It is made up of 2,800 lead glass blocks with a diameter of 2.4 meters that are arranged in a circle around the beamline [51]. The dimensions of each lead glass block are 4 x 4 x 45 cm^3. A PMT uses an acrylic light guide that is attached to the block through an optical interface to read out each block. A dark room encloses the detector. The photon energy range covered by the FCAL is approximately 1^0 to 11^0 in polar angle, and ranges from roughly 100 MeV to a few GeV.

Figure 2.22: Picture of the FCAL wall during construction. Source [51].

Cherenkov light is the term for electromagnetic radiation that is released when a charged particle moves faster than light across a dielectric material. The Cherenkov radiation that is created by the fast electrons and positrons in the electromagnetic

shower is detected using a lead glass calorimeter, such as FCAL. The number of produced Cherenkov photons is proportional to the path length of the charged particle. The path length of the electrons and positrons in the shower is in turn proportional to the energy loss, which is proportional to the high energy photon that initiated the electromagnetic shower. A high energy photon typically initiates a shower that hits multiple FCAL modules. Additionally, the signatures of photons and hadrons in the spatial energy deposition are distinct.

2.3.6 DIRC

Although the GlueX spectrometer consisting of detectors mentioned before can separate pions and protons efficiently, kaon identification is limited to about 1.8 GeV/c in the forward direction which led to the introduction of additional detector DIRC. The DIRC stands for Detection of Internally Reflected Cherenkov light [52]. This latest addition in 2019 helps in kaon identification possible up to about 3.5 GeV/c in forward direction, but the data from DIRC was not used for the analysis done in this thesis. The Cherenkov photons undergoes total internal reflection through silica medium which is then detected downstream by photomultiplier tubes (PMTs). The DIRC uses the total internal reflection of this Cherenkov light for particle identification.

2.3.7 Readout Electronics

The GlueX electronics implements signal conditioning, digitization, processing and read out of the detector signals [38]. With GlueX detectors, three types of sensors are used: PMTs, SiPMs, and drift chambers. PMTs are typically powered from commercially available High voltage HV power supplies and readout via coaxial cables. Silicon Photo-Multipliers, or SiPMs, are optical sensors that were created lately and mass-produced by Hamamatsu for GlueX. They require bias supplies of less than 80 V and frontend circuits. The Application-Specific Integrated Circuit (ASICs) and preamp cards used to instrument the GlueX drift chambers are made especially for

the CDC and FDC. A flash analog-to-digital converter (FADC) and Time to Digital converters are used as readout electronics. Five readout modules are used in Hall D: fADC250, fADC125, F1TDCV2, F1TDCV3 and Discriminator [38].

2.3.8 Trigger system

Reading of each and every interaction in GlueX detector system will accumulate huge amount of data resulting in storage and processing issues. The trigger condition helps in accepting high-energy hadronic interactions while reducing the background rate. The trigger conditions used are summarized in Table 2.1. The general approach is to set energy thresholds for both BCAL and FCAL as physics trigger [53]. If more than a certain energy was measured in the detectors, the analog electric signals read out are digitized using FADCs and TDCs. The digitized signals are stored in a pipeline as pulse height and integral. If the trigger condition is fulfilled, these are then readout via VME, thus recording an event.

Trigger Conditions	Inner FCAL Layers Masked
2 x E_{FCAL} + $E_{BCAL} > 1\ GeV$, $E_{FCAL} > 0\ GeV$	2
$E_{BCAL} > 1.2\ GeV$	n/a

Table 2.1: Table showing trigger conditions for spring 2018 run period [53].

2.3.9 DAQ

The purposes of Data Acquisition System (DAQ) are receiving data from electronic readout modules of detectors, building events, and writing data to disk [38]. The raw data format used is EVIO. This format was developed for GlueX with the help of a software toolkit CODA (CEBAF Online Data Acquisition), Jefferson Lab's data acquisition framework [54]. The livetime of the DAQ is in the range of 92–100 %. The deadtime arises from readout electronics and depends on the trigger rate.

2.4 Summary

All the major elements to the experimental Hall D including the production of photon beam, its interaction with the target, production and subsequent detection of particles at different subs detectors and readout electronics have been discussed. Overall its design allows for high statistics and excellent geometrical acceptance for many charged and neutral particles.

Chapter 3

BCAL gain monitoring system

3.1 Introduction

The relative gains of the SiPMs employed in the BCAL are monitored using an LED pulsing system [55]. This monitoring is done on a daily basis during every run period. While calibration using π^0 decays keeps accurate values of gains, LED monitoring have proved to be really useful in detecting very small shifts in gains. This forms the author's major service contribution towards the collaboration and will be discussed in detail in upcoming sections of this chapter.

3.1.1 LED pulser system

As mentioned in Section 2.3.5 of the previous chapter, the SiPMs are connected to its modules using light guides which are 8 cm long. At a distance of 3.8 cm, LEDs are placed in pockets on the side of the light guide [56], which are 4 mm in diameter and 2 mm deep as shown in Figure 3.1.

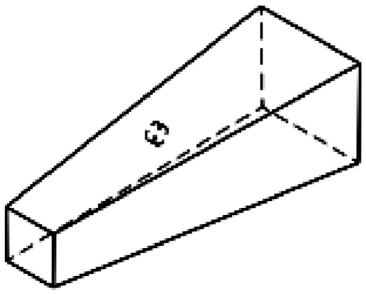

Figure 3.1: A pocket is shown on the side of a light guide where the LED is mounted on a pocket on the side of the light guide. Source [55].

Four strings of ten LEDs are attached to each module from a common control board as shown in Figure 3.2. The ten LEDs are attached to a flex cable and are pulsed simultaneously using a common trigger signal. Each string is attached to a column of light guides. The LEDs are attached in such a way that they emit light mostly parallel to light guide and toward the opposite side of the module. This light gets reflected from the near end of the module back into the near SiPM and also it is transmitted through the fibers in the module to the SiPM at the far end. Thus,

the SiPMs on both the upstream and downstream ends collect the LED pulse signal, although the intensity of pulses collected at the far end is less than that of near end due to attenuation during transmission through the entire length of the module[1].

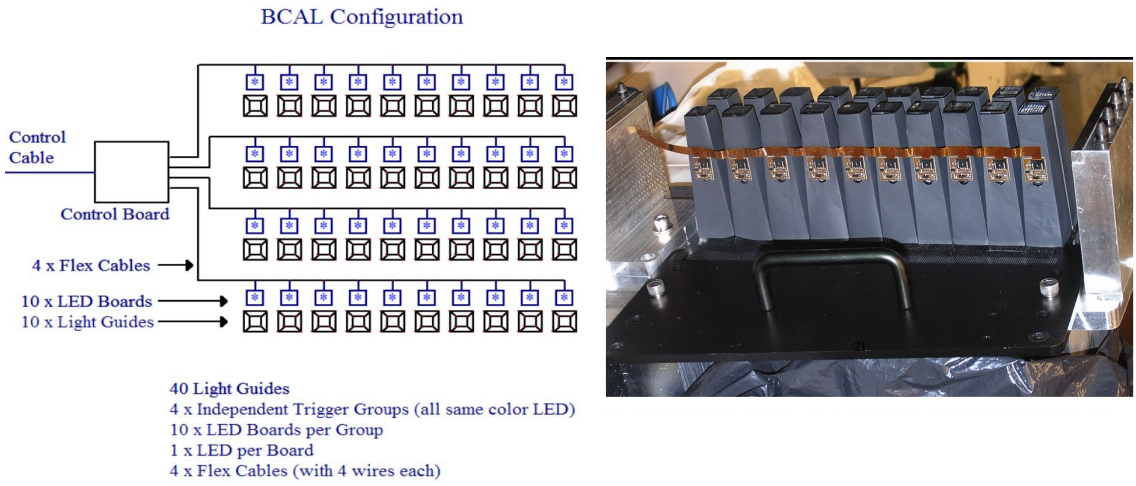

Figure 3.2: The physical layout of the controller module, LED boards, flex cable that connects them in a string of 10 are shown in left side figure while the right side figure shows mounting of one string on the light guides on actual BCAL module. Source [55].

The Analog-to-Digital-Converters (ADCs) connected to corresponding SiPMs read these LED pulses. The BCAL channels at each end first records the LED pulses as "hits". Then during data event reconstruction, the information from "hits" at both ends are stored as "point" information. Pulser data are identified using trigger information (e.g. the upstream pulser is associated with trigger bit 0x100, and 0x200 bit is for the downstream pulser) [57]. These pulse peaks are different from the physics signal in terms of energy, thus facilitating the skimming of the LED events from data. The criteria currently followed for associating an event as LED signal are the front panel (FP) triggers mentioned earlier and a minimum of 1200 hits in BCAL. The physics events (like a decay π^0 into two photons) might deposit few hundreds

[1]The design goal was 3:1 far:near, so the attenuation through whole length (1/3) made it roughly 1:1. In practice, it did not work that well due to difficulty in positioning the LEDs accurately in their pockets [56].

of MeV ($1\ MeV = 10^3\ eV$) of energy and couple of hits in BCAL. Whereas a LED event (pulsing of all upstream LEDs or downstream LEDs) will deposit at least say 12 GeV ($1\ GeV = 10^6\ eV$) energy and since the whole side with either upstream or downstream side (768 LEDs) being pulsed with the both sides having hits will result in say at least 1200 hits. Currently the skimming process is done using the HallD Online Skimming System (HOSS) and provides skimmed files after each run for monitoring. Furthermore, three triggers are also introduced:

1. Two pseudo triggers. One each for the upstream LED pulser and downstream LED pulser.

   - Upstream LED pseudo trigger- Three conditions are:
     (Energy UP > Energy DN) & (BCAL hits > 1200) & (both FP triggers(9 and 10) did not fire)
   - Downstream LED pseudo trigger- Three conditions are:
     (Energy DN > Energy UP) & (BCAL hits > 1200) & (both FP triggers(9 and 10) did not fire)

   The three conditions have to be satisfied together separately for each pseudo trigger. This allows detection of LED events if the front panel trigger has failed, but the LEDs had indeed pulsed. For example, if the three conditions of UP LED pseudo trigger are satisfied, it means that the UP LED front panel trigger has failed but the UP LEDs had pulsed.

2. 1200 hits in BCAL has been introduced as a separate trigger to check number of events with BCAL hits >1200 and compare with the BCAL LED FP triggers and BCAL LED pseudo triggers.

These triggers along with FP trigger bits have been incorporated separately in the online monitoring plot, as shown in Figure 3.3 for shift takers. If a problem is found the shift taker notifies the calorimeter expert[2] or the author and puts up a online log entry for further action.

[2]Dr.M.Dalton, Hall D Staff Scientist.

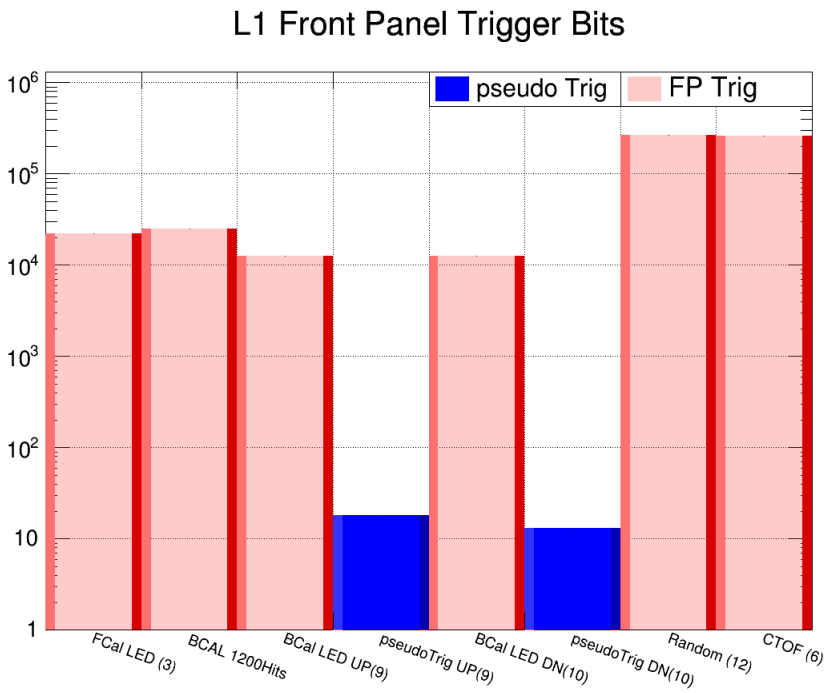

Figure 3.3: Online monitoring plot showing different LED front panel triggers. The y axis is in log scale.

3.1.2 Monitoring plugin

Skimmed files of the runs containing only the LED events are selected. The standard BCAL LED plugin (written in C++) runs over these skimmed files and produces files in ROOT format [57]. The runs with good statistics, having both upstream and downstream events, are selected first. Two-mode pulsing (Upstream and Downstream) with 6.25V results in a total of 3072 plots (1536 channels times two modes). These monitoring plots are produced using macros where the relative gain of PSPP (Pedestal Subtracted Pulse Peak) is plotted against run number for each channel, as shown in Figure 3.4, and then checked for deviation of the gain from unity. The relative gain is defined as deviation from a ratio of 1 for both Up and Down channels belonging to the same BCAL cell, which could indicate a problem with the associated LED. Likewise, a deviation in a channel (Up or Down) while the opposite one does not deviate could indicate a problem with the SiPM. Super ratios of Up/Down for both LEDs firing have been formed in the past. The accepted deviation is <5% from unity. Apart from these, there are also diagnostic plots including plots to check which quadrants have

been fired, plots comparing the trigger information of both upstream and downstream and occupancy plots.

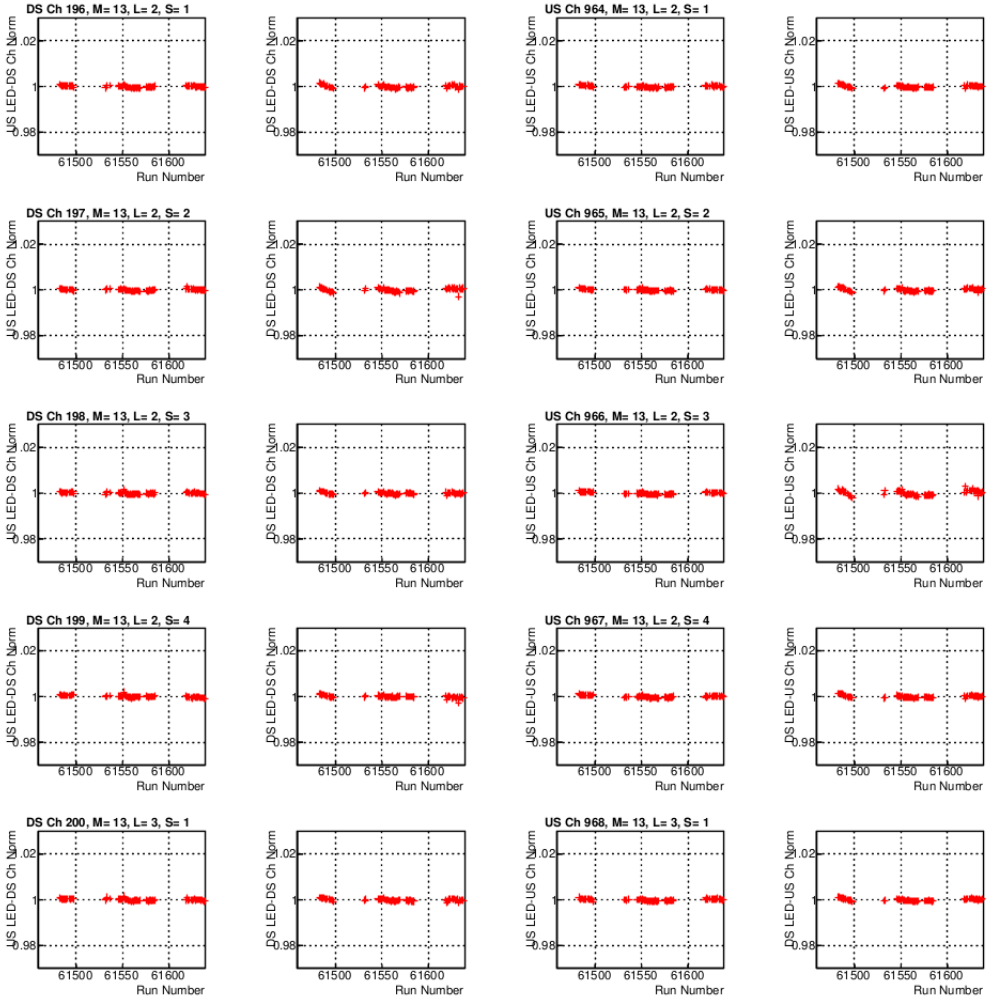

Figure 3.4: Normal looking plots from spring 2019 data set. The gain of average PSPP values (for particular run) over the average PSPP value for the entire run is plotted. The first two columns correspond to downstream channel and the last two corresponds to the upstream channel. The first and third column corresponds to upstream LED firing and the second and fourth downstream LED firing. Nomenclature: UP LED- DN Channel, DN LED- DN Channel, UP LED- UP Channel, DN LED- UP Channel respectively. The relative gain (y axis) is plotted against run number (x axis). Y axis ranges from 0.95 to 1.03. It can be seen that for these 10 channels, the deviations are negligible.

3.2 LED monitoring 2019-2022

3.2.1 Spring 2019 dataset

Runs from 61459 to 61639 were analyzed. Ten among the 1536 channels had large deviations which were reported in [58]. Eight of these channels belong to layer 4 and the remaining two are from layer 3. These channels were performing well in previous run periods. They are listed in Table 7.4 and the associated plots are shown below in Figure 3.5.

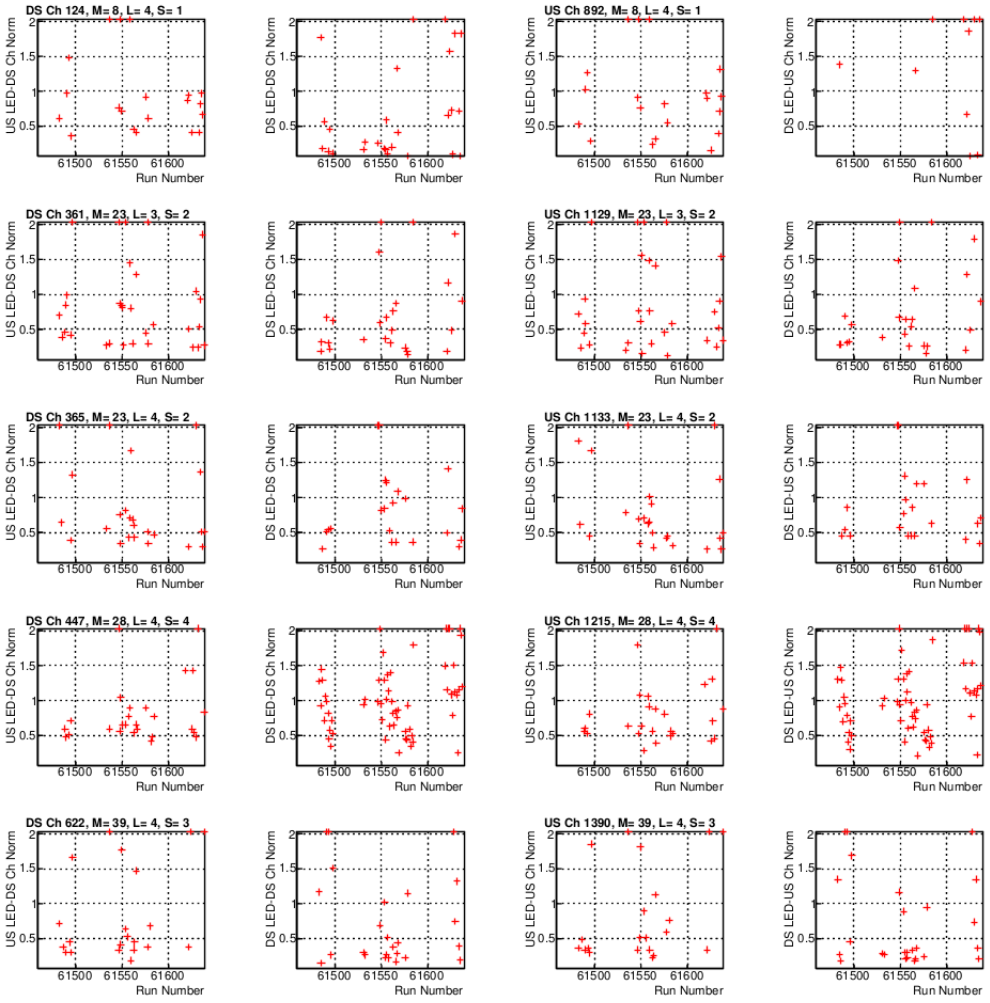

Figure 3.5: The gain of average PSPP values (for particular run) over the average PSPP value for the entire run is plotted against run number. Here the y axis is zoomed in, ranging from 0 to 2.

Channels with deviations				
Module	Layer	Sector	Channel Number	Side
8	4	1	124	DN
8	4	1	892	UP
23	3	2	361	DN
23	3	2	1129	UP
23	4	2	365	DN
23	4	2	1133	UP
28	4	4	447	DN
28	4	4	1215	UP
39	4	3	622	DN
39	4	3	1390	UP

Table 3.1: List of channels suffering from large deviations, with a ratio off from unity by >5%.

To further diagnose potential issues, plots of these channels with PSPP were also made in addition to the ratio plots. They are given in Figure 3.6. It was observed that these SiPM channels exhibited similar patterns for a particular LED indicating large fluctuations in the LED pulses.

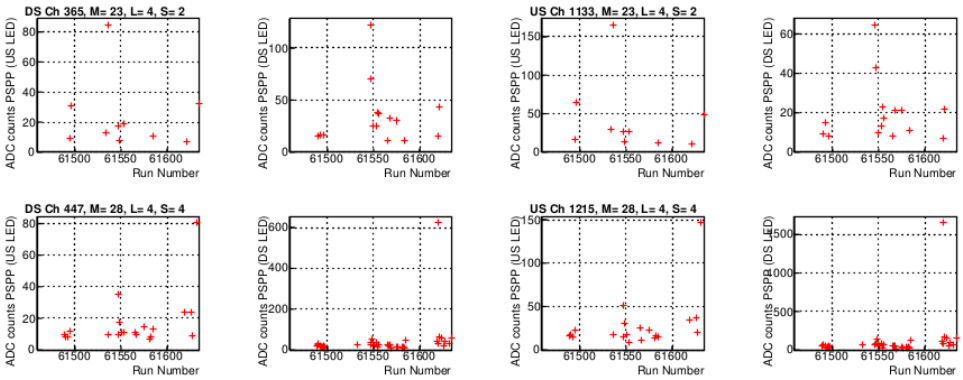

Figure 3.6: Plots of the 10 channels showing large deviation. It can be observed that the plots corresponding to same LED but different channels (first and third columns, second and fourth columns) have similar patterns indicating fluctuation in LED pulses.

Though we have found large deviations for the 10 channels in spring 2019 data, possibly due to LED fluctuations, these fluctuations were seen in other run periods

with much less magnitude. These channels are described further in the list of LED fluctuations discussed in section 3.2.4

3.2.2 Reflections

Reflections of pulses at one end of the BCAL and detection at the other end, had been studied by E. Smith [59]. As part of diagnostic studies, 10 runs (70131 to 70140) in raw mode (mode 10) were taken in fall 2019. Mode 9 contains the pulse integral, time information (coarse and fine times), pulse peak amplitude, pedestal sum, and time over threshold [60]. Mode 10 is the same as Mode 9 but contains the pulse waveforms for raw data. Detailed specifications of the fADC and modes are given in [60].

- The upstream LEDs were pulsed with bias voltages increasing from 6 V to 7 V in steps of 0.25 V and were recorded in run numbers 70131 to 70135.
- The downstream LEDs were pulsed with bias voltages increasing from 6 V to 7 V in steps of 0.25 V and were recorded in run numbers 70136 to 70140.

For each run, the LEDs were pulsed 1000 times thus creating 1000 entries for each channel. The additional window raw data gives the opportunity to look at the ADC pulse wave form for a particular channel for a single event, as shown in Figure 3.7a. The waveform for some channels had double peaks as shown in Figure 3.7b(b).

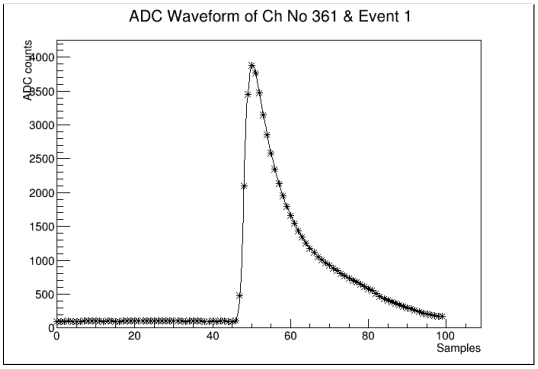

(a) Single peak of a channel for a particular event

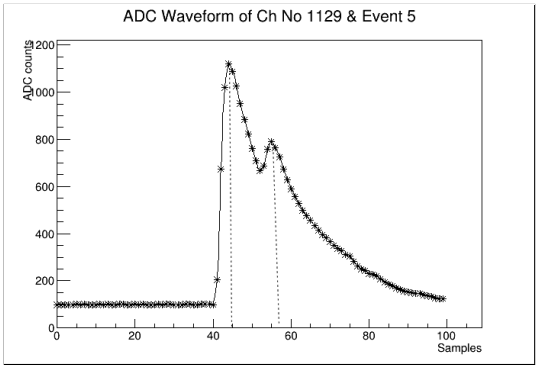

(b) Channel showing double peak for a particular event

Figure 3.7: The ADC pulse wave form for two opposite channels in the same BCAL cell for a particular event. The time difference between two adjacent samples is 4 ns. Here the peaks are 11 samples apart (shown using dotted lines in Fig(b)) so the time difference between the peaks is ≈ 44 ns.

As a further check on possible cross talk as a cause of double peaks, special runs where single sector is pulsed were taken. Double peaks were not observed in adjacent sector as shown in Figure 3.8 which ruled out the possibility of cross talk.

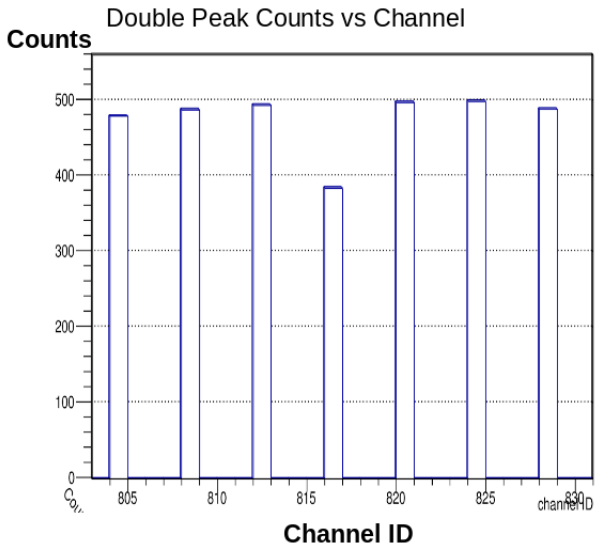

Figure 3.8: Histogram of double peak counts over channel number when upstream LEDs of Sector 1 were pulsed with 6.25V. It can be clearly seen that there are no double peaks in the channels of adjacent sectors. For example 3 channels adjacent to 804 which belongs to three different sectors did not have any double peaks.

600754 events with double peaks were found during this specific study. The histogram of the time differences for all these double peaks is given in Fig 3.9. Since the time difference between two samples is 4 ns, the time difference between the peaks can be found from the values of the samples corresponding to first and second peak. Most of them were either 11 samples or 10 samples apart, thus resulting in the two peaks. Multiplying by the 4 ns resulted in either 40 ns or 44 ns time difference. Assuming the effective velocity for propagation of signal $V_{eff} = 17$ cm/ns as mentioned in [59], the time taken to transverse the entire length of the BCAL module will be approximately 23 ns. So the pulse can take approximately 46 ns to reach back the near channel after reflection. This is close to what we have found earlier, thus confirming the process of reflection in the formation of double peaks. This study just confirms the results in [59].

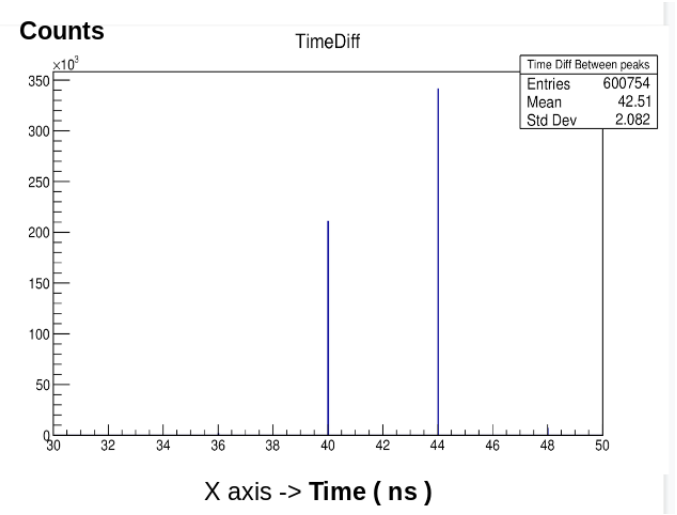

Figure 3.9: The histogram showing the distribution of time differences between first and second peaks. The number of entries are the 600754 events with double peaks.

With the lower bias voltage we usually observe peaks below the ADC count of 4096 especially with 6 V and 6.25 V. Anything above 4096 saturates to 8191. As we increase the bias voltage, we observe waveform with saturated peak as shown in Figure 3.10. This was of lesser concern, since 6.25 V is the nominal LED bias voltage during operational runs and the saturated peaks mostly seen with higher bias voltages.

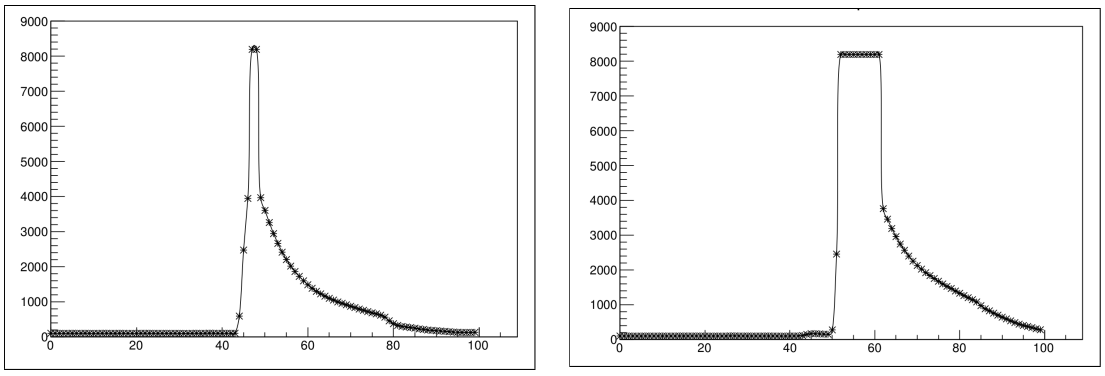

(a) **(b)**

Figure 3.10: Saturated Peaks at ADC count 8191 observed with Channel 108 from runs with bias voltage 6.5 V in Fig(a) and 6.75 V in Fig(b) respectively.

3.2.3 Fall 2019 - spring 2020

The LED monitoring is done on a daily basis to monitor the SiPM gains. Only about 10 runs per day with 1000 LED events are needed to monitor the gains. Any drift in

gain for a channel can be easily seen using the LED monitoring.

The absolute calibration of BCAL is carried out using π^0 particles. This is usually done at the end of each run period or in batches in order to have adequate statistics. Each batch might correspond to particular run condition, such as a different beam current. This process is laborious, time consuming and provides the condition of gains only after a run period.

In other words, LED monitoring has been proven to be really useful during each run period. This is best illustrated during a mishap that happened during the fall 2019 – winter 2020 run period. On 17 Feb 2020, during routine detector maintenance in Hall D, a 1" steel alignment ball became detached from its apparatus and was swept by the the solenoid magnet, striking a BCAL connector near BCAL module 26. This did not cause any observable physical damage but narrowly missing the FDC, which could have caused major damage and a shutdown of the experiment. A drift in gain for Module 26 channels was observed using LED data with a maximum drift of 10%. Representative plots are shown below in Figure 3.11. The incident was quickly reported and followup analysis was done by experts and members of calorimetry working group using different methods which confirmed the drift in the gains of Module 26 channels.

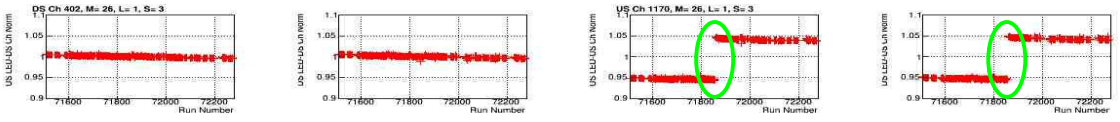

Figure 3.11: Drift in gain of 1170 channel in module 26 after the steel ball incident can be seen in the plot. The maximum of 10% shift is shown using green circles in the plot. Adjacent channels 1176, 1177 and 1200 also showed similar behavior.

A second example on the usefulness of LED monitoring was seen in the fall 2019 run period [61], which exhibited a very slight slope (<0.5%) in gain values as a function of run number as shown in Figure 3.12. This was also seen in π^0 calibration (work done by K. Suresh) [62]. This was observed for all channels, with the slope being slightly larger for downstream channels than for upstream channels. Further checks were done using temperature data of SiPM chillers during the run period but no

correlation was found with the temperature. An analysis of a different run period did not show similar trend. This drift was not reproducible.

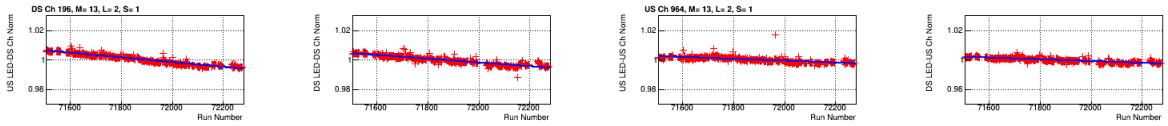

Figure 3.12: Fitted plots consisting of entire runs in the run period showing the slope for the gains (<0.5%). The Y axis is zoomed in to show the slight slope. The downstream channels (first two columns) can be seen to have slightly more slope than upstream channels (last two columns).

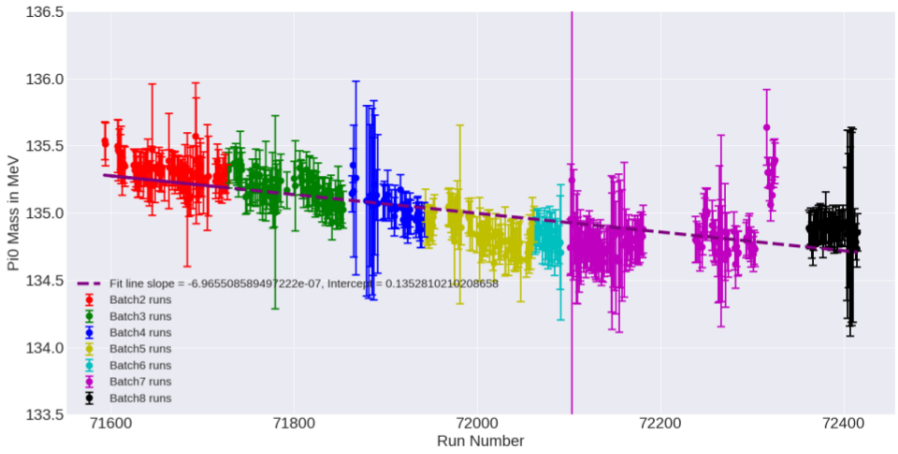

Figure 3.13: π^0 calibration plots from K. Suresh which shows slope similar to the slope found in the LED plots. The different colors corresponds to different batches used for calibration. Source [62].

A similar instance is shown in Figure 3.14, where there was a sudden change in gain which was traced back to change in run conditions. In this case the beam current was changed from 150 nA to 250 nA during run period. The apparent drift was seen in both LED monitoring and later during π^0 calibration.

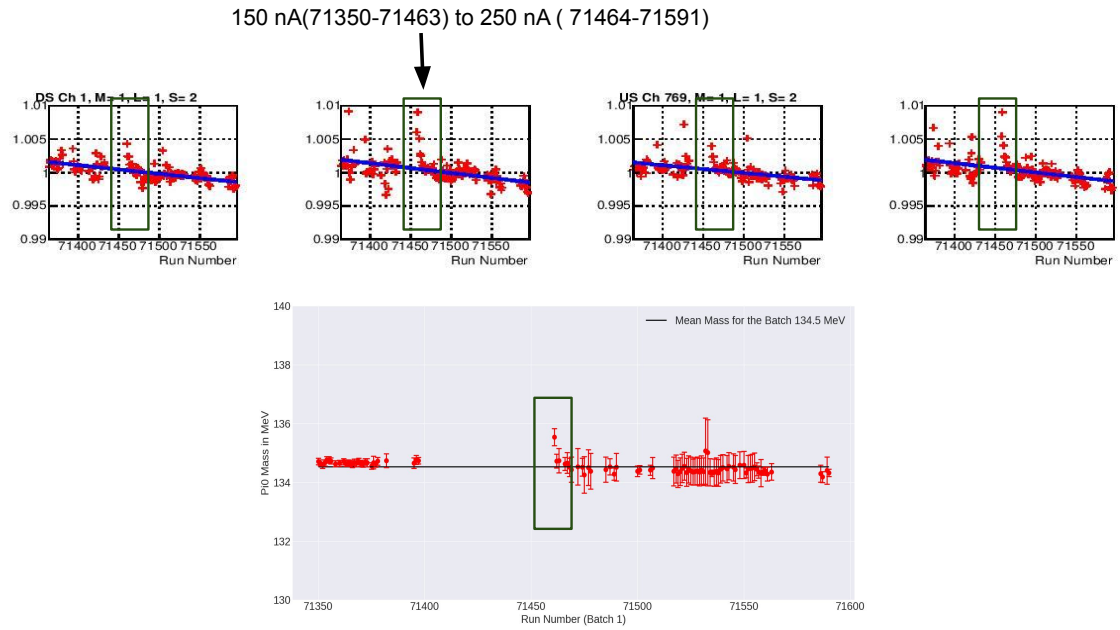

Figure 3.14: The change in current from run number 71464 can been seen (green rectangle boxes) in LED monitoring plot above and π^0 calibration plot (from K. Suresh) below.

3.2.4 General problems observed 2019–2022

If a drift is seen in both the DN and UP LEDs within a single channel while the opposite channel does not deviate, it was concluded that there is an issue in the SiPMs of that channel as shown in Figure 3.15. Overall, during the monitoring of different run periods from 2019–2022, only one out of 1536 channels have been determined to have deteriorated; this upstream channel 1118 has been already determined to be unreliable since 2017. A few other channels show occasional drifts a within the accepted threshold value of ±5%, which are immediately reported to Calorimetry Working Group to decide on the appropriate action. Those deemed to be unreliable are corrected for the corresponding runs in both data and Monte Carlo simulation (MC) data by "masking" them off. These channels are subsequently monitored closely over the run period and for different run periods. All of them, so far, are found to be stable over time without any further degradation. Sample plots are shown in Figure 3.15.

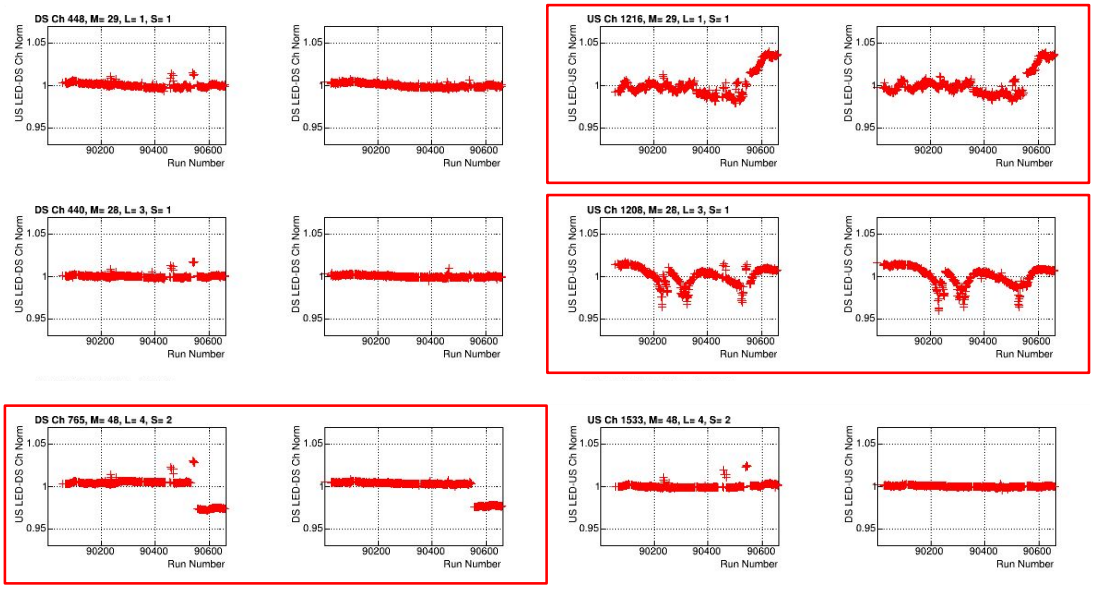

Figure 3.15: SiPM channels with drifts are shown in red boxes. Channels 1216 and 1208 are upstream channels while channel 765 is a downstream one. All have deviations within the accepted threshold value of ±5%.

Another common observation is LED fluctuations, as shown in Figure 3.16. Deviation from a ratio of 1 for both UP and DN channels belonging to the same BCAL cell could indicate a problem with the LED. The way to identify that these are LED fluctuations is by the similar patterns created by the same LED for both UP and DN SiPMs. One such instance has been discussed in detail in the Spring 2019 section in Section 3.2.1. Many other channels had shown issues with the LEDs over the run periods. The fluctuations are random, as seen in the Figure 3.16.

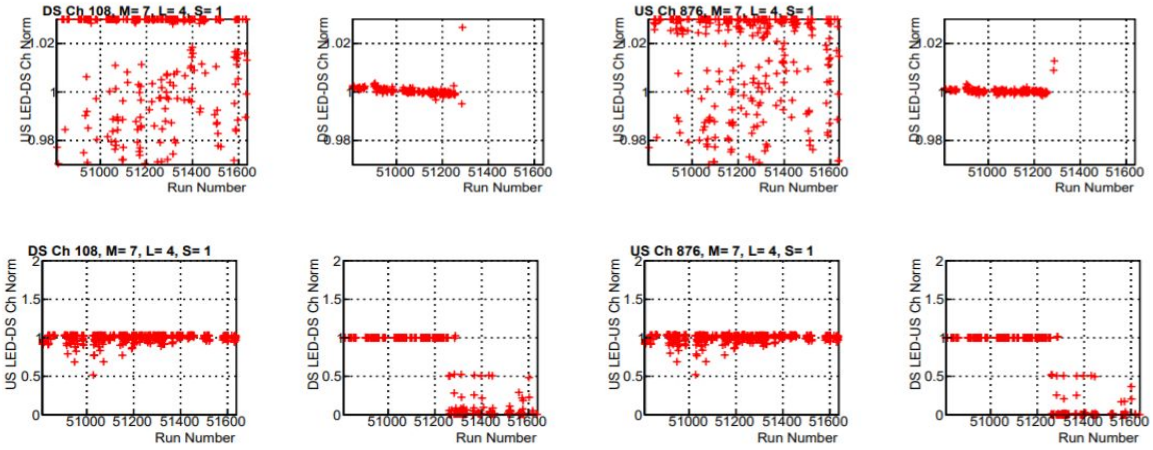

Figure 3.16: A selection of LED fluctuations are shown. The first and third colums in the plot correspond to UP LEDs while second and fourth columns correspond to DN LEDs. The first row shows UP LED fluctuations. The second row shows DN LED fluctuations.

Fluctuations in the DN LEDs were seen much more frequently than fluctuations in the UP LEDs. e.g., during the 2021 run period 144 LEDs had fluctuations out of which 19 were UP LED fluctuations and 125 were DN LED fluctuations. In the worst case, if one of the LED stops working, monitoring can be continued with the opposite one as this redundancy was built into the system design. Also, channels corresponding to different layers have different number of SiPMs and LEDs, as discussed in BCAL channels summing scheme in previous chapter. For example, a channel in layer 4 has 4 SiPMs and 4 LEDs. When one LED stops working, there are still 3 more LEDs remaining for that particular channel. So with the the help of these 3 LEDs, gains of that layer 4 channel can be still monitored.

3.3 SiPM dark rate study

Silicon Photo Multipliers (SiPM) have advantages such as low operating voltage, immunity to magnetic field, robustness, comparable gains with Photo Multiplier Tubes (PMTs) and smaller dimensions compared to PMTs. As a result, they are the most suitable detectors for the BCAL readout, especially being inside the solenoid of high magnetic field. Various detailed studies were conducted using Hybrid photodetectors (HPDs) and fine mesh PMTs before finally choosing SiPMs [63].

SiPMs are sensitive to temperature and their dark count rate per active unit area (basically the noise in the absence of signal) is high. So, it is important to study the SiPM dark rate since these SiPMs will be employed for years in experimental running. This study will yield information about the radiation damage caused over time.

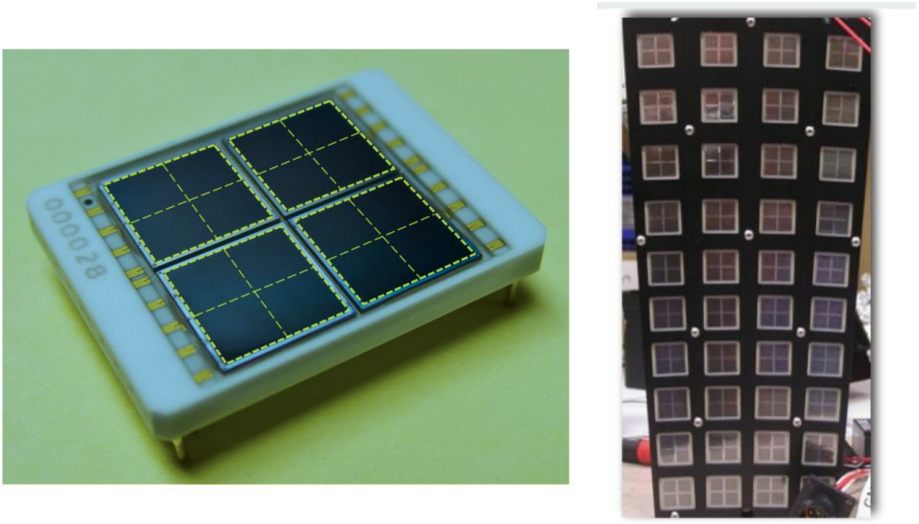

Figure 3.17: Left: photo of SiPM array Hamamatsu MPPC S12045(X) used for BCAL. Right: an array of 40 SiPMs employed in one side of BCAL module.

The BCAL readout employs Hamamatsu 16-cell SiPM photo-detectors arranged in a 4 × 4 array of cells [64] as shown in Figure 3.17, each cell has 3600 pixels (each 50μm ×50μm) all connected in a parallel electronic configuration. The 16 cells on an array are further connected in parallel for readout via a single preamp [64]. There are 3840 SiPM arrays with their preamp outputs summed in groups of 2, 3 or 4 and one row (layer1) with individual SiPMs. All are readout via flash ADCs. The gain of

the SiPM depends on the voltage above the breakdown voltage (V_{br}), which is about 70 V for these sensors. However, the operating voltage (V_{op}) is slightly above the V_{br} with the addition of overbias voltage (V_{ob}) i.e. $V_{op} = V_{br} + V_{ob}$. The V_{ob} used during experimental runs is 1.4 V.

The breakdown voltage has been determined to be a linear function of temperature over a broad temperature range. This imposes practical constraints on the operation of the SiPMs if the gain is to be kept constant during operation. It is important to stabilize the temperature and stabilize the gain within the temperature limits. This is achieved using a negative-temperature-coefficient thermistor [64]. At both upstream and downstream ends of the BCAL two chillers are installed. The coolant of the chillers is circulated through copper pipes that are in thermal contact with a plate that cools the rear side of the forty SiPMs on each module face through a silicon pad [65]. Then, using a negative coefficient thermistor in contact with the cooling plate to regulate the bias voltage, the gain is stabilized. During production running at high intensity, when we expect to see the effect of radiation damage, we plan to operate the sensors at 5°C To date, the chillers have been operated reliably down to 10°C and the electronics is flushed with nitrogen to prevent condensation. With the chiller set to 10°C, the cooling plate temperatures range between 11-12 °C and the environment inside the electronics volume results in a temperature of about 21 °C, 1–5% relative humidity and dew points less than –20°C. The coolers provide temperatures at three settings for the dark rate study: 5°C at chillers and operated at 7°C at the SiPMs, 8°C and 10°C, 16°C and 18°C, respectively.

Apart from having to deal with the temperature dependence, the possibility of radiation damage to SiPMs was also taken into account. For the expected γ ray background from simulation, tests were done with γ sources which showed no significant degradation of SiPMs [66]. Another possible radiation is the high energy neutron fluence which is equivalent to about ($\sim 10^{10} cm^2 - 1MeV$) (from simulation) over the expected lifetime of GlueX experiment which will result in degradation of SiPMs. Neutron irradiation tests conducted showed the increase in dark rate while

the gains being not affected [67]. This could potentially affect the lifetime of SiPMs. The solution that the collaboration came up with was to cool down the SiPMs to 5°C (described above) during the production runs thereby controlling the dark rate to acceptable levels during operation.

3.3.1 Method

The SiPM dark count rate (DR) is dependent on the bias voltage, temperature and active area. The DR of SiPMs can be measured by reading out waveforms not associated with pulse (termed as no-pulse) at particular V_{ob}, as shown in right part of the Figure 3.18 below.

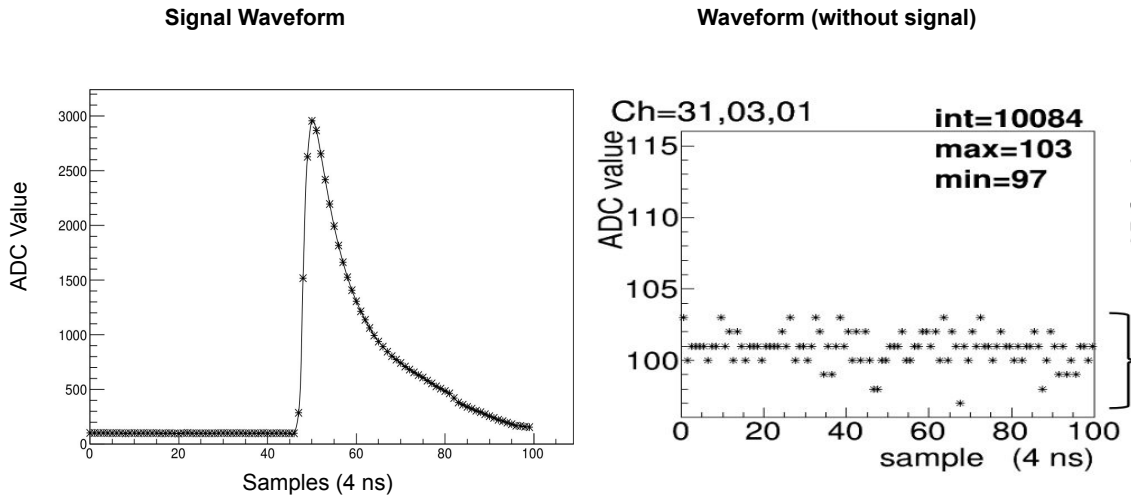

Figure 3.18: Left: Signal waveform showing peak at around 3000. Right: Sample window for a single channel without any signal but just noise. X axis:ADC sample window of 100 samples with time difference of 4 ns between each sample. Y axis : ADC values. Note that the ADC value on the y axis for no-pulse waveform is very low compared to the signal.

The mean ADC value is calculated in the sample window of no-pulse case and then is subtracted from other ADC values in the same sample window resulting in a Gaussian distribution. The DR is then related to the RMS variation about the pedestal-subtracted mean ADC value. Performing this study requires the DAQ (Data

Acquisition system) to read out all channels, rather than only reading out channels above a given ADC threshold, as normally is done. The DAQ requires a source of triggers. Currently, this is achieved by pulsing LEDs in Quadrant 3 (1000 pulses or triggers), then excluding this quadrant from later analysis. Quadrants 1, 2, and 4 are also read out as a result: but only quadrant 1 only is used in the DR analysis. This is done so as to avoid any cross talk signals in channels of quadrants 2 and 4 adjacent to quadrant 3. We take data for 12 voltage (V_{ob} = SiPMs OFF, 0.0, 0.2, 0.4, ..., 2.0 V) settings above breakdown voltage (V_{br}) and repeat for three different chiller temperatures (18°C, 10°C, 5°C); thus 36 runs are needed for this study. The waiting time for resetting the voltages is around 3 to 5 minutes. The raw data files of these 36 runs are then fed through an analysis plugin, yielding the required distributions, as shown in Figure 3.19b.

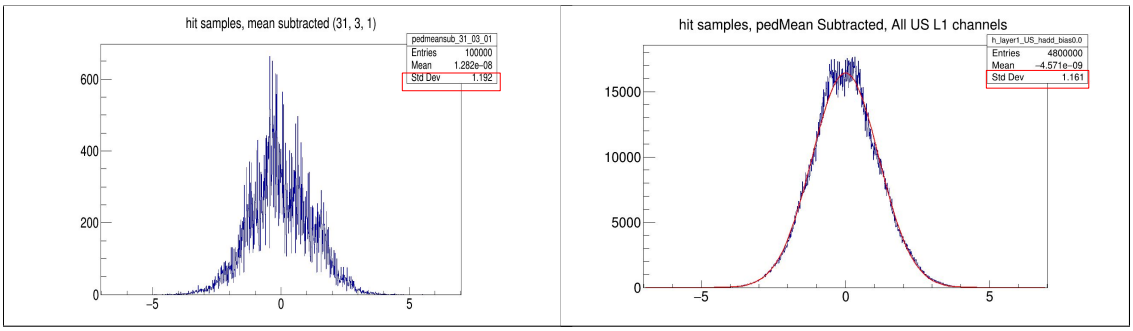

(a) Pedestal mean subtracted distribution for a Single channel.

(b) Pedestal mean subtracted distribution for a Single layer (48 channels)

Figure 3.19: The distribution Pedestal mean subtracted ADC values for 1000 pulses. There are 100 samples for each pulse, thus 100000 values for single channel as shown in the left figure and 4800000 values for a upstream or downstream layer consisting of 48 channels. The standard deviation values indicated in the red boxes are taken as the RMS variation used for this study.

After having the desired distributions, we use scripts written in python language to further analyze and compare runs [68]. A sample output plot is shown below. The first data point corresponds to the SiPM being switched off. Then from 0 (i.e SiPM switched on but 0 V over bias) the over bias voltage is increased in steps of 0.2 V until 2 V. The various colored points denote different temperatures (5°C, 10°C, 18°) and layers (1,2,3,4). It can be seen that the pedestal RMS increases with increase in

bias voltage and temperature, as expected. Also, it increases with active unit area which can be inferred from the comparison of layers.

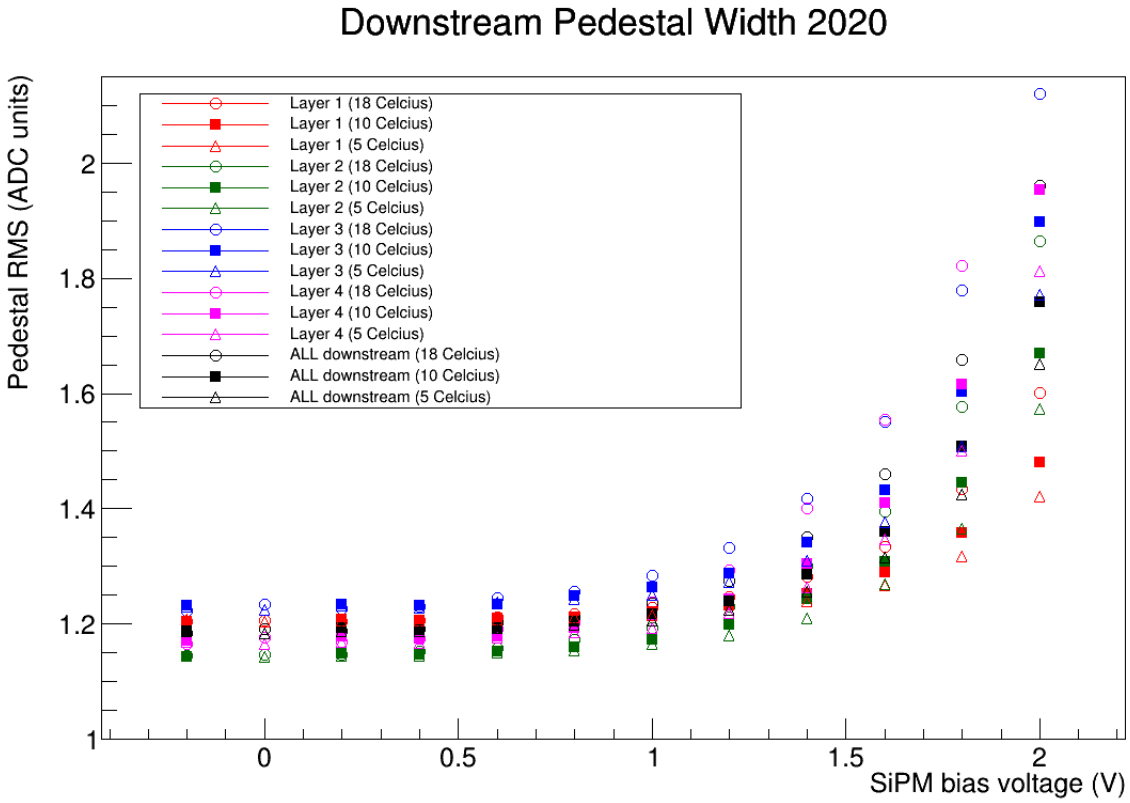

Figure 3.20: The plot shows the pedestal RMS values on the y axis plotted against SiPM over bias voltage on the x axis.

3.3.2 Results and discussion

Using the procedure discussed in the previous section, data were collected during the years 2015, 2017, 2019, 2020, 2021 and 2022. The analysis is just done before and after each run period, which might also give information on radiation damage caused during each run period. As an example, master comparison plot for data over two years (2019–2020) years is shown in Figure 3.21.

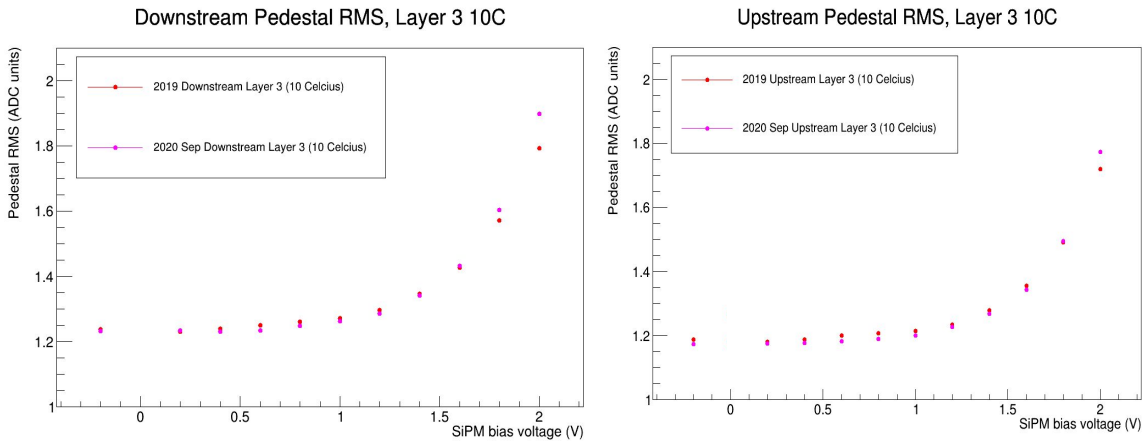

Figure 3.21: Comparison between pedestal RMS values of UP and DN layer 3 at 10^0C for 2019 and 2020 run periods.

The pedestal RMS values for DN channels (here layer 3) shown on left side plot of Figure 3.21 at given temperature and different voltages seems to be higher than the UP counterparts shown on right side plot. For example at 1.6 V the RMS value for DN is 4% higher than the UP counterparts and at 2 V it is 7% higher. This is expected, as downstream channels are more prone to degradation, because the impinging particle rate at the DN end during the experiment is considerably higher than at the UP end. A master comparison plot for data over the years (2017-2022) is shown in Figure 3.22. It can be seen in Figure 3.22 that the pedestal RMS increased over time, indicating possible radiation damage and degradation of SiPMs, although these sensors are still operating sufficiently well for the experiment. At V_{ob}= 1.4V, which is the operational V_{ob} during production runs and temperature 5°C, the operational temperature at chillers (7°C at the SiPMs) the increase is 8% .

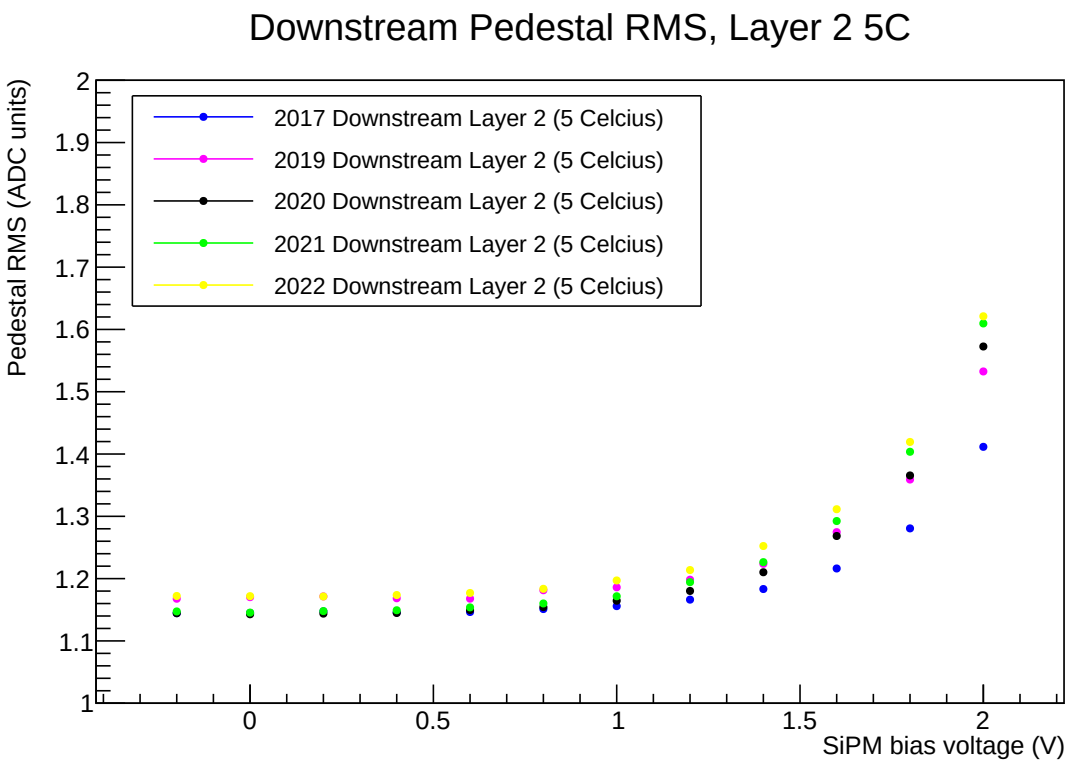

Figure 3.22: The plot shows the pedestal RMS values on the y axis plotted against SiPM over bias voltage on the x axis. The first data point corresponds to the SiPM being switched off. Then from 0 (i.e SiPM switched on but 0 V over bias) the V_{ob} is increased in steps of 0.2 V until 2 V. The different denote data from different years at same temperature 5°C.

Fluctuations in the pedestal ADC values were found during analysis. This is expected as the SiPMS are sensitive to temperature. The pedestal values also fluctuated when SiPMs were switched off. Specific runs at particular temperature and constant time intervals were taken as shown in Figure 3.23. Since these were very small fluctuations (0.5%), the calorimetry working group decided to move forward with the analysis and compare different run periods. It was also decided to have channel-wise analysis instead of the current layer-wise analysis for finer-grained detail per channel basis.

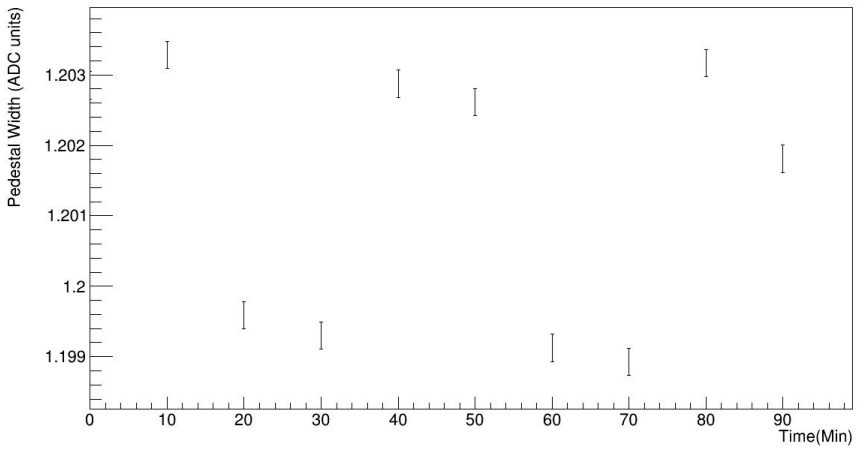

Figure 3.23: Data taken for SiPMs switched off v=off over constant time interval (t= 10 min). The y axis is zoomed to see these small fluctuations (0.5%).

This work has been handed over to another graduate student from our group.

3.4 Summary

The BCAL LED monitoring and SiPM DR study has been presented in this chapter. The author has carried out the LED monitoring work from 2019 till 2022. The LED pulser system, triggers, skimming conditions, monitoring plugin and procedure have been discussed in detail. The LED trigger plot was modified by introducing few more histograms to monitor front panel triggers and this was incorporated into the online monitoring plots for shift takers. LED fluctuations were observed in channels over the run periods. Fluctuations in the DS LEDs were seen much more frequently than fluctuations in the Upstream LEDs. At the end of 2021 run period 144 LEDs had fluctuations, out of which 19 were Upstream LED fluctuations and 125 were downstream LED fluctuations. Daily monitoring throughout runperiod proved to be really useful in detecting slight change in gains of SiPMs. So far, only very few channels have shown deviations from the accepted threshold value and one removed from CCDB and for data and MC. These are reported and well documented. A SiPM dark study was carried out by taking dedicated runs during different run periods

(2019-2022). The pedestal RMS increased over time, indicating radiation damage and degradation of SiPMs, with studies ongoing by others. This study has been useful for selecting SiPMs of calorimeter for the Electron Ion Collider (EIC) experiment.

Chapter 4

Data Analysis

The data taken using the GlueX detector systems described in Chapter 2 contains the desired physics information for the present analysis which has to be filtered out. This chapter provides a brief overview of the data taking process, subsequent reconstruction of events and preliminary analysis steps.

4.1 Spring 2018 Run Period

The run periods during which the data is taken using CEBAF are termed as "spring" or "fall" depending upon whether they are run during January to April or from September to December respectively, although occasionally the runs are extended slightly beyond this time frame.

In spring 2016, after completing the commissioning of detectors, some physics data was collected in both 0° and 90° beam polarization angles along with amorphous radiator data. The first dedicated physics data was taken in spring 2017 collecting over 50 billion triggers in total with addition of two more beam polarization angles (−45° and 45°). With the same four beam polarization angles combined, 145 billion triggers were recorded throughout the spring 2018 run period. Since the PrimEx experiment was commissioned in the fall 2018, only 78 billion triggers were recorded during this run period.

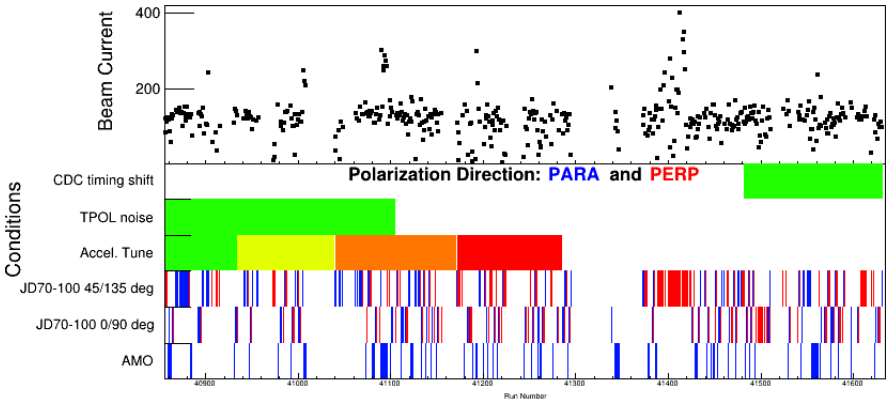

Figure 4.1: Plot showing a summary on spring 2018 run conditions [69]. The X axis is run number. The conditions on Y axis include different radiators with their orientations and different beam currents used.

Complete analysis for this thesis work is done using spring 2018 data, as it has

higher statistics, thus reducing statistical uncertainty. A specific run period is chosen at a time as the calibrations for different subsystems are carried out on run period basis. Spring 2017 and fall 2018 datasets have been used for preliminary analysis.

4.1.1 Beam polarization conditions

The polarization of the linearly polarized beam is measured using TPOL as described in Section 2.2.3. We have four beam polarization angles for the 2018 spring data. A "PARA" (parallel to x-z plane) orientation $\phi_{lin} = 0°$ and a "PERP" (perpendicular to x-z plane) orientation $\phi_{lin} = 90°$ and by analogy, two other orientations ϕ_{lin} =45° and ϕ_{lin} =−45° are also referred as "PARA" and "PERP" respectively. For the spring 2018 run period coherent peak energy is 8.8 GeV. As there is a trade off between statistics and magnitude of linear polarization while choosing the range of energy, a range $8.2 < E_\gamma < 8.8$ GeV as shown in the Figure 4.2, is commonly used for different analysis in GlueX.

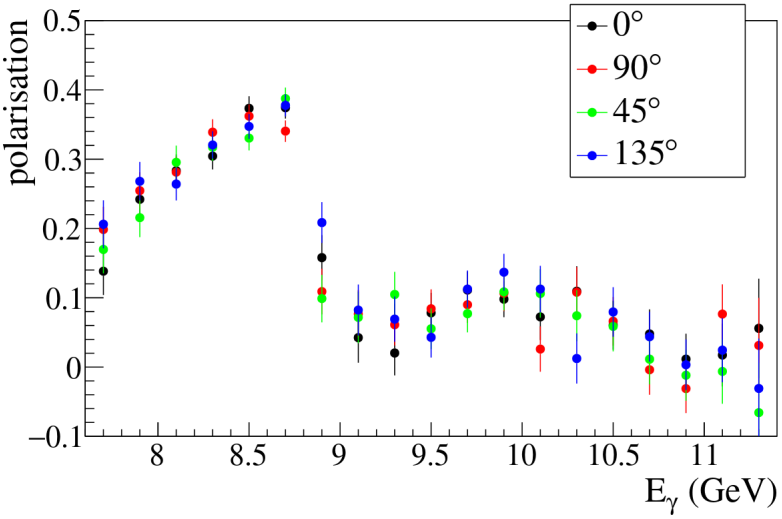

Figure 4.2: Plot showing the polarization fraction of the photon beam as a function of energy for Spring 2018 dataset, as measured by the triplet polarimeter for the four polarization angles PARA (0°, parallel to the floor), PERP (90°, perpendicular to the floor) on the right and PARA (−45°), PERP (45°) [44].

Orientation	polarization	Statistical uncertainty
0°	0.3420	0.0063
45°	0.3474	0.0065
90°	0.3478	0.0063
−45°	0.3517	0.0065

Table 4.1: Magnitude of Polarization for spring 2018 with it's uncertainties for different orientations [44].

4.2 Data acquisition

During each run period, the data were taken in terms of "runs". The time period of each run is around two hours and the data was saved across multiple files. A flowchart of GlueX data production and monitoring procedures are shown in Figure 4.3. Some of these steps including reconstruction will be discussed in subsequent sections.

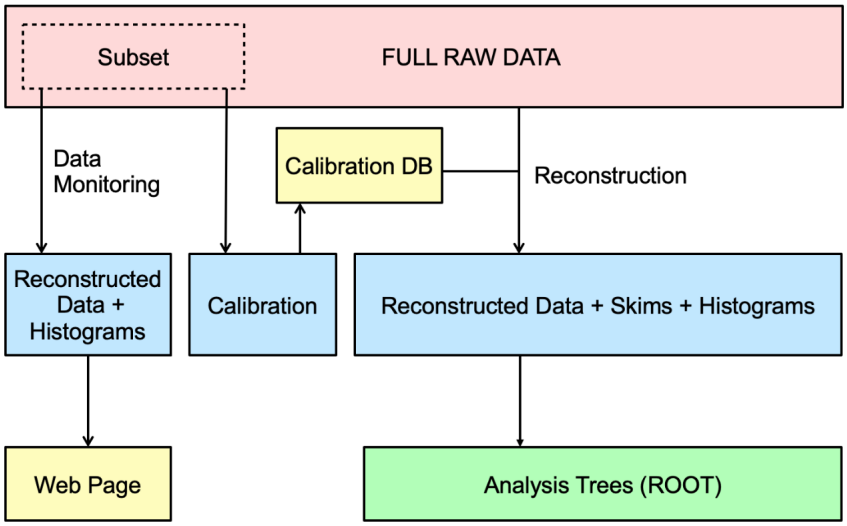

Figure 4.3: Flowchart illustrating the GlueX data production and monitoring procedures. Image source: [38]

A small number of files from each raw data run is taken as subset or sample as shown in the blocks for offline monitoring and also for low level timing calibrations of subdetectors. Once the calibration is done, the Calibration Constant Data Base

(CCDB) is updated with the calibration parameters for the sub detectors and are then used for reconstruction. These process can be repeated if necessary so as to include any improvement in reconstruction algorithms or other calibrations [38].

4.3 Event reconstruction

The analysis of this work is on the reaction channel $\gamma p \rightarrow \eta\ \Delta^+$, where η decays into two photons ($\eta \rightarrow \gamma\gamma$) and Δ^+ decays into proton and π^0 ($\Delta^+ \rightarrow p\ \pi^0$) . The π^0 decays into two photons ($\pi^0 \rightarrow \gamma\ \gamma$). Thus, the final state particles will be $\gamma p \rightarrow p + 4\gamma$. This is an "exclusive" reaction meaning all the final state particles are detected in the sub detectors.

4.3.1 Shower reconstruction

The photons are detected in the two calorimeters, BCAL and FCAL. The "hits" which are signals in the individual detector components of these calorimeters, are grouped together to form "clusters". Then the clustering algorithm will check that each cell was placed in its most appropriate cluster, which is identified based on the cell's proximity and energy relative to its original cluster and all other clusters in the event. Once the cells are gathered into clusters, the information from these cells are combined to form "showers". The energy of the shower is the sum of all of the energy deposited in each of the cells corresponding to that shower with a non-linear correction applied to the entire cluster. The shower time is determined as the energy-square-weighted average of all the cell times in the shower. The energies of the the photons are then calculated from these showers during reconstruction. The FCAL photon reconstruction is based on RadPhi algorithm [70] and KLOE algorithm is used for BCAL [71].

4.3.2 Track reconstruction

The linking of hits formed by charged particles in the drift chambers is called track reconstruction. Under the uniform magnetic field, the charged particle takes helical trajectory. The drift chambers CDC and FDC helps to identify the radius of curvature i.e " tracking" the trajectory and thus determining the momentum of the particle [72]. This information along with energy deposited in detectors and timing information helps in the identification of charged particle. This process is done in three stages. In the first stage, the linked hits within adjacent FDC packages and adjacent rings in the axial layers of the CDC are used and fitted for rough estimation of track segments. A rough estimation of fitted helical model in FDC and a circle model in CDC gives the fit parameters of track candidates.

In the second stage, these track candidates are then run through Kalman filter [73]. The general idea behind Kalman filter is an algorithm that uses a series of measurements observed over time, including statistical noise and other inaccuracies, and produces estimates of unknown variables. Here, the algorithm is developed for finding unknown tracks using known hits in FDC. The Kalman filter proceeds in steps from the hits farthest from the beam line toward the beam line. It finally provides a set of fit parameters at closest approach to the beam line. Energy loss and multiple scattering are taken into consideration at each step along the way, also considering non-uniform magnetic field at different points.

The third and last stage involves determining a start time using timing data from the Forward Calorimeter, Barrel Calorimeter, Time-of-Flight detector, and Start Counter. This allows the drift time to each wire connected to the track to be utilized in the fit. For each particle hypothesis, the drift time in tracking chambers is then used independently. After obtaining the information on charge of the particle, i.e. whether positive or negative, further particle identification can only be possible through some event selection cuts which will explained in subsequent sections.

4.4 Analysis workflow and event selection

The results from the reconstruction procedure were saved in hddm (Hall-D Data Model) files. The information of hits are no longer kept in these files and they only contain higher-level track and shower information. In order to further reduce the size of the data, and select events of particular reaction, analysis launches are performed. These are done in a group setting for the whole collaboration where some initial selection cuts are performed for reactions specified by different users. These selected events are stored in ROOT file format for further analysis by individual users.

The following selection criteria are applied during the analysis launch for $\gamma p \rightarrow \eta \Delta^+$ channel. These collaboration wide cuts are conservative and do not affect any key distribution in a significant way.

- At least one positively charged track and at least four showers in the final state;
- For a given charged track, at least one hypothesis must have a hit in either: BCAL/FCAL/TOF/SC;
- For a given neutral shower, it must at least have a shower energy of 50 MeV in the BCAL;
- For neutral showers in the BCAL, there must be hits in at least 2 cells;
- Four beam bunches before and after in-time events are saved (-18.036 < t tagger - t RF < 18.036 ns);
- A cut must be placed on the missing energy: -3.0 GeV < missing energy < 3.0 GeV;
- A cut must be placed on the measured missing mass squared: $-0.1 < —MM^2— 0.1 < GeV^2/c^4$ where the missing mass squared is given by

$$MM^2 = (p_f - p_i)^2 = (p_\gamma^{beam} + p_{proton}^{target} - (p_{proton}^{recoil} + p_{\gamma_1} + p_{\gamma_2} + p_{\gamma_3} + p_{\gamma_4}))^2 \quad (4.4.1)$$

- Loose cuts on the invariant mass of decaying π^0 and η are applied. When the combinations of photons decaying from both these particles are reconstructed and do not add up to the ranges of masses given below, they are discarded.
  - Decaying π^0 : 0.08 GeV $<$ mass of π^0 $<$ 0.19 GeV;
  - Decaying η : 0.35 GeV $<$ mass of η $<$ 0.75 GeV;
- Next, cuts are on particle timing which helps to identify and match the particles to correct RF beam bunch are applied. Selection cuts on Δt RF for both proton and photons in the ST, TOF, BCAL, and FCAL are given below:

  proton
  - Δt RF $<$ 0.6 ns TOF
  - Δt RF $<$ 1 ns BCAL
  - Δt RF $<$ 2 ns FCAL
  - Δt RF $<$ 2.5 ns SC
  - dE/dx in central drift chamber consistent with a proton

  photon γ :
  - Δt RF $<$ 1.5 ns BCAL
  - Δt RF $<$ 2.5 ns FCAL
- Finally, convergence of 4-momenta and a vertex kinematic fit are applied, which will be discussed in next section.

4.4.1 Kinematic fitting procedure

Kinematic fitting (KinFit) is a very useful tool in constraining the measured variables while using the known information (position, momentum and energy) of the particles and conservation laws of energy and momentum. As the precise information on initial states i.e. beam photon (photon energy) and target proton (rest position) is already available, this method can be used to improve resolution of measured quantities in

GlueX [74]. As we have an exclusive reaction for this analysis, the KinFit is a χ^2 minimization. The χ^2 is shown in Eq. 4.4.2

$$\chi^2 = (y-\eta)^T V_y^{-1}(y-\eta) + 2\lambda^T f \tag{4.4.2}$$

where η's are the measured and y's are fitted observables. The detector resolution encoded in an N $\times$ N covariance matrix V. Conservation of four-momentum is a constraint implemented as a Lagrange multiplier λ. The KinFit is an iterative and convergent process which varies the value of each observable to obtain the minimal possible χ^2. At the end of the process, we get a set of four momenta of particles obeying conservation laws. The χ^2 value gives information on how well the fitting procedure has performed. Two more optional requirements in these fits are that all particles originate from a same vertex (or many vertices in the case of interactions involving particles that decay over a long period of time) and that the four-momenta of the daughters of an intermediate particle sum up to a fixed invariant mass. A vertex constraint is used to constrain multiple particles, belonging to the same reaction, to pass through the same point in space, either an interaction or decay vertex.

4.4.2 Final selection cuts

The analysis ROOT files produced by skimming the reconstructed data are then run through a DSelector using ROOT framework. A DSelector is a GlueX specific analysis tool based on ROOT's TSelector. Further cuts listed below are applied at this stage to remove wrong photon combination and to improve event quality.

- 8.2 $<$ beam energy $<$ 8.8 GeV is applied to select set of events around the coherent peak of photon beam energy;
- In order to remove combinations with tracks not coming from inside the target cell, a cut is placed on the reconstructed vertex z position, 51 $<$ measured vertex z position $<$ 78 cm shown in Figure 4.4. Here, z denotes the z-coordinate of either of the particles in the final state in the GlueX lab frame;

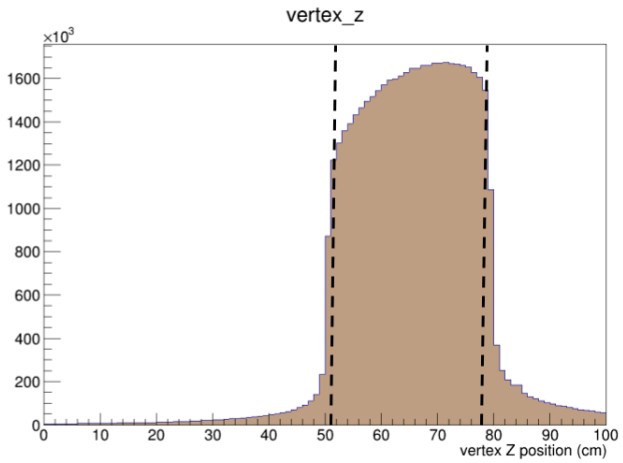

Figure 4.4: Vertex Z position distribution. The black dashed lines shows the cut placed on the distribution.

- Kinematic fit χ^2 /NDF < 10 where NDF is Number of Degrees of Freedom shown in Figure 4.5.;

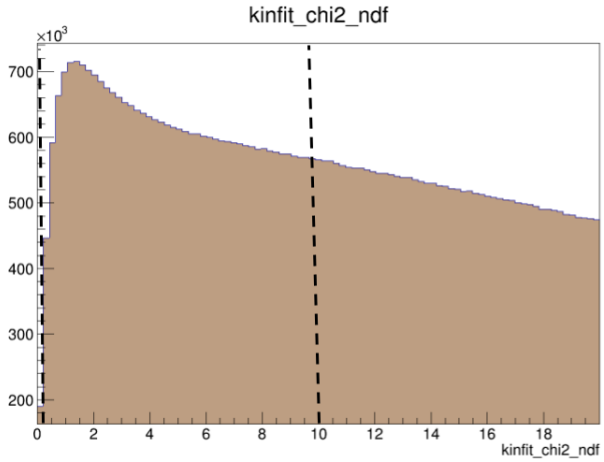

Figure 4.5: Kinematic fit χ^2 /NDF distribution. The black dashed lines shows the cut placed on the distribution χ^2 /NDF < 10.

4.4.3 Accidentals from Tagger

The CEBAF provides electron beam bunches with a 4.008 ns timing difference between them. The tagger system records multiple hits, although only one corresponded to the photon that triggered the event. This multiple tagger hits for a single event is known as accidentally tagged or "accidentals". The timing distribution of tagger events is

shown in Figure 4.6. The peak between red lines is reconstructed from correct beam bunch or "in-time" and is known as "prompt peak". The smaller four distributions i.e the side bands on either side of the prompt peak are due to accidentals or "out of time" events and are known as accidental peak. The prompt peak also contains background contributions from these accidentals.

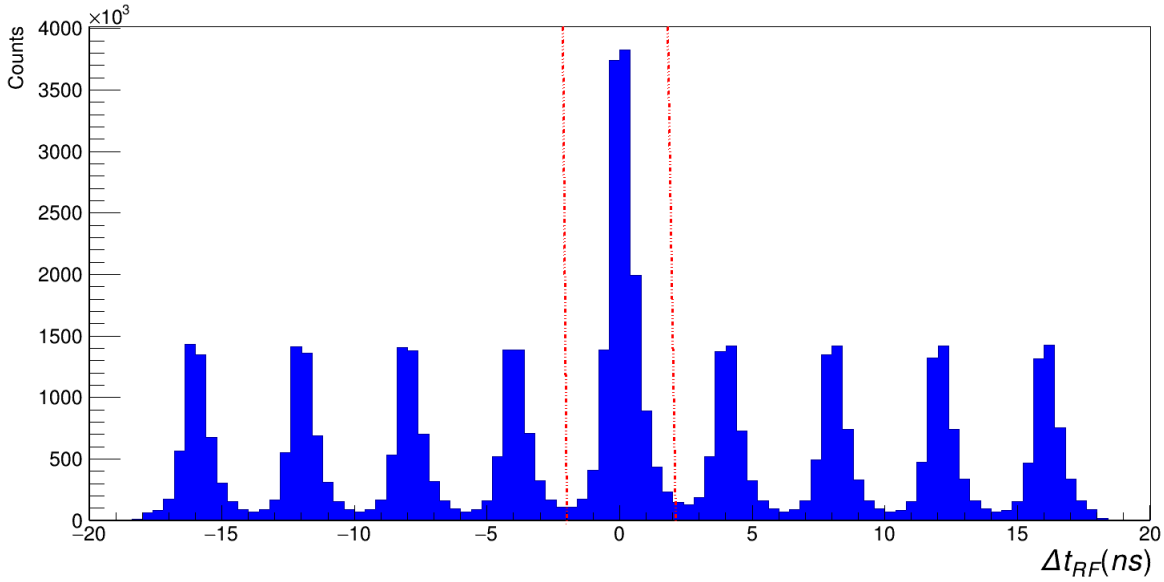

Figure 4.6: RF Δt timing distribution is shown with the "prompt peak" in between the red lines and four "out of time" beam bunches on either side. The four peaks on either sides are used for accidental subtraction.

In order to remove this contribution, a statistical subtraction method is used, since the accidental tagger photons contributed same amount to the background under the prompt peak as they did to the side bands. In this process, the reconstructed invariant mass histograms are made for both "in time" events and "out of time" events. The "out of time" histogram is scaled by 1/8 as there are 4 beam bunches on each side to make a total of 8 side bands. This scaled histogram is then subtracted from the prompt peak to obtain accidental subtracted quantity thus giving correct number of event counts from true photons.

4.4.4 Invariant mass selection cuts

The KinFit quantities were plotted to see the invariant mass distributions of particles. A 2D invariant mass squared plot of combination of decaying particles (p,π^0,η), known

as a Dalitz plot is shown in Figure 4.7. In order to cut down on the background events, as shown by the yellow vertical bands less than 2 GeV^2/c^4, a cut on the $\eta\pi^0$ mass squared between 2 GeV^2/c^4 and 6 GeV^2/c^4 was used. This cut is on the 4γ's of both η and π^0 together, i.e. $1.4142 < m_{\eta\pi^0}(4\gamma) < 2.45\ GeV/c^2$. The 1D projection of π^0p invariant mass before applying the above cuts is shown in Figure 4.11 and after applying those cuts is shown in Figure 4.12.

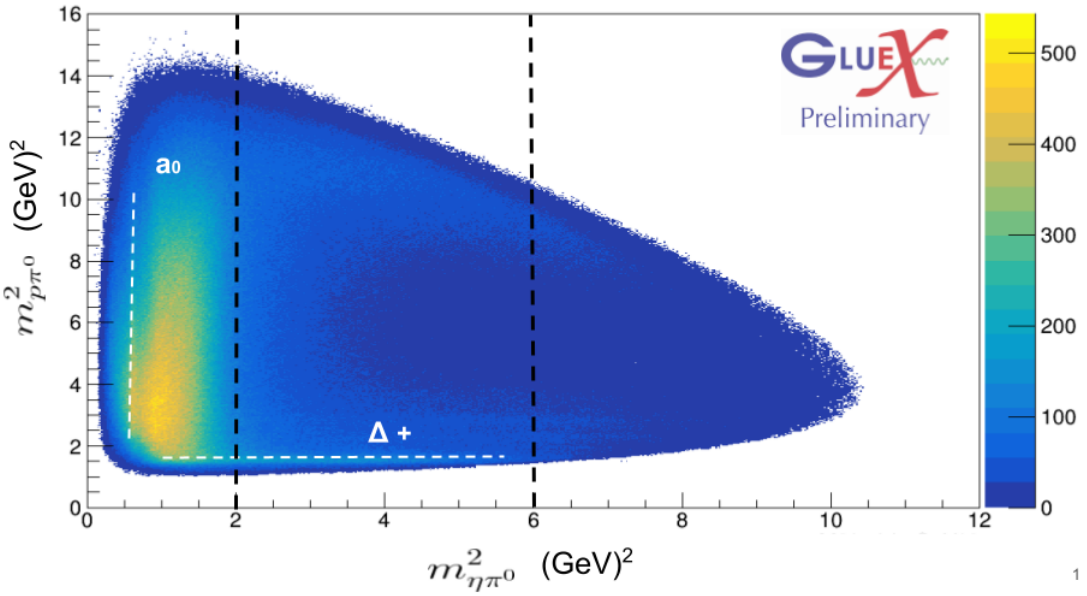

Figure 4.7: The Dalitz plot of pπ^0 on x axis and $\eta\pi^0$ on y axis. The Δ^+ and a^0 are shown by white lines. The plot is accidental subtracted. The black dashed line shows cut on the $m^2_{\eta\pi^0}$.

A tight cut on the invariant mass locus of the decaying π^0 and η is applied as shown in Figure 4.10.

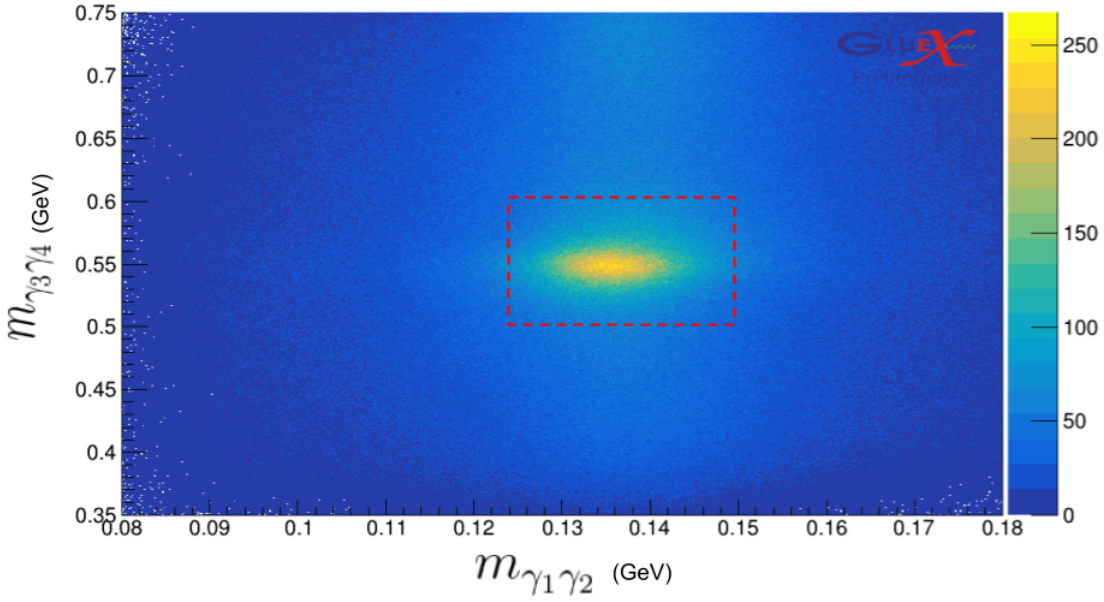

Figure 4.8: The 2D mass plot of the 2γ from π^0 on x axis and 2γ from η on the y axis is shown. The cut on η and π^0 is shown by the rectangular red dashed box. The plot is accidental subtracted.

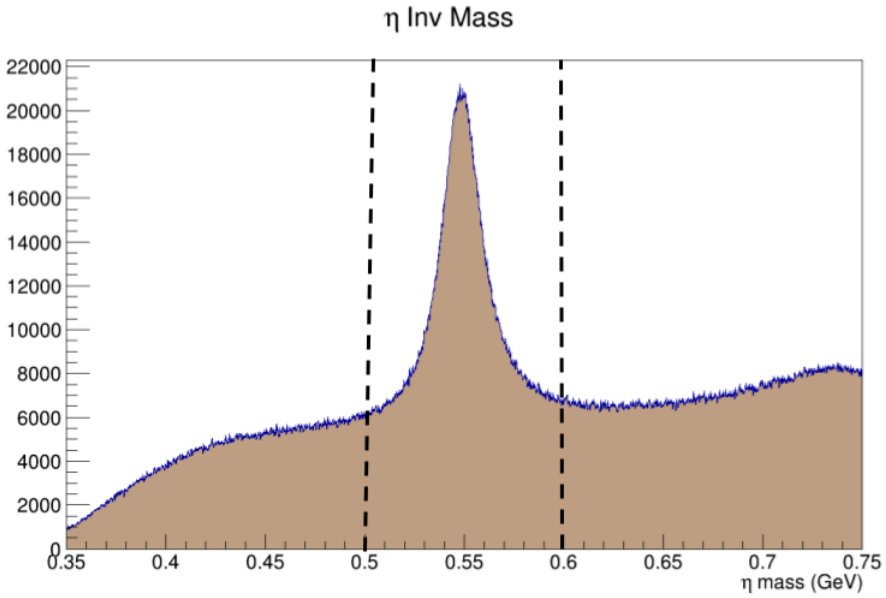

Figure 4.9: The 1D mass plot of η is shown. The cut on is shown by black dashed lines. The plot is accidental subtracted.

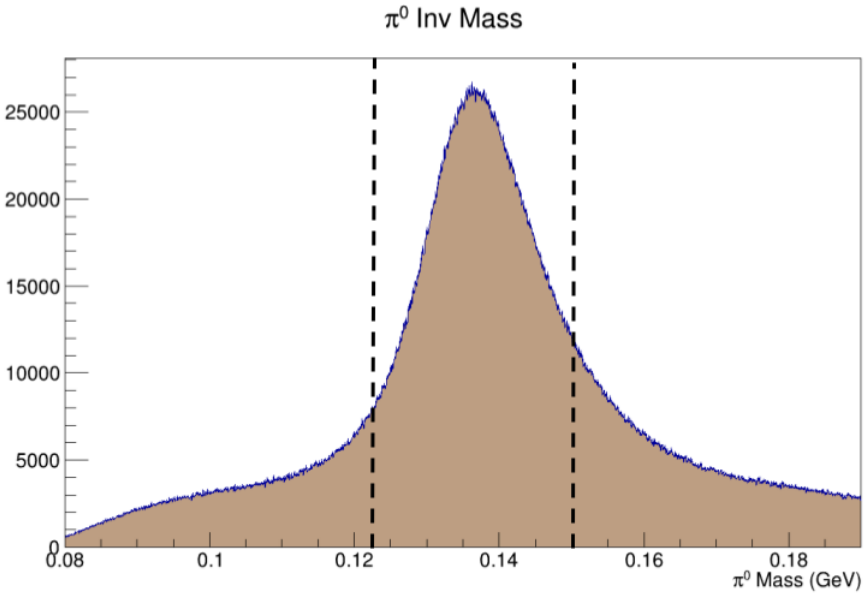

Figure 4.10: The 1D mass plot of π^0 is shown. The cut on is shown by black dashed lines. The plot is accidental subtracted.

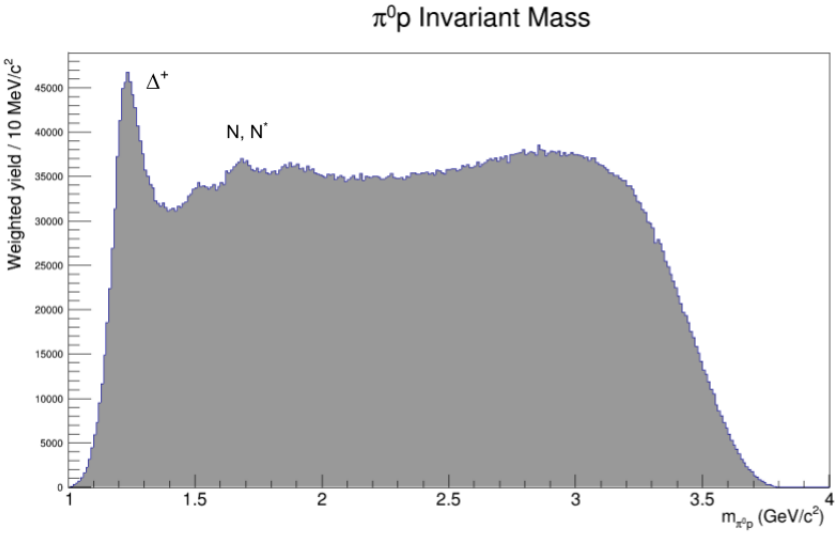

Figure 4.11: The π^0p invariant mass distribution before applying the mass selection cuts. The Δ^+ peak can be seen as well as the dominant Δ^+, N^* background. The plot is accidental subtracted.

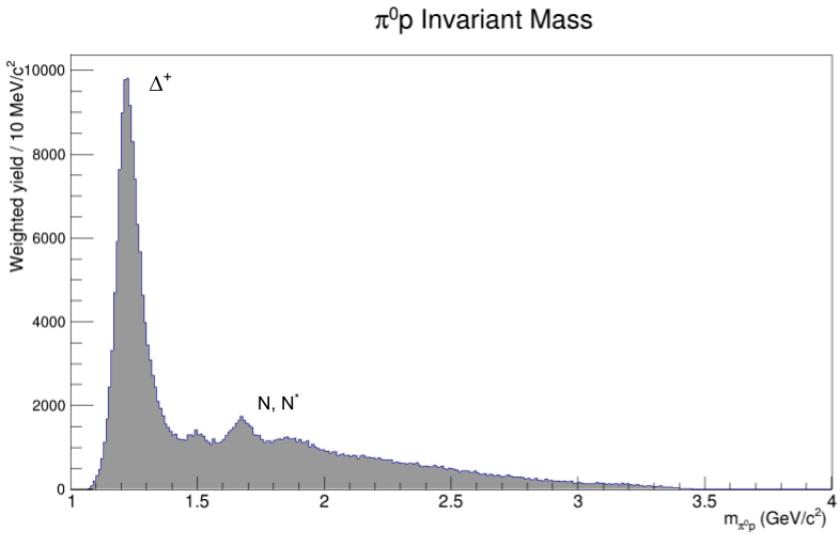

Figure 4.12: The π^0p invariant mass distribution after applying the mass selection cuts with the dominant Δ^+ peak. The plot is accidental subtracted.

In this chapter, we have discussed various steps including data collection, reconstruction and event selection through skimming. Various cuts were introduced at different stages to reduce the background contribution. This resulted in a much cleaner Δ^+ signal, as shown in in Figure 4.12, and will be used for extracting beam asymmetry.

Chapter 5

Asymmetry Method

5.1 Beam asymmetry in GlueX

The methods used to measure the beam asymmetry of photoproduced pseudoscalar mesons in GlueX are described in depth in this chapter. The Beam asymmetry is a polarization observable that may be accessed when we have polarized beams, as was mentioned in Chapter 1. The beam and target are made up of particles with unknown spin states. The expectation value of the spin projection among all the particles, also known as the system's polarization, is an information obtained from the experiment. As a result, the beam and target are statistical ensembles of single particle spin states referred as a mixed quantum state. Each mixed state has a probability of being realized, rather than being a pure quantum state. A density matrix, rather than a state vector, can be used to represent it. Hence, each spin density matrix for the beam, target, and recoiling particles has all of the spin information about them [75]. The spin density matrix elements (SDMEs) of the spin and target will be known since experiments have control over the spin states of the beam and target. The dynamics of the process, or the helicity amplitudes, will establish the SDMEs of the recoil baryon for a given initial spin configuration. The production of spin 3/2 Δ^+ in $\gamma p \to \eta\ \Delta^+$ is partially polarized in GlueX, which can be quantified in SDMEs.

The distribution of Δ^+ can be given in terms of a function $W(\theta,\ \phi,\ \Phi)$, i.e. as a function of angles, SDMEs and the direction of the beam polarization [76].

$$
\begin{aligned}
W(\theta,\phi,\Phi) = \frac{3}{4\pi}\Bigg\{ & \rho^0_{33}\sin^2\theta + \rho^0_{11}(\frac{1}{3} + cos^2\theta) - \frac{2}{\sqrt{3}}Re[\rho^0_{31}\cos\phi\sin 2\theta + \rho^0_{3-1}\cos 2\phi\sin^2\theta] \\
& - P_\gamma\cos 2\Phi\Big[\rho^1_{33}\sin^2\theta + \rho^1_{11}(\frac{1}{3} + \cos^2\theta) \\
& - \frac{2}{\sqrt{3}}Re[\rho^1_{31}\cos\phi\sin 2\theta + \rho^1_{3-1}\cos 2\phi\sin^2\theta]\Big] \\
& - P_\gamma\sin 2\Phi\frac{2}{\sqrt{3}}Im[\rho^2_{31}\sin\Phi\sin 2\theta + \rho^2_{3-1}\sin 2\Phi\sin^2\theta]\Bigg\}
\end{aligned}
\tag{5.1.1}
$$

Where;

ρ^1_{nm} (n,m are integers) are the SDMEs. Specifically ρ^1_{33}, ρ^1_{11} shown in red are the ones

that gives us the beam asymmetry

The asymmetry can be written in terms of W as

$$\Sigma = -\frac{1}{P_\gamma}\frac{W(\Phi=0) - W(\Phi=\frac{\pi}{2})}{W(\Phi=0) + W(\Phi=\frac{\pi}{2})} \tag{5.1.2}$$

When $W(\theta,\ \phi,\ \Phi)$ is integrated over the solid angle $(\theta,\ \phi)$ and assuming uniform acceptance we get, the asymmetry becomes

$$\Sigma = 2(\rho^1_{33} + \rho^1_{11}). \tag{5.1.3}$$

This matches with the beam asymmetry discussed in Chapter 1 which is given in terms of differential cross section. Indeed, the differential cross section can be expressed as follows:

$$\frac{d\sigma_{pol}}{d\phi} = \frac{\sigma_{unpol}}{2\pi}[1 - P_\gamma \Sigma \cos(2(\phi - \phi_{lin}))] \tag{5.1.4}$$

and beam asymmetry is given as

$$\Sigma = \frac{\left(\frac{d\sigma_\perp}{dt}\right) - \left(\frac{d\sigma_\parallel}{dt}\right)}{\left(\frac{d\sigma_\perp}{dt}\right) + \left(\frac{d\sigma_\parallel}{dt}\right)} \tag{5.1.5}$$

where:

- $\frac{\sigma_{unpol}}{2\pi}$ is a constant cross section term for an amorphously produced (i.e. unpolarized) beam;
- The experiment has four orientations, as discussed previously. The four orientations gives us two sets of mutually perpendicular orientations, i.e., two sets of PARA and PERP data. $\mathrm{d}\sigma_\parallel$, $\mathrm{d}\sigma_\perp$ are the differential cross sections in PARA and PERP orientations respectively.
- P_γ is the magnitude of linear polarization measured using the Triplet Polarimeter. For GlueX it is roughly around 0.35 for the coherent peak energy selection of this analysis.

- **Φ** is the difference between the angles ϕ and ϕ_{lin}
- ϕ is the azimuthal angle of the outgoing η in the lab frame (using standard detector coordinates) as shown in Figure 5.1. It is exactly opposite of the ϕ angle from the π^0 p system (Δ^+ decay) after the kinematic fit is applied.
- ϕ_{lin} is the direction of the beam polarization. For PARA(0°) ϕ_{lin}=0°, PERP(90°) ϕ_{lin}=90°, for PERP(135°) ϕ_{lin}=135°, and for PARA(45°) ϕ_{lin}=45°.

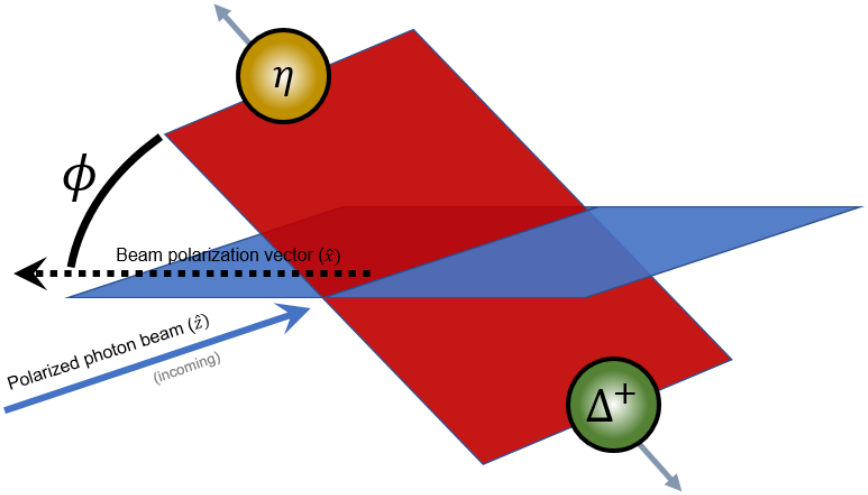

Figure 5.1: An illustration of photoproduction of η and Δ^+.

5.1.1 Σ measurement techniques

Two methods for measuring a beam asymmetry will be discussed in this chapter, the conventional direct fit method and the moment yield method. For this thesis, only the moment yield method is used but both will be presented and compared.

5.2 Conventional Direct Fit Method

The Equation 5.1.4 is expressed in terms of cross section. We can then write the asymmetry Equation using two mutually perpendicular orientations as:

$$\frac{\left(\frac{d\sigma_\perp}{d\phi}\right) - \left(\frac{d\sigma_\parallel}{d\phi}\right)}{\left(\frac{d\sigma_\perp}{d\phi}\right) + \left(\frac{d\sigma_\parallel}{d\phi}\right)} = \frac{\left(P_\perp + P_\parallel\right)\Sigma\cos(2\phi)}{2 + \left(P_\perp - P_\parallel\right)\Sigma\cos(2\phi)} \tag{5.2.1}$$

In terms of yields of events as a function of ϕ, Equation 5.1.4 can be written as:

$$\begin{aligned} Y_{\perp}(\phi, \phi_{lin} = 90) &\propto N_{\perp}[\sigma_0 A(\phi)(1 + P_{\perp}\Sigma cos2\phi)] \\ Y_{\parallel}(\phi, \phi_{lin} = 0) &\propto N_{\parallel}[\sigma_0 A(\phi)(1 - P_{\parallel}\Sigma cos2\phi)], \end{aligned} \tag{5.2.2}$$

where $Y(\phi)_{\perp}$ and $Y(\phi)_{\perp}$ denote the yield of events in PARA and PERP orientations, respectively, distributed over ϕ, with total number of events $N_{\parallel}$ and $N_{\perp}$. The experiment has four orientations, as discussed previously. The four orientations gives us two sets of mutually perpendicular orientations, i.e., two sets of PARA and PERP data. The $N_{\parallel}$ and $N_{\perp}$ are determined from the Pair Spectrometer flux. $P_{\parallel}$ and $P_{\perp}$ are polarizations for PARA and PERP orientation data and are externally determined using the Triplet Polarimeter. This provides terms proportional to $\frac{d\sigma_{\parallel}}{d\phi}$ and $\frac{d\sigma_{\perp}}{d\phi}$. We can then express Equation 5.2.2 as

$$\frac{Y(\phi)_{\perp} - F_R Y(\phi)_{\parallel}}{Y(\phi)_{\perp} + F_R Y(\phi)_{\parallel}} = \frac{\left(P_{\perp} + P_{\parallel}\right)\Sigma\cos(2\phi)}{2 + \left(P_{\perp} - P_{\parallel}\right)\Sigma\cos(2\phi)}, \tag{5.2.3}$$

where F_R is the flux ratio defined as $F_R \equiv \frac{N_{\perp}}{N_{\parallel}}$. The terms on the left hand side containing yields that can be determined experimentally. The right hand side provides the functional form which consists of the known polarization values $P_{\parallel}$ and $P_{\perp}$. This leaves with the free parameter Σ in the right hand side. The function can be directly fit to determine Σ.

The previous published works of GlueX on η beam asymmetries used this method [30] [31]. The ηp channel contained a known and smoothly varying background contribution from the ω meson decay. This was removed using a sideband subtraction (the method is exactly similar to accidental subtraction discussed before). Thus, this method can only be used after the removal of any known background. In the case of $\eta\Delta^+$ the background for $m_{\pi^0 p}$ invariant mass distribution is not smooth and slowly varying. Instead, a different method is needed which could extract the Σ while separating background contributions without relying on sideband methods.

5.3 Moment yield method

As shown in Figure 4.12, a relatively pure sample of Δ^+ cannot be obtained by selecting a region of $m_{\pi^0 p}$ invariant mass. The Direct-Fit Method aims to extract the amplitude of the 2Φ oscillation of a data sample consistent with pure signal. For the present analysis, the Moment Yield method is used, where the 2Φ component of all the data for a given energy is projected on the invariant mass histogram. The Δ^+ contribution is then isolated by using the known lineshape of the Δ^+. Here, individual events are weighted individual by $cosn\Phi$ and $m_{\pi^0 p}$ invariant mass histograms are created. The bin-by-bin contents of such histograms are then proportional to strength of the $cosn\Phi$ component. These histograms can be fit to measure the Δ^+ contribution to each. This technique, referred to as the "Moment-Yield Method", will be discussed in the rest of this chapter.

This method was first implemented in CLAS analysis of $\gamma p \to \pi^0 p$ and $\gamma p \to \pi^+ n$ [77] and was later used in $\pi^- \Delta^{++}$ analysis in GlueX [32]. For this work, the same technique is followed and similar notations are used.

Before the detailed description of the method, some quantities are introduced below:

- Y_a,is the unnormalized yield of signal events recorded in the GlueX detector, using an amorphous radiator i.e. no beam polarization.
- $Y_{\parallel(\perp)}$, is the unnormalized yield of signal events recorded in the GlueX detector with a diamond radiator in PARA (PERP) orientations.
- N_γ, is the number of incident beam photons for a specific dataset calculated using the Pair Spectrometer. When more data is collected in one orientation than the other, or when detector acceptance results in a systematic bias toward the detection of events in one orientation over another, this is a crucial quantity.
- $\tilde{Y} = \frac{Y}{N_\gamma}$, is the yield (amorphous, $\parallel$, or $\perp$ data) normalized by the number of beam photons.

Next, the amorphous yield-density is defined, giving the distribution of yields as a function of ϕ by:

$$\tilde{Y}_a = \int_{-\pi}^{\pi} f_a(\phi) d\phi \tag{5.3.1}$$

It is important to note that this equation is completely general. Any detector acceptance effects are encoded in $f_a(\phi)$. Furthermore, for this analysis, we do not need to explicitly know what $f_a(\phi)$ is with the GlueX detector. The amorphous yield density $f_a(\phi)$ is expressed as a Fourier series:

$$f_a(\phi) = a_0 + \sum_{m=1}^{\infty} [a_n \cos(m\phi) + b_n \sin(m\phi)] \tag{5.3.2}$$

The technique used in this method is similar to that used to determine coefficients of a Fourier expansion. During the derivation in the following subsections it will be shown that only the coefficients a_0, a_2, and a_4 are only required to extract the asymmetry parameter Σ. Here, the derivation is done for the PARA(0°)/PERP(90°) data by using $\cos(n\phi)$, while $\sin(n\phi)$ is used in the case of PARA(45°)/PERP(135°). The polarized yields $Y_\parallel$ and $Y_\perp$ can be expressed using Equation 5.1.4 as:

$$\tilde{Y}^\perp = \int_{-\pi}^{\pi} f_\perp(\phi) d\phi = \int_{-\pi}^{\pi} f_a(\phi)(1 + P\Sigma \cos(2\phi)) d\phi \tag{5.3.3}$$

$$\tilde{Y}^\parallel = \int_{-\pi}^{\pi} f_\parallel(\phi) d\phi = \int_{-\pi}^{\pi} f_a(\phi)(1 - P\Sigma \cos(2\phi)) d\phi \tag{5.3.4}$$

and substituting Fourier expansion terms for $f_a(\phi)$, we get:

$$\begin{aligned} f_\perp(\phi) &= f_a(\phi)(1 + P\Sigma \cos(2\phi)) \\ &= \left[a_0 + \sum_{m=1}^{\infty} (a_n \cos(m\phi) + b_n \sin(m\phi)) \right] (1 + P\Sigma \cos(2\phi)) \end{aligned} \tag{5.3.5}$$

$$
\begin{aligned}
f_{\parallel}(\phi) &= f_a(\phi)(1 - P\Sigma\cos(2\phi)) \\
&= \left[a_0 + \sum_{m=1}^{\infty}(a_n\cos(m\phi) + b_n\sin(m\phi))\right](1 - P\Sigma\cos(2\phi))
\end{aligned}
\tag{5.3.6}
$$

Using the definitions above, a set of m^{th} *moment yields* Y_m can be defined as:

$$
\tilde{Y}_m^{\perp} = \int_{-\pi}^{\pi}\cos(m\phi)f_{\perp}(\phi)d\phi = \int_{-\pi}^{\pi}\cos(m\phi)f_a(\phi)(1 + P\Sigma\cos(2\phi))d\phi \tag{5.3.7}
$$

$$
\tilde{Y}_m^{\parallel} = \int_{-\pi}^{\pi}\cos(m\phi)f_{\parallel}(\phi)d\phi = \int_{-\pi}^{\pi}\cos(m\phi)f_a(\phi)(1 - P\Sigma\cos(2\phi))d\phi \tag{5.3.8}
$$

The following linear combinations of moment yields can be solved by using the form for f_a in Equation 5.3.2, orthogonality relationships, and moment yield Equations 5.3.7 and 5.3.8.

$$
\tilde{Y}_2^{\perp} - \tilde{Y}_2^{\parallel} = \pi(P_{\perp} + P_{\parallel})\Sigma\left(a_0 + \frac{a_4}{2}\right) \tag{5.3.9}
$$

$$
\tilde{Y}_0^{\perp} + \frac{P_{\perp}}{P_{\parallel}}\tilde{Y}_2^{\parallel} = 2\pi a_0\left(1 + \frac{P_{\perp}}{P_{\parallel}}\right) \tag{5.3.10}
$$

$$
\tilde{Y}_4^{\perp} + \frac{P_{\perp}}{P_{\parallel}}\tilde{Y}_4^{\parallel} = \pi a_4\left(1 + \frac{P_{\perp}}{P_{\parallel}}\right) \tag{5.3.11}
$$

Then, Equation 5.3.10 can be solved for a_0 and Equation 5.3.11 for a_4. Inserting these into Equation 5.3.9 to eliminate a_0 and a_4, we obtain the expression for the asymmetry Σ:

$$
\Sigma = \frac{\tilde{Y}_2^{\perp} - \tilde{Y}_2^{\parallel}}{\frac{P_{\parallel}}{2}(\tilde{Y}_0^{\perp} + \tilde{Y}_4^{\perp}) + \frac{P_{\perp}}{2}(\tilde{Y}_0^{\parallel} + \tilde{Y}_4^{\parallel})} \tag{5.3.12}
$$

It is useful to express the moment-yield expression for Σ as:

$$
\Sigma = \frac{N}{D} \tag{5.3.13}
$$

where

$$
\begin{aligned}
N &= \tilde{Y}_2^{\perp} - \tilde{Y}_2^{\parallel} \\
D &= \frac{P_{\parallel}}{2}(\tilde{Y}_0^{\perp} + \tilde{Y}_4^{\perp}) + \frac{P_{\perp}}{2}(\tilde{Y}_0^{\parallel} + \tilde{Y}_4^{\parallel})
\end{aligned}
\tag{5.3.14}
$$

So far, continuous integrals of ϕ are used for deriving the above expressions for moment-yields $Y_m^{\perp}$ and $Y_m^{\parallel}$. But the data used for the analysis is in terms of finite bins of invariant mass. In the next section, we will express the moment yields and Σ in terms of finite samples of events.

5.3.1 Implementation in Data

The total yield $\tilde{Y}^{(\perp/\parallel)}$ can be expressed in terms of small bins of mass denoted as $\Delta\tilde{Y}_j^{(\perp/\parallel)}$ by the following expression:

$$
\tilde{Y}^{(\perp/\parallel)} = \sum_{k=1}^{k_{max}} \Delta\tilde{Y}_j^{(\perp/\parallel)} \tag{5.3.15}
$$

where k specifies a particular mass bin. The invariant mass distribution in this analysis is from 0 GeV to 4 GeV with 300 bins. Thus, 13 MeV wide bins of $m_{\pi^0 p}$ are used for this analysis.

Each individual $\Delta\tilde{Y}_j^{(\perp/\parallel)}$ can be thought of as a Monte Carlo estimator of the integral over ϕ of the yield density in a particular mass bin (denoted as $\Delta f_{\perp/\parallel}$). This can be expressed as in the following two equations:

$$
\Delta\tilde{Y}_{m,j}^{\perp} = \int_{-\pi}^{\pi} \cos(m\phi)\Delta f_{\perp}(\phi)d\phi \approx 2\pi \sum_{i=1}^{N_j} \cos(m\phi_i) \tag{5.3.16}
$$

$$
\Delta\tilde{Y}_{m,j}^{\parallel} = \int_{-\pi}^{\pi} \cos(m\phi)\Delta f_{\parallel}(\phi)d\phi \approx 2\pi \sum_{i=1}^{N_j} \cos(m\phi_i) \tag{5.3.17}
$$

The domain volume factor of 2π appears for all quantities and can be safely dropped (or formally by redefining terms to absorb this factor, if one prefers).

Statistical uncertainties

For a set of Poisson-distributed events N_j within each mass bin, the statistical variance can then be expressed as:

$$\sigma^2_{\Delta\tilde{Y}_{m,j}} = \frac{1}{N_\gamma^2}\sum_{i=1}^{N_j}\cos^2(m\phi_i) \tag{5.3.18}$$

It can be shown that

$$\sigma^2_{\Delta\tilde{Y}_{0,j}} = \frac{1}{N_\gamma^2}\sum_{i=1}^{N_j}1 = \frac{1}{N_\gamma^2}\Delta Y_{0,j} = \frac{1}{N_\gamma}\Delta\tilde{Y}_{0,j} \tag{5.3.19}$$

Then, using the double-angle identity we can also show that

$$\sigma^2_{\Delta\tilde{Y}_{m,j}} = \frac{1}{2N_\gamma^2}\sum_{i=1}^{N_j}[1+\cos(2m\phi_i)] = \frac{1}{2N_\gamma^2}[\Delta\tilde{Y}_{0,j}+\Delta\tilde{Y}_{2m,j}] \tag{5.3.20}$$

The covariance of two moment-yield quantities is defined as

$$Cov(\Delta\tilde{Y}_{m_1,j},\Delta\tilde{Y}_{m_2,j}) = \frac{1}{N_\gamma^2}\sum_{i=1}^{N_j}\cos(m_1\phi_i)\cos(m_2\phi_i) \tag{5.3.21}$$

and it can be shown that

$$Cov(\Delta\tilde{Y}_{0,j},\Delta\tilde{Y}_{m,j}) = \frac{1}{N_\gamma^2}\Delta\tilde{Y}_{m,j} \tag{5.3.22}$$

and

$$Cov(\Delta\tilde{Y}_{m,j},\Delta\tilde{Y}_{1m,j}) = \frac{1}{2N_\gamma^2}\left(\Delta\tilde{Y}_{m,j}+\Delta\tilde{Y}_{3m,j}\right). \tag{5.3.23}$$

Using these relationships, the statistical uncertainty on Σ can be derived. Since the histograms are weighted by $cos(m\phi)$, the errors received from the ROOT fitting cannot be depended upon. Errors in the case of log-likelihood can be used only when the weights are equal to one, which is not the case here. Thus we need to have different expression to extract the statistical uncertainty.

The variance of Σ in terms of N and D from Equation 5.3.13 can be expressed as

$$\sigma_{\Sigma}^{2} = \Sigma \left\{ \frac{\sigma_{N}^{2}}{N^{2}} + \frac{\sigma_{D}^{2}}{D^{2}} - 2\frac{Cov(N,D)}{ND} \right\} \tag{5.3.24}$$

The validation of the uncertainty expressions is checked using toy MC data, and will be shown later in this chapter. Thus, three additional terms which include numerator variance σ_N^2, denominator variance σ_D^2 and covariance of numerator and denominator $Cov(N,D)$ are needed. These variance terms can be expressed as linear combinations of moment-yields $\tilde{Y}_m$:

$$\sigma_{N}^{2} = \frac{1}{2N_{\gamma\perp}} \left(\tilde{Y}_{0}^{\perp} + \tilde{Y}_{4}^{\perp} \right) + \frac{1}{2N_{\gamma\parallel}} \left(\tilde{Y}_{0}^{\parallel} + \tilde{Y}_{4}^{\parallel} \right) \tag{5.3.25}$$

$$\sigma_{D} = \frac{P_{\parallel}^{2}}{4N_{\gamma\perp}} \left(\tilde{Y}_{0}^{\perp} + \frac{1}{2} \left(\tilde{Y}_{0}^{\perp} + \tilde{Y}_{8}^{\perp} \right) + 2\tilde{Y}_{4}^{\perp} \right) + \frac{P_{\perp}^{2}}{4N_{\gamma\parallel}} \left(\tilde{Y}_{0}^{\parallel} + \frac{1}{2} \left(\tilde{Y}_{0}^{\parallel} + \tilde{Y}_{8}^{\parallel} \right) + 2\tilde{Y}_{4}^{\parallel} \right) \tag{5.3.26}$$

$$Cov(N,D) = \frac{P_{\parallel}}{4N_{\gamma\parallel}} \left(3\tilde{Y}_{0}^{\perp} + \tilde{Y}_{6}^{\perp} \right) + \frac{P_{\parallel}}{4N_{\gamma\perp}} \left(3\tilde{Y}_{0}^{\perp} + \tilde{Y}_{6}^{\perp} \right) \tag{5.3.27}$$

All quantities that are required to measure Σ are listed above. The $\cos(2\phi)$ dependence of the data is present in the yields of $\tilde{Y}_2^{(\parallel/\perp)}$. Thus, the magnitude and sign of polarization times asymmetry Σ is extracted using the yields of the same components. The proper normalization is achieved using the quantities $\tilde{Y}_0^{(\parallel/\perp)}$ which are scaled by polarization.

The moment-yields $\tilde{Y}_4^{(\parallel/\perp)}$, $\tilde{Y}_6^{(\parallel/\perp)}$, and $\tilde{Y}_8^{(\parallel/\perp)}$ completely express the non-uniform ϕ dependence of an experiment. Although the GlueX experiment is considered to have uniform ϕ acceptance, we have included them to help in accounting for the correction factors and fully eliminate the effect of any detector acceptance.

5.3.2 Extraction of Σ in the Presence of Background

As discussed earlier, the Direct-Fit Method can not be used for this channel as we do not have pure signal (without any background) for the $\eta\Delta^+$ data. In this case, one must account for the presence of background. This can be done by obtaining the moment yield $\tilde{Y}_m^{\perp/\parallel}$ components through a fitting procedure. Assume that two processes, with two different corresponding asymmetries Σ_{sig} and Σ_{bg}, contribute to a particular mass distribution. We label these *sig* for signal and *bg* for background. Unfortunately, the information on how much each of these contribute to each bin of the distribution is not available. Then the signal and background asymmetries can be extracted separately using a moment yield method through a fitting procedure provided that they both have different characteristics mass distributions. The physics process that determines the distribution of events over a mass range happens after the production. Since the measurement of ϕ happens at the production, we can safely make the assumption that the Σ for signal carries no mass dependence.
Let us define each mass bin by $\Delta h_{m,k}^{\perp/\parallel}$. Each mass bin then contains two components:

$$\Delta h_{m,k}^{\perp/\parallel} = \Delta \tilde{Y_{sig}}_{m,k}^{\perp/\parallel} + \Delta \tilde{Y_{bg}}_{m,k}^{\perp/\parallel} \tag{5.3.28}$$

in data, these are once again calculated (following Equation 5.3.16 and 5.3.17) as:

$$\Delta h_{m,k}^{\perp/\parallel} \approx \sum_{i=1}^{N_k} \cos(m\phi_i) \tag{5.3.29}$$

Let $g_{sig}(m;\lambda_{sig})$ and $g_{bg}(m;\lambda_{bg})$ be probability distribution functions (pdfs) describing the shapes of signal and background respectively, over mass parameter m with shape parameters λ. These functions are defined and normalized over a mass range m_1 to m_2. An invariant mass distribution over m can be fit to the function

$$f_{fit}(m) = \tilde{Y_{sig}}_m \, g_{sig}(m;\lambda_{sig}) + \tilde{Y_{bg}}_m \, g_{bg}(m;\lambda_{bg}) \tag{5.3.30}$$

with normalization convention

$$\begin{aligned} \int_{m_1}^{m_2} g_{sig}(m;\lambda_{sig})\, dm = 1 \\ \int_{m_1}^{m_2} g_{bg}(m;\lambda_{bg})\, dm = 1 \end{aligned} \tag{5.3.31}$$

Let $h_m^{\perp/\parallel}$ represent the histogram over a range of mass, with individual bin contents $\Delta h_{m,k}^{\perp/\parallel}$. We can then fit the histogram $h_m^{\perp/\parallel}$ to the function in Equation **??** to determine constants $\tilde{Y}_{sigm}$ and $\tilde{Y}_{bgm}$. These fit parameters $\tilde{Y}_{sigm}$ and $\tilde{Y}_{bgm}$ are then the inputs to Equation 5.3.13 to determine Σ and Equations 7.1.5-7.1.7 to determine its statistical uncertainty.

5.3.3 Modification to CLAS Method Parameters

The analysis in CLAS was done using high statistics. On the other hand, for some of the $\pi^-\Delta^{++}$ analysis the statistics were low. Likelihood fitting performs well in case of lower statistics compared to the conventional χ^2 fitting. A similar approach of using likelihood fitting has been taken here as the present analysis also faces low statistics.

Following the footsteps of the $\pi^-\Delta^{++}$ analysis, we modify the method used in this thesis to solve for $\Sigma' \equiv \Sigma + 1$. This Σ' then ranges from 0 to 2 and should have positive amplitudes everywhere. In terms of the original CLAS method, we re-parameterize to solve for:

$$\Sigma' = \frac{N'}{D} \equiv \frac{N+D}{D}. \tag{5.3.32}$$

Here, N and D are the original numerator and denominator as they appear in Equation 5.3.13, whereas N' refers to a new numerator defined above. The uncertainty on this parameter takes the form

$$\sigma_{\Sigma'}^2 = \Sigma' \left\{ \frac{\sigma_{N'}^2}{N'^2} + \frac{\sigma_D^2}{D^2} - 2\frac{Cov(N',D)}{N'D} \right\}. \tag{5.3.33}$$

It is straightforward to show that the modified variance components of Σ' can be

expressed in terms of quantities above as:

$$\begin{aligned} \sigma^2_{N'} &= \sigma^2_N + \sigma^2_D + 2Cov(N, D) \\ Cov(N', D) &= Cov(N, D) + \sigma^2_D. \end{aligned} \tag{5.3.34}$$

This gives all the quantities required to solve for any value of asymmetry Σ using log-likelihood fitting. The yields from the above quantities are only used for determining the Σ and its statistical uncertainty as we cannot rely upon the errors from ROOT fitting (likelihood fitting errors are only valid when weights are equal to 1). We will describe in detail about the signal and background functions in the next section.

5.3.4 Signal and background Fit functions

For the signal Δ^{++} lineshape a relativistic Breit-Wigner with P-wave dynamic mass width is used. The Breit-Wigner propagator is given by:

$$BW = \frac{h(p)}{m^2_{BW} - s - im_{BW}\Gamma(s)}. \tag{5.3.35}$$

The term $h(p)$ includes threshold factors and Blatt-Weisskopf barrier factors [78]. For an angular momentum 1 decay (P-wave) it is given by

$$h^2(p) = \frac{p^2 r^2}{1 + p^2 r^2}. \tag{5.3.36}$$

The term $\Gamma(s)$ is the dynamical mass width

$$\Gamma(s) = \Gamma_0 \frac{p m_{BW}}{p_0 \sqrt{s}} \frac{h^2(p)}{h^2(p_0)} \tag{5.3.37}$$

where p is the pion momentum in the c.m. frame, s is the invariant mass of the π^0 proton system, m_{BW} is the BW mass parameter, Γ_0 is the BW width parameter, p_0 is the pion momentum at m_{BW}, and r is the interaction radius. The values m_{BW}=1.232 GeV/c^2 and Γ_0=0.117 GeV/c^2 are obtained from the PDG [78]. The value of the interaction radius is taken from the previously measured hadroproduction value r =

1.15 ± 0.02 fm [79].

The final fit function is obtained as

$$\frac{d^2\sigma}{dtdm_{\pi^+p}} \equiv f_\Delta = N\frac{\lambda^{1/2}(s, m_\pi^2, m_p^2)}{s}BW(s)^2 \tag{5.3.38}$$

where N is a normalization constant and λ is the Kaellen function:

$$\lambda(x, y, z) = x^2 + y^2 + z^2 - 2xy - 2xz - 2yz. \tag{5.3.39}$$

The histograms ($H_{N'}$, H_D, $H_{\sigma^2_{N'}}$, $H_{\sigma^2_D}$, and $Cov(N', D)$) are fitted to the function as given below:

$$f_{tot} = Nf_\Delta(m_{\pi p}) + p_1 b_{1,n}(m_{\pi p}) + p_2 b_{2,n}(m_{\pi p}) + ... + p_n b_{n,n}(m_{\pi p}) \tag{5.3.40}$$

where $b_{\nu,n}(m_{\pi p})$ is the set of Bernstein polynomials of degree n. The Bernstein polynomial has the benefit that each component, $b_{\nu,n}$, is by design positive. Therefore, the total background function is guaranteed to deliver a positive yield as long as each fit coefficient p_1,..., p_n is required to be positive on an individual basis. These are defined from $m_{Min} < m_{\pi^+p} < M$, with m_{Min} the fixed π proton threshold, and M, a free parameter that roughly corresponds to the right edge of these histograms (typically about 3.0-3.5 GeV/c^2). Coefficients p_1,...,p_n are fitted to data and restricted to be positive. Fourth order Bernstein polynomials are used as nominal value for this analysis.

The line shape parameters as described above are taken as nominal values. The changes to these values are separately studied as possible systematic uncertainties which will be discussed in detail in the next chapter.

5.4 Final $\eta\Delta$ Asymmetry Extraction Workflow

Together with the fit functions as mentioned in the preceding section, the five histograms ($h_{N'}$, h_D, $h_{\sigma^2_{N'}}$, $h_{\sigma^2_D}$, and $Cov(N', D)$), will help in extracting the beam asym-

metry. A brief overview of asymmetry extraction workflow is given in this section. As discussed in the previous chapter, there are certain event selection criteria which the accepted events have to pass through. The distribution of those events forms the invariant mass histogram $h_m^{(\parallel/\perp)}$. Each signal moment $\tilde{Y}_m^{(\parallel/\perp)}$ is assigned to have an $h_m^{(\parallel/\perp)}$. In order to perform the accidental subtraction there are separate $h_m^{(\parallel/\perp)}$ for both in-time events and out-of-time events. These are filled with weight $\cos(m\phi)$ for $0/90^\circ$ data and with weight $\sin(m\phi)$ for $45/135^\circ$ data.

We can try understanding this using an example. We $h_{4\ in-time}^{\perp}$ and $h_{4\ out-of-time}^{\perp}$ which corresponds to 4^{th} moment histogram. Let's say we have an in time event which can be found from RF Δt value, a π^0 proton invariant mass, and an observed η angle. The ROOT frame work allows us to fill the histograms using Fill function has additional option of weighing the data.

```
Histogram->Fill(data event, weight);
```

In this case, the pseudo code will look like

```
Hist_4mom_perp_InTime->Fill( π⁰ proton mass,TMath::Cos(4*φ));
```

Since there are 0^{th}, 2^{nd}, 4^{th}, 6^{th}, and 8^{th} moment histograms, this process is repeated for all those histograms. These histograms are then accidental subtracted, as discussed in the previous chapter.

With accidental subtracted moment histograms $h_m^{(\parallel/\perp)}$, we define the following histograms (mirroring the definitions in previous sections)

$$h_D = \frac{P_\parallel}{2}(h_0^\perp + h_4^\perp) + \frac{P_\perp}{2}(F_R h_0^\parallel + F_R h_4^\parallel), \tag{5.4.1}$$

$$h_{N'} = h_2^\perp + F_R h_2^\parallel + h_D. \tag{5.4.2}$$

The flux ratio F_R is used to normalize histograms to one another. This accounts

for the absolute quantities of N_γ. Each variance term $h_{\sigma^2_{N'}}$, $h_{\sigma^2_D}$, and $Cov(N', D)$ is represented by particular histograms as defined earlier. Thus we have five histograms to fit for each $0/90^\circ$ or $45/135^\circ$ dataset: $h_{N'}$, h_D, $h_{\sigma^2_{N'}}$, $h_{\sigma^2_D}$, and $Cov(N', D)$. These histograms are fitted to a relativistic Breit-Wigner and polynomial background in order to extract the Δ^+ yield in each histogram.

Chapter 6

Monte Carlo Simulation Studies

6.1 Introduction

In this chapter, we will first go through the MC generation framework used in GlueX. Simulated events using this framework are used for efficiency studies. By comparing the events from experimental data and the simulated events we get a quantitative information on how efficient the reconstruction and analysis processes were. Later on, we will discuss the validation of the statistical uncertainty using a toy MC.

6.2 Monte Carlo Generation

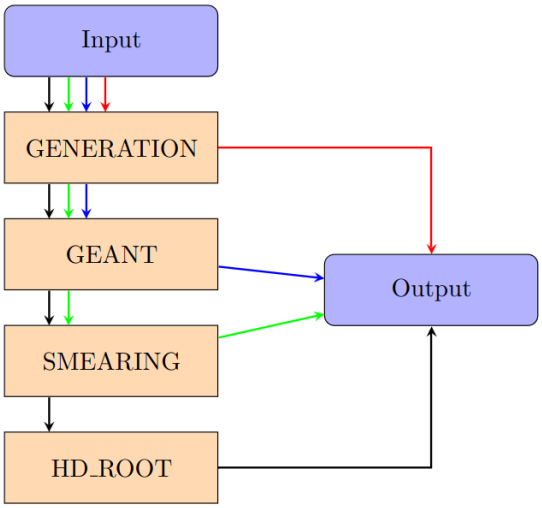

Figure 6.1: A flowchart of MC generation at GlueX. Ref [80]

The MC generation framework, as shown in Figure 6.1, is really helpful as it is customizable for individual analyses. It is written in python and shell scripting.

Generation

In the first step, the reaction of interest is defined, which serves as the input for the generation part. This includes defining the initial and final state particles. These particles are characterized by their energy-momentum four vectors, which are generated using a generator. For this work genr8 is used, which is one of the default generators

for MC simulation in GlueX collaboration. It is based on the isobar model, which constructs any many-body system as a tree of subsequent two-body decays [81]. Both mesons and baryon decay chains are allowed, but with the limiting assumption of a t-channel production process. It is useful for calculating acceptance and resolution for signal events. In this step, a beam photon energy is generated, and the energy-momentum of all final state particles except one, whose four-vector is calculated according to the energy-momentum conservation. Following the creation of the event's set of four vectors, a weight is determined using a PDF. Depending on the user's need, this PDF could be uniform to simulate particles scattering with no resonance (i.e. phasespace) or it could describe the features of a resonance (i.e. signal): the decaying delta baryon in our case [81]. If the weight exceeds a threshold set by a uniform random function, the event is recorded. As the MC simulation is mimicking the data, it is important to have exactly similar run conditions. For this it utilizes information from Run Conditions Data Base (RCDB). This includes appropriate run number also various parameters such as radiator thickness, coherent Peak Position, electron beam energy etc.

Geant

Geant4 is a toolkit for the realistic, 3D simulation of the passage of particles through matter. It was created for subatomic physics experiments and in recent decades have found applications in accelerator and medical physics. After the generation step, the MC sample is passed through a Geant simulation (supports both Geant3 and Geant4) of the full GlueX spectrometer. It uses the RCDB information to determine specifics of the detector and records the final state particles as hits in the various detector subsystems.

Smearing

These hits from Geant are then smeared to simulate readout resolution and thus makes the MC more similar to data. The smearing parameters are obtained from

energy and position resolution values of various detectors in GlueX. For example the energy resolution of BCAL is given by Equation 2.3.1.

HDRoot

The HD Root process in the simulation production line runs a specified plugin according to the particular analysis over the smeared file from the previous step. An output can be received after any point in the chain of the framework and can skip any process if needed, thus making it more flexible to use. At this stage, the MC sample is converted into the same format as that of experimental data.

6.3 Efficiency Studies

The MC sample is then used for efficiency studies by comparing with the experimental data which will be explained in this section. First, frames of references will be discussed as they are important for the study of the decaying particles and their distributions in the detector. Then the SDME's, which can be expressed in terms of angles and their relation with beam asymmetry Σ. Finally we will discuss how an efficiency correction can address a potential bias in the measurement of Σ.

6.3.1 Frames of reference

Lab frame and Center of Mass Frame

The laboratory frame, or Lab Frame for short, is generally used in GlueX. The proton in the GlueX liquid hydrogen target which is at rest interacts with an incident photon of energy traveling in the $\boldsymbol{z}$ direction. The $\boldsymbol{x}$ direction is taken in this frame such that we have a right-handed coordinate system, and the $\boldsymbol{y}$ direction is considered as up [82]:

$$\hat{x} = \hat{y} \times \hat{z} \tag{6.3.1}$$

$\boldsymbol{x}$, if looking in the $\boldsymbol{z}$ direction, is to the left, as shown in Figure 6.2.

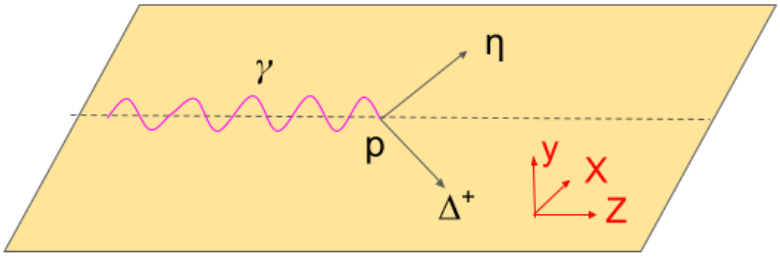

Figure 6.2: The depiction of lab frame coordinates used in GlueX. A right-handed coordinate system is formed by the z-axis being along the incident photon beam's direction, the y-axis pointing up and normal to the hall floor, and the x-axis pointing left of the beam.

The center of mass frame is defined using the same axis orientations as the lab frame, but as Figure 6.3 illustrates, the system's total momentum is zero. With respect to the lab frame, the center of mass frame travels at a velocity along the positive axis. A Lorentz boost is applied along the $\boldsymbol{z}$ axis to obtain the four vectors in the center of mass frame. In special relativity, Lorentz transformation is a linear transformation to shift from one co-ordinate system to another. The transformation's parameter is the relative velocity between the frames.

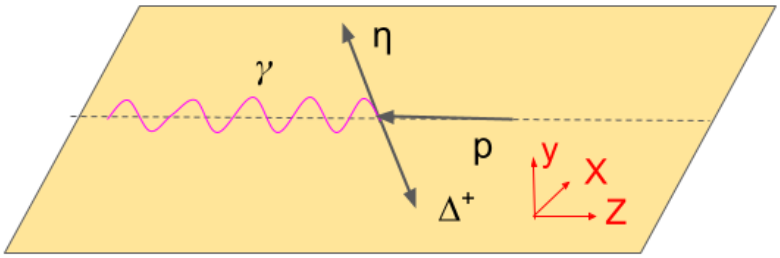

Figure 6.3: The depiction of center of mass frame used in GlueX. A right-handed coordinate system is formed by the z-axis being along the incident photon beam's direction, the y-axis pointing up and normal to the hall floor, and the x-axis pointing left of the beam.

The Gottfried-Jackson frame

In reactions such as the one shown in Figure 6.3, the produced meson or baryon (the Δ^+ in this thesis) typically decays into two daughter particles; there are other decay channels that can involve three daughters. As mentioned in the previous chapter, the angular distribution of outgoing π^0 and proton in the rest frame of the Δ^+ is given by the SDMEs. The two most commonly used reference frames for such meson or baryon analyses are the Gottfried-Jackson (GJ) frame and the helicity (H) frame [82]. Both are measured in the rest frame of the Δ^+, where we move to the Δ^+ rest frame with a Lorentz boost from the center-of- mass frame. The frames both have the same y axis, but their z axes differ. The y axis can be expressed in terms of center of mass momenta $\overrightarrow{P_\gamma}$ and $\overrightarrow{P}_{\Delta^+}$, in the following manner:

$$\hat{y}_{GJ} = \frac{\overrightarrow{P_\gamma} \times \overrightarrow{P}_{\Delta^+}}{|\overrightarrow{P_\gamma} \times \overrightarrow{P}_{\Delta^+}|} \tag{6.3.2}$$

For the GJ frame, the z-axis is the direction of the incident photon in the GJ frame, as shown in Equation 6.3.3. For the H frame, the z-axis is opposite to the direction of the Lorentz boost to reach the frame (along the direction of Δ^+ in the center of mass) [82].

$$\hat{z}_{GJ} = \frac{\overrightarrow{P_\gamma}}{|\overrightarrow{P_\gamma}|} \tag{6.3.3}$$

In a right handed co-ordinate sytem, the direction x is the cross product of y and z.

$$\hat{x}_{GJ} = \hat{y}_{GJ} \times \hat{z}_{GJ} \tag{6.3.4}$$

The angles θ_{GJ},ϕ_{GJ} is used to denote the angles of the π^0 in this frame which will be discussed in next section.

6.3.2 SDMEs

As described in Chapter 5, the production of spin 3/2 Δ^+ in $\gamma p \to \eta\, \Delta^+$ are partially polarized in GlueX, which can be quantified in SDMEs. The asymmetry can be written in terms of W as

$$\Sigma = -\frac{1}{P_\gamma}\frac{W(\Phi = 0) - W(\Phi = \frac{\Pi}{2})}{W(\Phi = 0) + W(\Phi = \frac{\Pi}{2})} \tag{6.3.5}$$

When W(θ,ϕ,Φ) is integrated over the solid angle (θ_{GJ}, ϕ_{GJ}) and assuming uniform acceptance we get:

$$\Sigma = \frac{3}{2}\int \Big[\rho^1_{33} sin^2\theta_{GJ} + \rho^1_{11}\Big(\frac{1}{3} + cos^2\theta_{GJ}\Big)\Big]\epsilon(\theta_{GJ}, \phi_{GJ})d\Omega \tag{6.3.6}$$

Where $\epsilon(\theta_{GJ},\phi_{GJ})$ is the 2D efficiency in GJ frame and ρ^1_{33}, ρ^1_{11} are the SDMEs.

If the 2D efficiency is uniform everywhere:

$$\Sigma = 2(\rho^1_{33} + \rho^1_{11}). \tag{6.3.7}$$

If the 2D efficiency is non-uniform, then potentially a bias in our Σ will be introduced. Experimentally, because the Δ^+ decay may not be uniformly detected, this will result in a weighted integration over the decay phase space. This can unequally affect ρ^1_{33} and ρ^1_{11} and their relative weights and could also allow additional SDMEs to "infiltrate" the simple expression of Equation 6.3.7. Either of these effects would result in an extracted value of the asymmetry Σ that does not faithfully represent the reaction under study. This has to be fixed with an efficiency correction. Afterwards we would weight events distributed according to ρ^1_{33} so they get treated the same as ρ^1_{11}. Thus it is important to look into the 2D GJ angles efficiency plots.

The potential bias in Σ from regions where the efficiency is non-zero are reduced by weighting data by an additional factor of $1/\epsilon$, where ϵ is the efficiency for the particular event.

6.3.3 2D Angles Efficiency Study

MC simulated data for the 2018 dataset was used for producing the efficiency plots shown in Figure 6.5. The efficiency plots were plotted for both Gottfried-Jackson and Helicity frames. Since GJ angle plots retained slightly more area for θ and ϕ than helicity angle plots for all three t-bins (2% - 4% more), it was decided to do the rest of the study using GJ angle plots. The efficiency is produced using the reconstructed and thrown information. A 2D bin by bin smoothing option available in ROOT was also used for the plots shown in Figure 6.4.

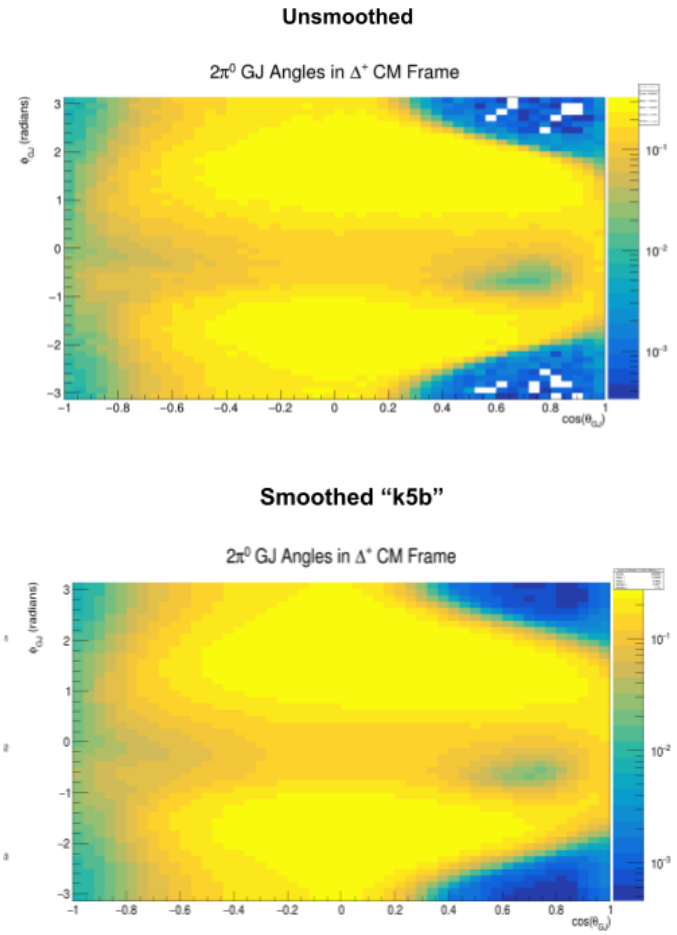

Figure 6.4: The x axis is $\cos\theta_{GJ}$, the y axis is ϕ_{GJ} in radians and the z axis (the color code shown on the right side scale) is on log scale. The top plot is unsmoothed while the bottom plot is smoothed using "k5b" option.

Here, TH2F::Smooth() function with "k5b" option was used, where the bin to be modified is placed at the center of a 5×5 grid of neighboring points. This is

to smooth bin contents using kernel algorithms similar to the ones used in image smoothing, where the sharp edges of pixels are smoothed using nearby pixel values. k5b is a bit more stronger in smoothing than other options such as "k3a" or "k3b" which has only 3×3 grid.

A non-uniform efficiency can be seen in the plots and also areas where there is near zero efficiency (corners of the plot marked by red dashed line boxes) in left plot of Figure 6.5. Check were done by varying the event selection cuts and its effect on the 2D plots. These are shown in Appendix B. As these plots are used for SDME bias correction, it is important to understand these regions and recover as much area as possible. The BCAL minimum shower energy was reduced to 50 MeV and this recovered the blank spaces in left region as shown in Figure 6.5 while reducing the blank space at $\cos\theta_{GJ} \approx 0.8$.

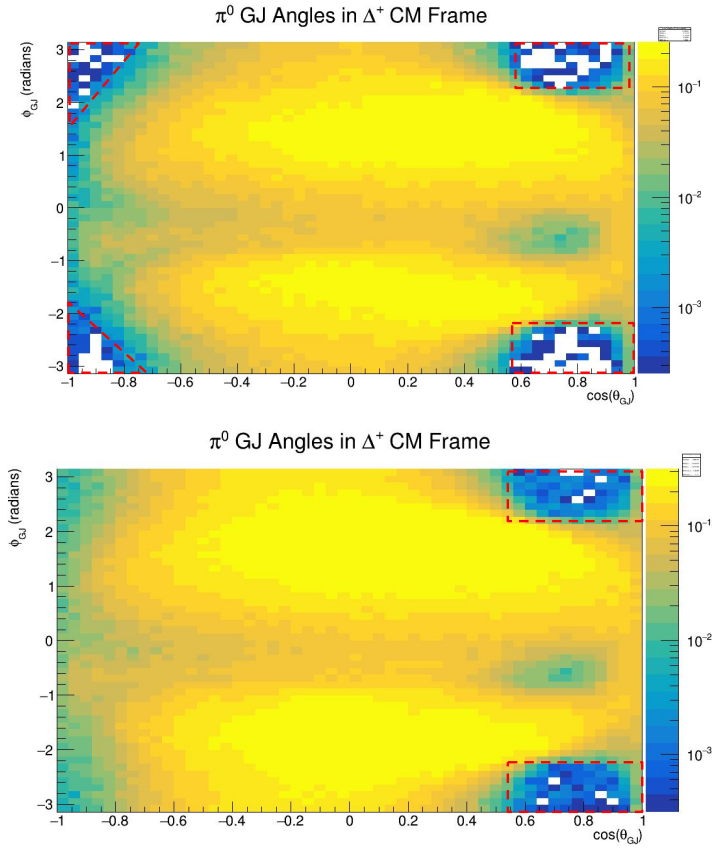

Figure 6.5: The top plot is with BCAL minimum shower energy =100 MeV and the bottom plot is with BCAL minimum shower energy = 50 MeV. The x axis is $\cos\theta_{GJ}$, the y axis is ϕ_{GJ} in radians and the z axis (the color code shown on the right side scale) is on log scale. The t bin used here is $0.2 < t < 1.5$.

The blank areas on right hand top and bottom corners were looked into by checking the thrown θ_{Lab} and ϕ_{Lab} in lab frame of the two photons of π^0. The angular distributions of one of the photons is shown in Figure 6.6

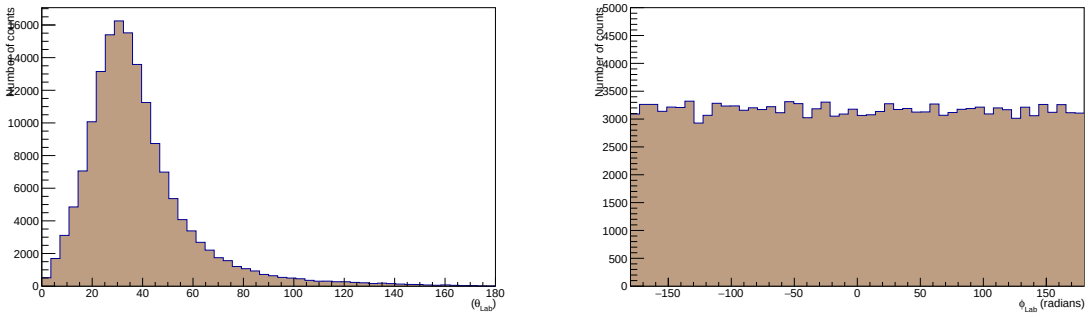

Figure 6.6: The left hand plot is thrown θ_{Lab} distribution and the right hand plot is ϕ_{Lab} distribution for one of the photons of π^0. x axis is in degrees, the y axis is the number of counts.

The distribution of angle between two photons was also checked and is shown in Figure 6.7.

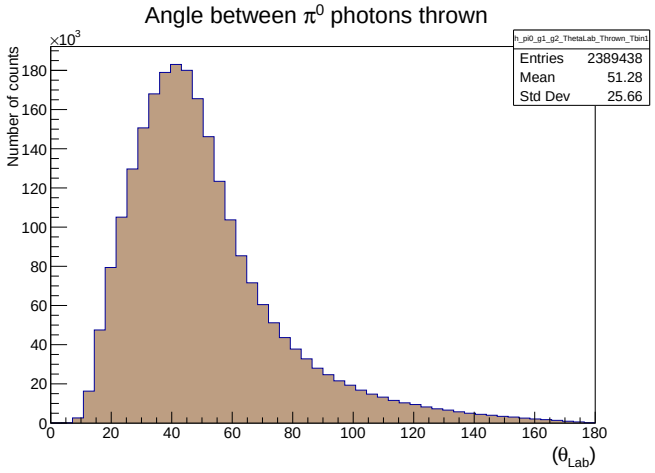

Figure 6.7: θ_{Lab} distribution between two photons of π^0. x axis is in degrees, the y axis is the number of counts.

The thrown information of proton angles and energy were also checked. The distributions are given in Figure 6.8. The distributions looks similar to that of the other regions of the efficiency map and did not have any anomalies. Any further information could not be inferred, which would help us to retrieve the near zero efficiency regions. The decision was taken to proceed in extracting Σ and assess the impact of these regions.

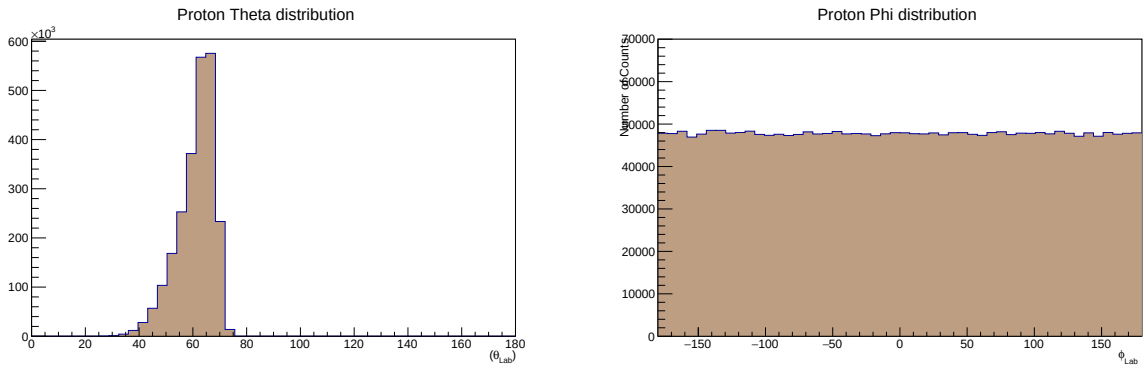

Figure 6.8: The left hand plot is thrown θ_{Lab} distribution and the right hand plot is ϕ_{Lab} distribution for the proton. x axis is in degrees, the y axis is the number of counts.

These plots are then used as efficiency maps for efficiency correction on the experimental data. This was done on an event by event basis. The factor of $1/\epsilon$ is used for the particular event where ϵ is obtained from the efficiency map. We also introduce a cutoff value of efficiency so that near zero efficiency regions will be excluded during efficiency correction. This cutoff value is treated as a systematic error and will be explained in the next chapter.

6.3.4 1D Efficiency Study

An efficiency was also applied to the $m_{\pi p}$ distribution. The ratio between accepted events and thrown events gives an efficiency plot for the $m_{\pi p}$ distribution as shown in Figure 6.9. The efficiency was calculated for the signal region between $1.1 < m_{\pi p} < 1.7$. The correction was applied on the line shape of Δ^+ and was done on a bin by bin basis.

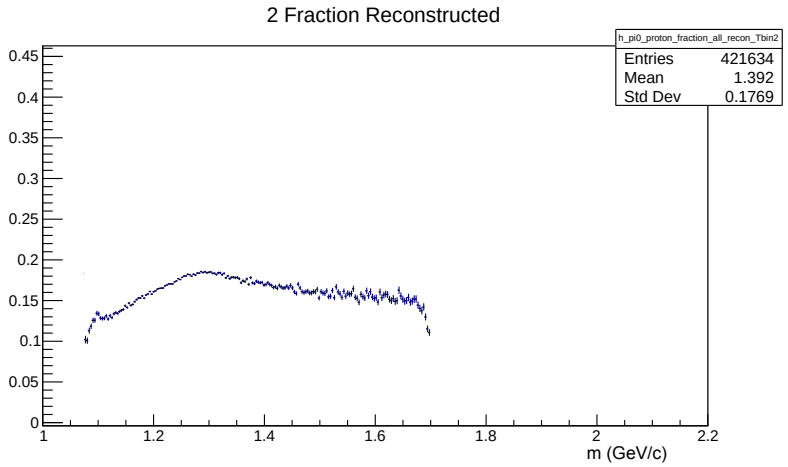

Figure 6.9: 1D efficiency plot for $m_{\pi p}$ distribution. The x axis is $m_{\pi p}$ in GeV/c and the y axis is the efficiency.

6.4 Validation of Statistical Uncertainty using Toy MC

An ideal statistical estimator is a minimum-variance unbiased estimator. Because we have relied on statistical approaches to extract the beam asymmetry Σ, we need to validate the the statistical properties involved to ensure that the method for extracting Σ is unbiased and therefore an accurate extraction for the reaction in this study. A common method for such cross checks is to simulate data from many toy experiments, analyze them and examine the variance of a large ensemble of toy experiments modeled to match our data. The study using toy MC here will prove that the moment-yield method is unbiased and a minimum-variance estimator.

Pseudoevents are generated randomly using a RooFit framework. ROOT provides with the RooFit library a toolkit for modeling the expected distribution of events in a physics analysis [83]. Each event is given a value of "mass" and a value for "phi". Here, mass values correspond to the $m_{\pi p}$ mass following the BW shape described in Equation 5.3.35. The value of ϕ assigned to pseudoevents is based on the equation for polarized pseudoscalar production in Equation 5.1.4 with a simple accept/reject algorithm. A few additional assumptions are made, which are as follows:

- It is assumed that the Σ asymmetry for the signal has a constant value and does not rely on $m_{\pi p}$, as would be predicted for the signal process. We additionally make the simplifying assumption that this asymmetry is constant across $m_{\pi p}$ when we add background components in the following section;

- Fixed known values for $P_{\perp}$ and $P_{\parallel}$ polarization are used. These can take any value from 0 to 1 and are assumed to be known precisely.

- For all polarization directions (PARA(0°), PERP0(90°), PARA(45°), and PERP(-45°)) events are generated. There are no additional offsets used, meaning that the orientation direction remains consistent with the nominal 0/45/90/-45° degrees. Following a Gaussian mean number of events N and standard deviation $\sqrt{N}$, the number of events in each orientation has a random distribution.

- The number of events that are generated is known prior to the accept/reject algorithm shaping the ϕ distribution. This is the same as measuring the flux experimentally.

- Here, resolution/accidentals are not modelled. The resolution is negligible in comparison to physical mass width of the Δ^{+} and log-likelihood fitting does not use utilize error bars which grow larger than sqrt(N) after accidental subtraction. Therefore this would not have a substantial effect on the analysis.

Exactly the same procedure as that of the experimental data was followed next. The moment weighted histograms as described in the previous chapter were obtained. First the $m_{\pi p}$ distribution is generated and is then weighed with the ϕ values. Then the combination of these histograms were taken to get the numerator and denominator histograms shown in Figure 6.10, which eventually were used to extract beam asymmetry values Σ_{Meas}.

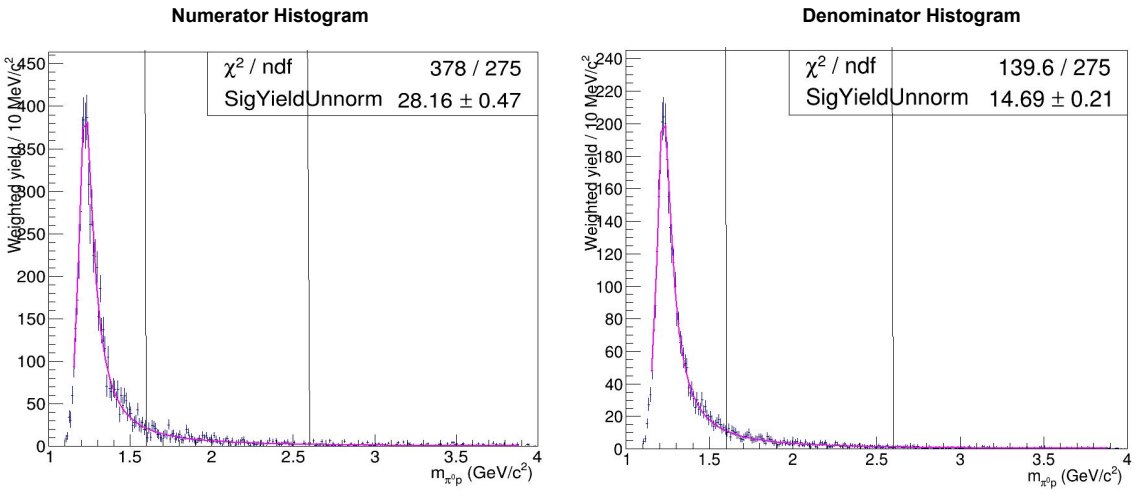

Figure 6.10: Numerator and Denominator histograms for a pseudo-experiment. The x axis is $m_{\pi p}$ in GeV/c and the y axis is the number of counts. The exclusion zone marked by the vertical lines is the same as that mentioned in Section5.3.38.

6.4.1 Pull Distributions

The next step was to fit and extract yields of histograms in each pseudo experiment. In order to check the statistical properties of the moment yield method, pull distribution as given in Equation. 6.4.1 was used,

$$\frac{\Sigma_{Meas} - \Sigma_{Input}}{\sigma_{stat}} \tag{6.4.1}$$

where, Σ_{input} is beam asymmetry value from data, Σ_{Meas} are extracted beam asymmetry values from pseudoexperiments, σ_{stat} - extracted uncertainty using the moment-yield method. According to the central limit theorem, if many pseudoexperiments are performed, then the pull should be a standard Gaussian distribution with a mean of zero and width sigma (RMS) equal to one. In this analysis, 1000 pseudo experiments were used for different t bins and both 0/90 and 45/135 orientations. One example is given in Figure 6.12. As shown in figure, the pull distribution results are Gaussian distribution centered around 0 indicating that it is unbiased and with RMS very

close to 1 indicating that the method used here is minimum variance estimator. The maximum deviation found with RMS was only around 10% for t bin 1.

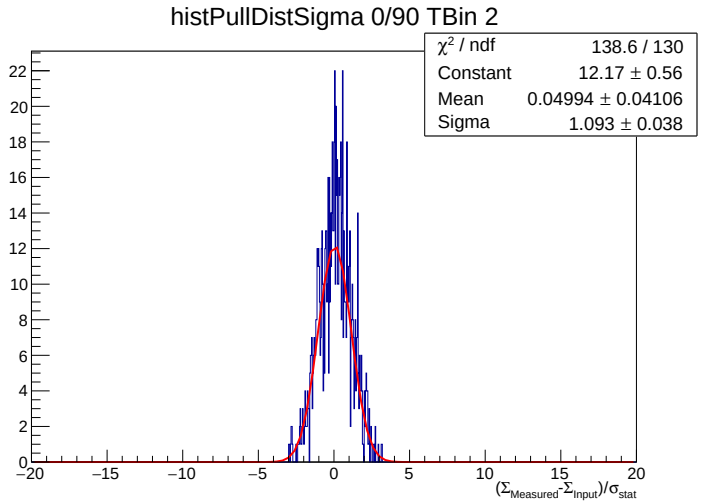

Figure 6.11: Pull distribution of 0/90 orientation. The x axis is Equation 6.4.1 and the y axis is number of counts.

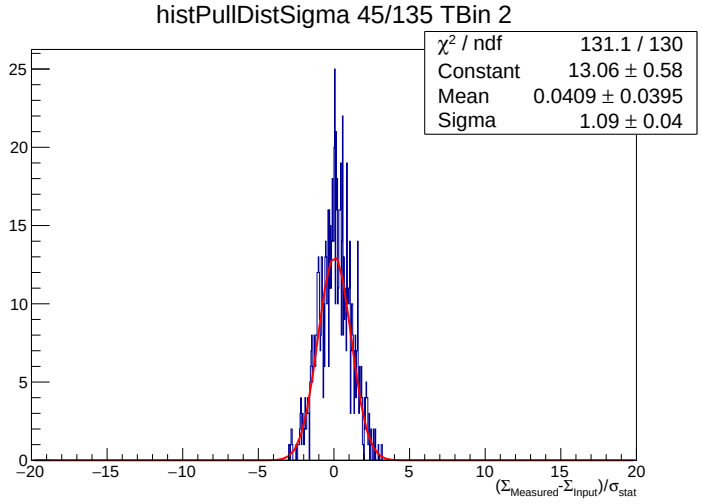

Figure 6.12: Pull distribution of 45/135 orientation. The x axis is Equation 6.4.1 and the y axis is number of counts.

Pull Distributions Including Background events

Additionally, the "pull" distributions to verify the statistical properties of the moment-yield determination are used by including the background. In this case, a background is added that imitates the shapes found in the data, the number of signal and background events and the asymmetries of the signal and background as determined by

the data are used as input. The background asymmetry is assumed to be constant as a function of $m_{\pi^0 p}$ for the purposes of this study. The process is repeated for both the 45/135 and the 0/90 datasets, and for each bin of t separately.

The shape of background events is determined from the results from the data using a set of nominal cuts. This helps to model continuum background shape over a wide range of $m_{\pi^0 p}$. The Δ^* components, which are difficult to accurately describe with their own yields and asymmetries, are avoided in this region. Then the background shapes are determined using a 4th order polynomial fit.

A background asymmetry is then calculated using the same method as for the signal asymmetry, using the integral of background shapes between 1.14 GeV/c^2 $< m_{\pi^0 p} <$ 3.2 GeV/c^2. We next fit the individual histograms of PARA (0°), PERP (90°), PARA (45°), PERP (135°) accidental subtracted invariant mass distributions to determine an estimate of the yields to use as input. A sample from one pseudo experiment and the actual distribution of data is shown in Figure 6.13.

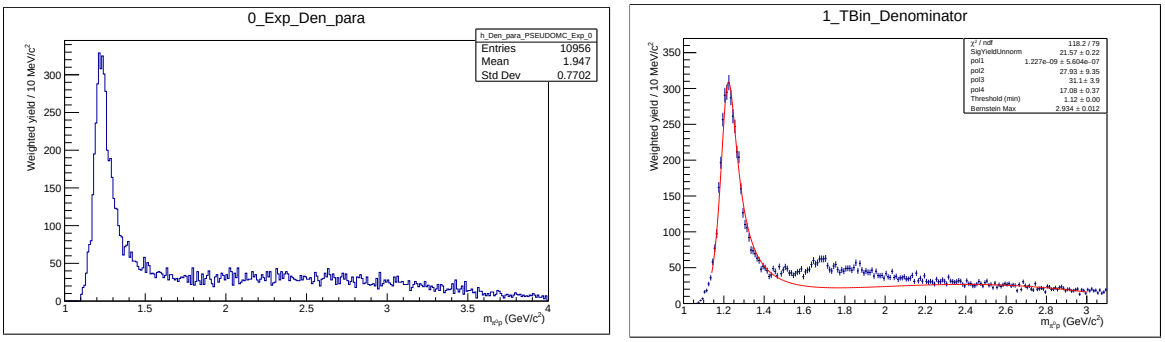

Figure 6.13: Left plot is a pseudoexperiment denominator histogram mimicking the experimental data plot given on the left. Right side plot is a fitted denominator histogram from experimental data. The x axis is $m_{\pi p}$ in GeV/c^2 and the y axis is the number of counts. The t bin used here is $0.2 < t < 0.35$.

An estimate of the signal asymmetry (taken from the nominal result), background asymmetry, and signal/background yields in a wide range of $m_{\pi^+ p}$ are obtained. The same method as described in the previous section is then used, and pull distributions are generated individually for each bin of t. The results were similar to the pull distribution results taken with just the signal and samples are shown in Figure 6.14 and Figure 6.15. They are also Gaussian distributed, centered around 0, indicating

that it is unbiased and with RMS very close to 1 indicating that the method used here is minimum variance estimator. The maximum deviation found with RMS was only around 12% for t bin 3.

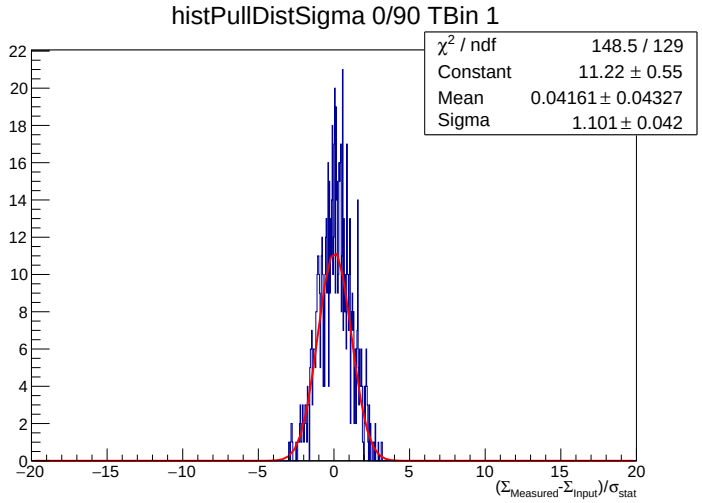

Figure 6.14: Pull distribution of 0/90 orientation. The x axis is Equation 6.4.1 and the y axis is number of counts.

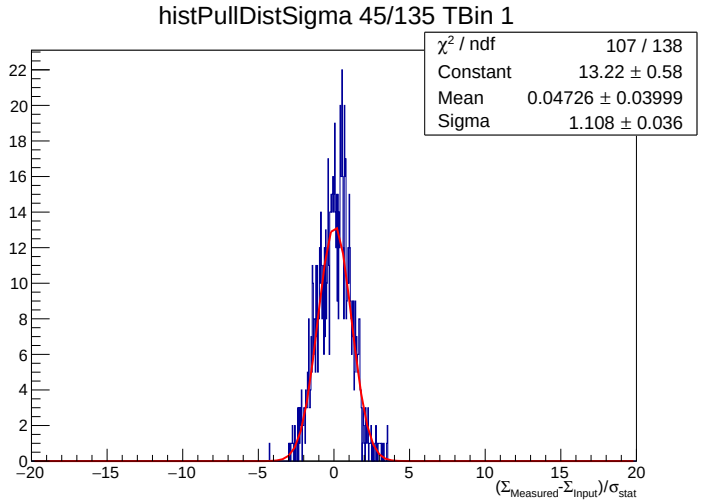

Figure 6.15: Pull distribution of 45/135 orientation. The x axis is Equation 6.4.1 and the y axis is number of counts.

Chapter 7

Results and Systematics

The event selection is described in Chapter 4, the analysis work flow is described in Chapter 5 and the simulations are described in Chapter 6. With these, all ingredients are available to extract the beam asymmetry values. First, the beam asymmetry was extracted using nominal values for the cuts, and this is termed the 'nominal' beam asymmetry, which was initially produced with only the statistical uncertainty. Subsequently, the cut values were varied in order to calculate the systematics on the beam asymmetry. The beam asymmetry was extracted separately for the two independent data sets, at 0/90 and 45/135 polarization orientation, and later combined into one result. Finally, the results with both systematic and statistical uncertainties are shown, and compared to theoretical predictions.

7.1 Results

We begin with recap of the event selection cuts and nominal values used.

- Binning of the histograms: 300 bins are used within the range of 1-4 GeV/c;
- Fitting range: $1.1 < m_{\pi p} < 1.6 GeV/c$ and $2.6 < m_{\pi p} < 3.2 GeV/c$. The mass range near Δ^*, N, N^* contributions, 1.6 to to 2.6 GeV/c^2 is always excluded from fitting;
- The efficiency correction has a cutoff, the nominal value used for the efficiency correction cutoff is 0.005;
- Line shape parameters: The Δ^+ lineshape parameters are fixed. These parameters include the B-W mass, mass width Γ_0 and the interaction radius;
- A fourth order of Bernstein polynomial (background) was used in the fitting;
- A 1D efficiency correction as a function of π^0 proton mass applied;
- Polarization angle offsets were applied from a high statistics GlueX sample of ρ meson, which will be described in later section. These values were used to account for the correction in the polarization values.

We also revisit the event selection cuts which are described in Chapter 4. Cuts on invariant mass of decaying π^0 and η were applied:

- Decaying π^0 : 0.125 GeV $<$ mass of π^0 $<$ 0.150 GeV;
- Decaying η : 0.50 GeV $<$ mass of η $<$ 0.60 GeV;

Additionally, we applied a cut on the 2D Dalitz plot described in Section 4.4.4. This cut was placed on the 4γ's of both η and π^0 together: $1.4142 < m_{\eta\pi^0}(4\gamma) < 2.45$ GeV/c^2. The $\pi^0 p$ mass distribution for the non-η side band was also checked and was found to contain a large background. These are shown in Appendix A, Fig A.1.

The Mandelstam-t distribution is given in Figure 7.1. Three t bins were used for the analysis. These bins were initially chosen to have roughly equal statistics. Additional studies were done by splitting the t bins finer and also changing the limits of the bins. These did not contribute any further information but reduced the statistics per bin and increased the statistical uncertainty. For example, by when the third t bin was split into two, the resulting beam asymmetry was in agreement between the two bins and ended just being averaged out.

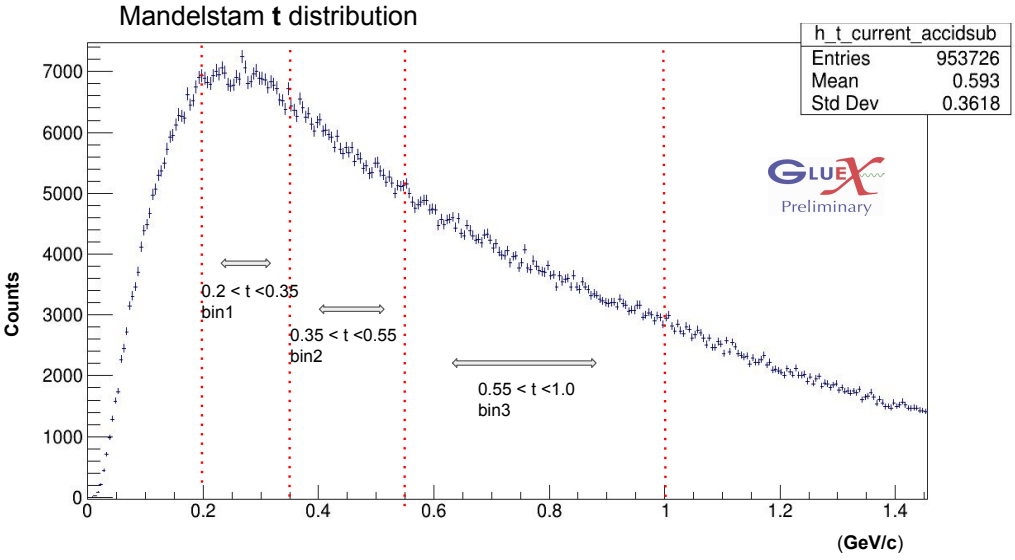

Figure 7.1: The Mandelstam-t distribution and the three t bins separated by red dotted lines are shown. The width of each arrow represents the RMS value of that bin.

The region below t= *0.2* GeV^2 was excluded from this analysis since it resulted in 2D angle efficiency plots that had extremely low efficiency regions, therefore necessitating very large corrections that inflated the errors. The distribution at t= *1.0* GeV^2 and beyond (Tbin 4) was also looked into and is shown below in Figure 7.2, to compare with the three t bins used in this analysis. The background is quite large in this case rendering the extraction method inapplicable, and thus this high t region was not used further in this thesis. For comparison the distributions for $t$bin 1, $t$bin 2 and $t$bin 3 are shown in Figure 7.3

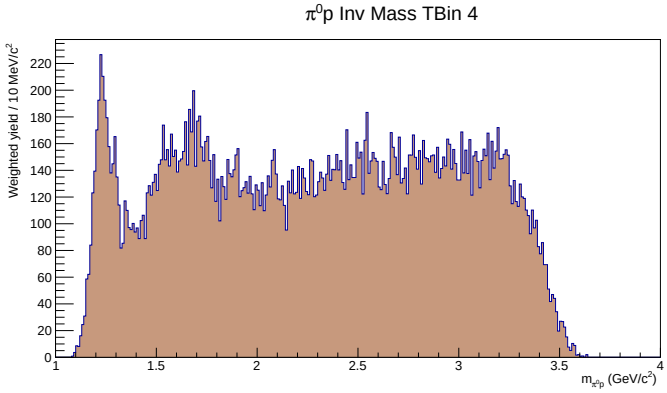

Figure 7.2: The invariant mass distribution $m_{\pi p}$ for t bin $1.0 < t < 1.5 GeV^2/c$.

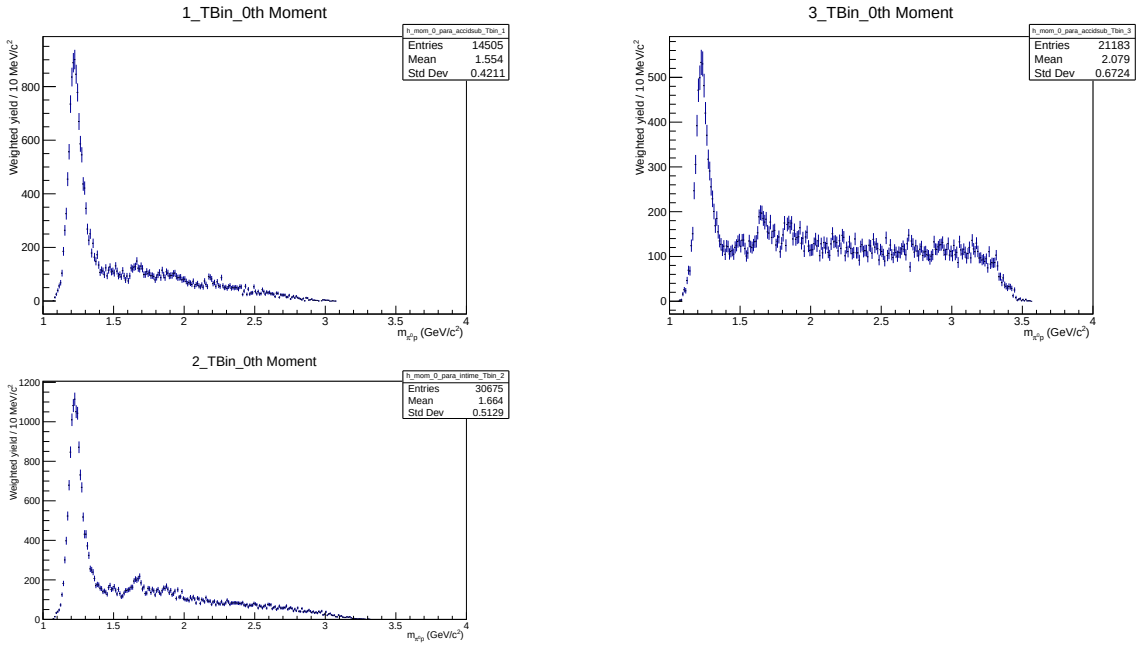

Figure 7.3: The top left hand plot is invariant mass distribution $m_{\pi p}$ for Tbin 1 distribution ($0.2 < t < 0.35 GeV/c$) and the top right hand plot is invariant mass distribution $m_{\pi p}$ for Tbin 3 distribution ($0.55 < t < 1.0 GeV/c$). The bottom plot is invariant mass distribution $m_{\pi p}$ for Tbin 2 distribution ($0.35 < t < 0.55 GeV/c$).

7.1.1 Numerator and Denominator for 0/90 and 4/135

Recall the key asymmetry, Σ, equations from Chapter 5, namely 5.3.12 and 5.3.13:

$$\Sigma = \frac{\tilde{Y}_2^{\perp} - \tilde{Y}_2^{\parallel}}{\frac{P_{\parallel}}{2}(\tilde{Y}_0^{\perp} + \tilde{Y}_4^{\perp}) + \frac{P_{\perp}}{2}(\tilde{Y}_0^{\parallel} + \tilde{Y}_4^{\parallel})} \tag{7.1.1}$$

It is useful to express the Moment-Yield expression for Σ as:

$$\Sigma = \frac{N}{D} \tag{7.1.2}$$

where

$$\begin{aligned} N &= \tilde{Y}_2^{\perp} - \tilde{Y}_2^{\parallel} \\ D &= \frac{P_{\parallel}}{2}(\tilde{Y}_0^{\perp} + \tilde{Y}_4^{\perp}) + \frac{P_{\perp}}{2}(\tilde{Y}_0^{\parallel} + \tilde{Y}_4^{\parallel}). \end{aligned} \tag{7.1.3}$$

So far we have used continuous integrals of ϕ for deriving the above expressions for moment-yields $Y_m^{\perp}$ and $Y_m^{\parallel}$, but the data used for the analysis is expressed in terms of finite bins of mass.

We also reproduce Equation 5.3.23 to show the terms that enter in the beam asymmetry Moment-Yield method; these terms will be graphed individually below, and separately for the 0/90 and 45/135 polarization orientations.

The variance of Σ in terms of N and D from Equation 7.1.2 can be expressed as

$$\sigma_{\Sigma}^2 = \Sigma \left\{ \frac{\sigma_N^2}{N^2} + \frac{\sigma_D^2}{D^2} - 2\frac{Cov(N,D)}{ND} \right\} \tag{7.1.4}$$

Clearly, we need three additional terms which include numerator variance σ_N^2, denominator variance σ_D^2 and covariance of numerator and denominator $Cov(N,D)$. These variance terms can be expressed as linear combinations of moment-yields $\tilde{Y}_m$.

$$\sigma_N^2 = \frac{1}{2N_{\gamma\perp}}\left(\tilde{Y}_0^{\perp} + \tilde{Y}_4^{\perp}\right) + \frac{1}{2N_{\gamma\parallel}}\left(\tilde{Y}_0^{\parallel} + \tilde{Y}_4^{\parallel}\right) \tag{7.1.5}$$

$$\sigma_D = \frac{P_{\parallel}^2}{4N_{\gamma\perp}}\left(\tilde{Y}_0^{\perp} + \frac{1}{2}\left(\tilde{Y}_0^{\perp} + \tilde{Y}_8^{\perp}\right) + 2\tilde{Y}_4^{\perp}\right) + \frac{P_{\perp}^2}{4N_{\gamma\parallel}}\left(\tilde{Y}_0^{\parallel} + \frac{1}{2}\left(\tilde{Y}_0^{\parallel} + \tilde{Y}_8^{\parallel}\right) + 2\tilde{Y}_4^{\parallel}\right) \tag{7.1.6}$$

$$Cov(N, D) = \frac{P_{\parallel}}{4N_{\gamma\parallel}}\left(3\tilde{Y}_0^{\perp} + \tilde{Y}_6^{\perp}\right) + \frac{P_{\parallel}}{4N_{\gamma\perp}}\left(3\tilde{Y}_0^{\perp} + \tilde{Y}_6^{\perp}\right) \tag{7.1.7}$$

An example plot with the fitting scheme is shown in Figure 7.4.

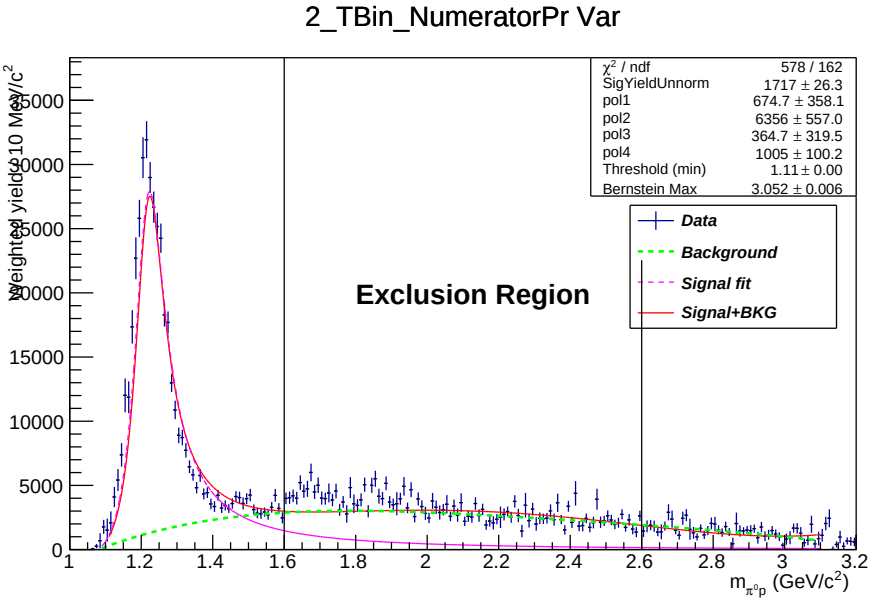

Figure 7.4: An example fit of numerator variance histogram. The signal, background and the total(signal+background) fits are shown by magenta, green and red lines, as indicated in the legend. The yields from the signal fit is used in Equations 7.1.2 and 7.1.4.

Plots of the Numerator, Denominator, their variances and their covariance for 3 tbins and for both 0/90 and 45/-35 are presented in Figure 7.5, Figure 7.6 and Figure 7.7.

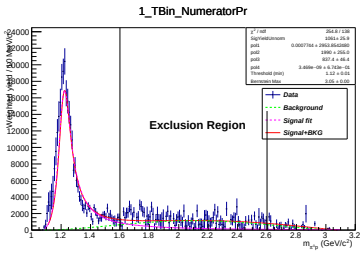

(a) Numerator 0/90

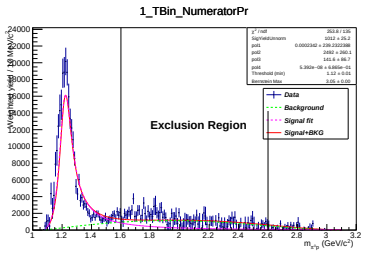

(b) Numerator 45/135

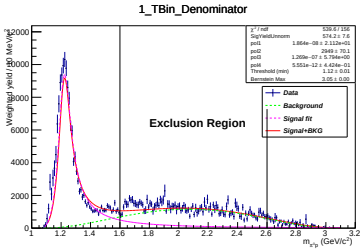

(c) Denominator 0/90

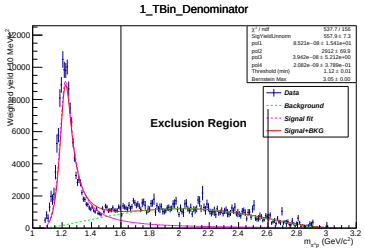

(d) Denominator 45/135

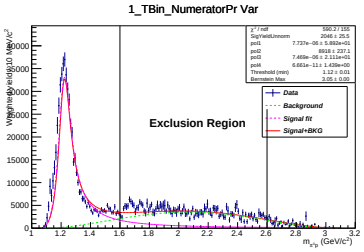

(e) Numerator variance 0/90

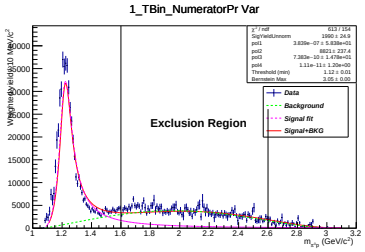

(f) Numerator variance 45/135

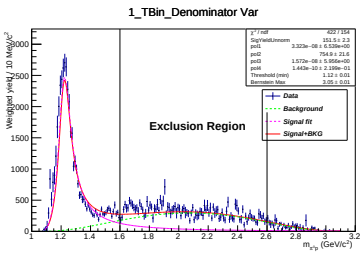

(g) Denominator variance 0/90

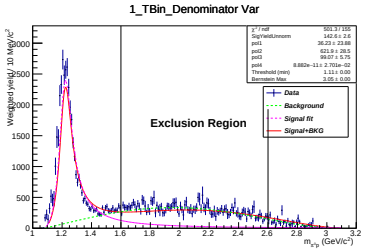

(h) Denominator variance 45/135

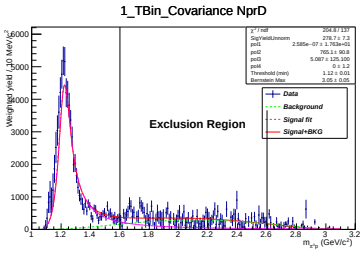

(i) Covariance 0/90

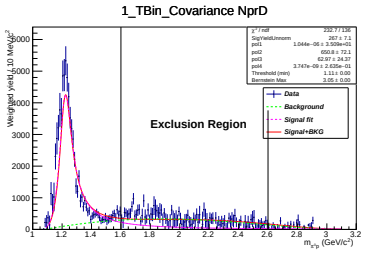

(j) Covariance 45/135

Figure 7.5: Histograms for the Numerator, Denominator, Numerator Variance, Denominator Variance and their Co-Variance for two orientations for TBin 1. The signal yields from the five histograms are used for extraction of Σ and its statistical uncertainty.

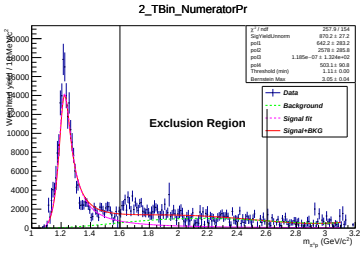

(a) Numerator 0/90

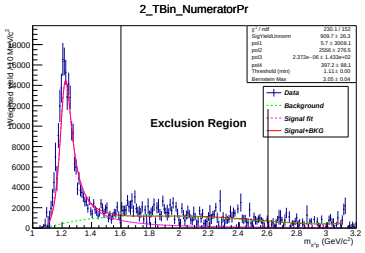

(b) Numerator 45/135

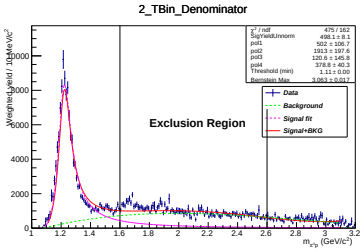

(c) Denominator 0/90

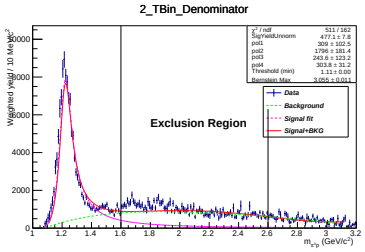

(d) Denominator 45/135

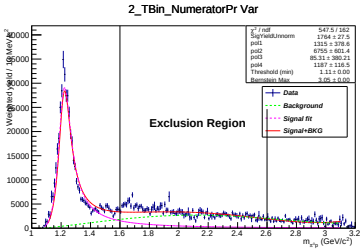

(e) Numerator variance 0/90

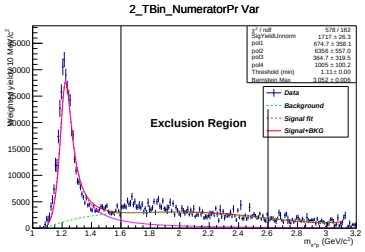

(f) Numerator variance 45/135

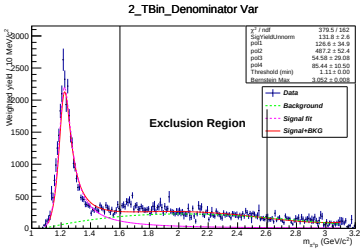

(g) Denominator variance 0/90

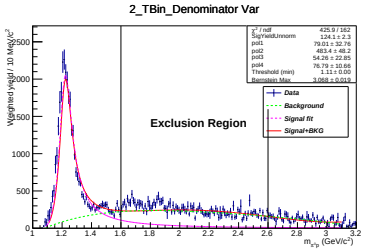

(h) Denominator variance 45/135

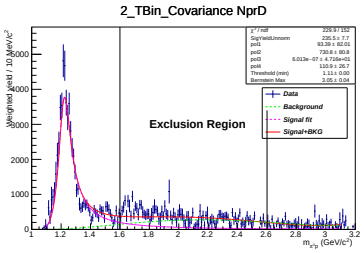

(i) Covariance 0/90

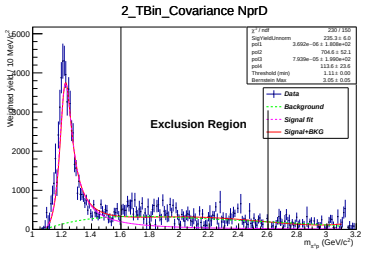

(j) Covariance 45/135

Figure 7.6: Histograms for the Numerator, Denominator, Numerator Variance, Denominator Variance and their Co-Variance for two orientations for TBin 2. The signal yields from the five histograms are used for extraction of Σ and its statistical uncertainty.

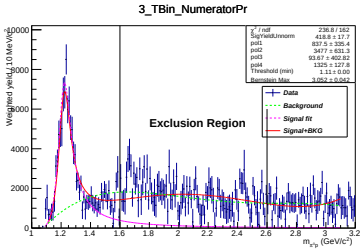

(a) Numerator 0/90

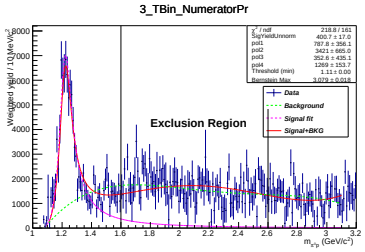

(b) Numerator 45/135

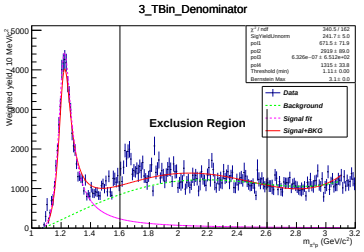

(c) Denominator 0/90

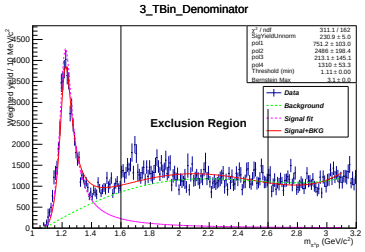

(d) Denominator 45/135

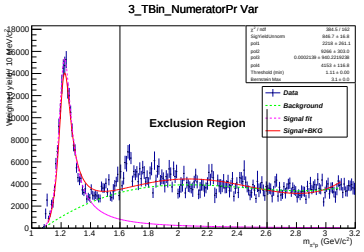

(e) Numerator variance 0/90

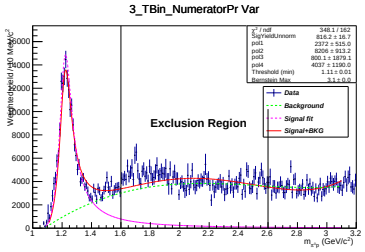

(f) Numerator variance 45/135

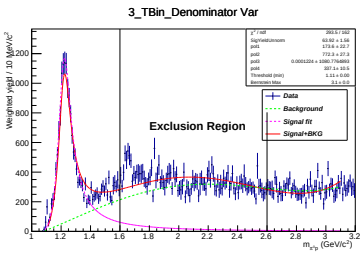

(g) Denominator variance 0/90

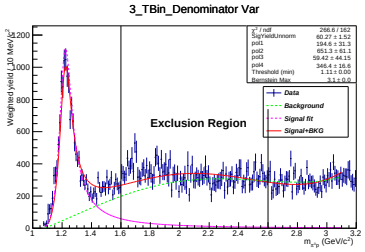

(h) Denominator variance 45/135

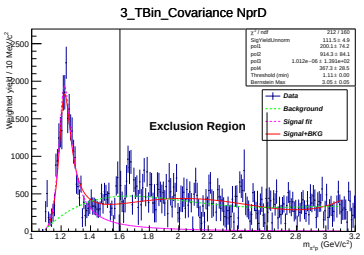

(i) Covariance 0/90

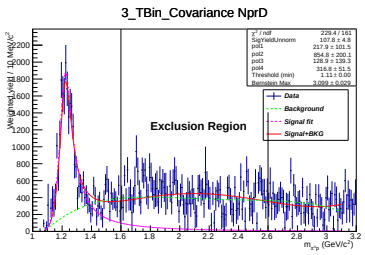

(j) Covariance 45/135

Figure 7.7: Histograms for the Numerator, Denominator, Numerator Variance, Denominator Variance and their Co-Variance for two orientations are shown here for TBin 3. The signal yields from the five histograms are used for extraction of Σ and its statistical uncertainty.

As expected, the five histograms for 0/90 look similar to their counterparts for 45/135 and no anomalies were observed. Overall, the fits looks reasonable as expected for the signal and background. We also assume that these two datasets are completely correlated, which can also be reasoned from these distributions as well. Usually the χ^2 /NDF is one way to tell the goodness of the fit. Although the χ^2 /NDF for these distributions are greater than 1, we are less concerned with it as we are taking the ratio of the yields from the fits. The signal shape and the fit also looks the same between numerator and denominator.

7.1.2 Nominal Results for 0/90 and 4/135

The results from the previous subsection for the 0/90 and 45/135 orientations allow the extraction of the beam asymmetry following Equation 5.3.13. The statistical uncertainties for each are extracted using Equation 7.1.4. The beam asymmetry values and statistical errors are shown in the Figure 7.8 below.

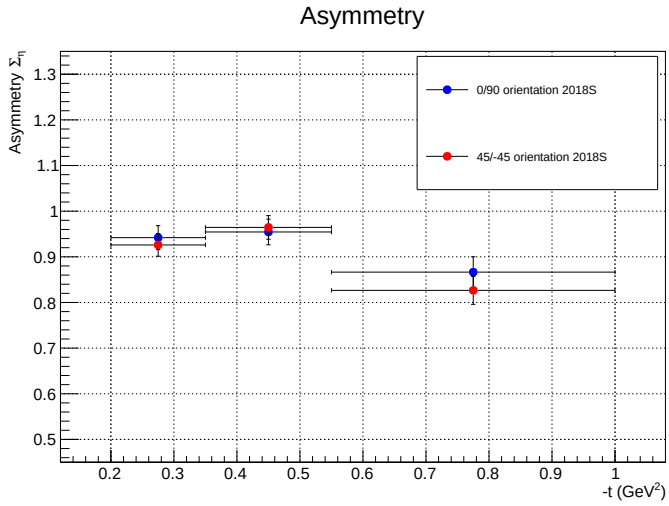

Figure 7.8: The results showing Σ values for both 0/90 and 45/135 orientations along with their statistical error bars.

Initially, the analysis was started with the 2017 data set that has about $\sim \frac{1}{3}$ of the statistics of the spring 2018 data data set, in order to establish the analysis cuts and work flow. The resulting preliminary plots were examined to ensure that method had been implemented correctly and did not result in unphysical values or

unrealistic error bars. Comparisons included several quantities, and as an example the mass distribution with other two periods are shown in Appendix A, Figure B.3. The increased fluctuations in these distributions are a result of the 2017 run period statistics. Even though the 2017 data set was processed and refined many more times that the spring 2018 data set by successive data production launches by the Collaboration, because the 2018 data has three times more statistics than 2017 it was selected for the final results as shown in Figure 7.8. The timeline of this work did not permit the analysis of the remaining fall 2018 data, which were also part of the GlueX Phase-I data set. As the tools to carry out that analysis have now been refined, this could followed up by others in the Collaboration. However, this is not expected since the increased statistics from such an effort will not alter the conclusion of this work, which has adequate statistical precision to demonstrate that the beam asymmetry of the $\eta\Delta^+$ channel resembles that from the ηp channel, as per theoretical expectations. This is discussed at the end of this Chapter.

7.2 Systematics

We checked for additional potential sources of systematic uncertainties. This is carried out by changing few of the cuts (one at a time) and checking if this affects the final beam asymmetry Σ_{nom} values. The estimate of the uncertainty of each individual cut $\boldsymbol{i}$, we carried out using the following equation:

$$\delta_i = \sqrt{\frac{\sum_{n=1}^{N}(\Sigma_{i,n} - \Sigma_{nom})^2}{N-1}} \tag{7.2.1}$$

where $\boldsymbol{n}$ indices all variations used within a particular study, with $\boldsymbol{N}$ representing the maximum total variations. These are carried out based on two assumptions:

- It is assumed that each of the several systematic checks is statistically independent of the others.

- It is assumed that these alternative evaluations deserve equal treatment and are

statistically fully correlated.

The uncertainties calculated so far are explained in the following subsections.

7.2.1 Signal Shape Variations

Δ^+ Shape Parameters

Although the precise mass parameters for the Δ^+ lineshape can be found in the Particle Data Group (PDG) [12], the mass parameters were allowed to float in the fit one at a time while finding the Σ to account for the likelihood of tiny distortions due to resolution or miscalibration effects. Thus, six additional evaluations of the uncertainty are made: two allowing the BW mass m_{BW} to vary by $\pm 10\%$ of the PDG value, two allowing the mass width Γ_0 to vary by $\pm 10\%$ of the PDG value, and two allowing the interaction radius to vary by up to $\pm 50\%$. This is done by allowing only one parameter at a time to float. The interaction radius was given greater flexibility than other parameters because it derives from an older measurement and has only a minor influence on the overall lineshape. The results of these three fits are input to Equation 7.2 to estimate any potential systematic contribution, with results listed in Table 7.1.

7.2.2 Efficiency Correction Effects

2D efficiency correction cutoff

The 2D efficiency plots described in Section 6.3.3 were used as efficiency maps for efficiency corrections. This was done on an event by event basis. The factor of $1/\epsilon$ is used for the particular event where ϵ is obtained from the efficiency map. We also introduce a cutoff value of efficiency so that near zero efficiency regions will be excluded from the efficiency corrections. This cutoff value was varied from 0.0025 to 0.0075 in steps of 0.0005 to study how it affects the σ values. The systematics obtained in this manner are listed in Table 7.1.

Lineshape Efficiency Correction

A binned efficiency as a function of $m_{\pi p}$ is obtained from the signal MC, as described in Section 6.3.4. After that, the fitted B-W signal shape is modified using this efficiency. This was done on bin by bin basis. The bins for both data and MC were matched for doing this. The fitted shape, rather than histogram entries, was modified so as not to distort error bars in data. This modification would not matter, so long as the signal shape is the same between numerator and denominator. Thus the effect of applying this correction was relatively very minor and is listed in Table 7.1.

7.2.3 Variations to Background Shape

In order to estimate the uncertainty due to background parameters, the order of Bernstein polynomial was varied between 5-8 and the effect was checked. Due to poor fits, polynomial orders 3 and below were not used further in the analysis. The results of these modifications were input to equation 7.2 to estimate any potential systematic contribution, and the results are listed in Table 7.1.

7.2.4 Varying Histogram Fit Range

The maximum value of the fit range was varied in order to assess how much effect this has on the background determination within the mass range of the Δ^+. The maximum fit range was varied from 1.35 to 1.6 GeV/c^2 and also from 1.6 to 3.3 GeV/c^2 in 50 MeV steps. The mass range near Δ^* contributions, 1.6 to to 2.6 GeV/c^2, is always excluded from fitting (these are shown by black bars on invariant mass plots shown earlier). By doing this study, we are also able to evaluate the effect of increasing of the exclusion region on either side i.e. below 1.6 and above 2.6 GeV/c^2 while doing one side at a time. The results of these modifications is input to Equation 7.2 to estimate any potential systematic contribution, with results listed in Table 7.1.

7.2.5 Histogram Binning effects

Although the pull distributions discussed in the previous chapter suggest that the B-W signal shape may not be sensitive to finite binning effects, the variation due to invariant mass histogram binning was studied here. The number of bins were from 100 to 500 in steps of 20. The nominal value is 300. The results are listed in Table 7.1.

7.2.6 Flux Normalization Factor

The GlueX Collaboration's previously extracted and published beam asymmetry measurements for π^0, η, and η' mesons [30] [31] indicate that a $\pm 5\%$ change to the normalization factor F_R due to uncertainties in flux determination is in fact a conservative value. The same estimate of uncertainty is applied here. The analysis is performed again multiplying the nominal F_R by a factor of 0.95 and by 1.05.

7.2.7 Polarization Angle Offsets

During running, the GlueX experiment aligns the diamond radiator such that the polarization direction corresponds precisely to ϕ=0/45/90/135° for respective datasets. However, the observed polarization direction may diverge from the planned polarization directions by $1^\circ - 4^\circ$.

The measured polarization angles were determined using a high statistics sample of ρ meson events [84] by collaborators. The goniometer system used allows for good run-to-run stability of the polarization direction, which is also verified in the same study.The following offsets are obtained from this study. We subtract the measured ϕ value in data by these values to shift the data to the desired orientations of ϕ=0/45/90/135°.

- PARA(0°) $\phi_0 = (1.77 \pm 0.04_{stat} \pm 0.56_{syst})^\circ$
- PERP(90°) $\phi_0 = (4.50 \pm 0.04_{stat} \pm 0.50_{syst})^\circ$
- PARA(45°) $\phi_0 = (2.85 \pm 0.05_{stat} \pm 0.53_{syst})^\circ$

- PERP(135°) $\phi_0 = (3.43 \pm 0.04_{stat} \pm 0.59_{syst})^\circ$

The offsets were removed and analysis was repeated. The upper and lower limits of uncertainty in angle offset were also included one at a time and their effect was checked. The results of these modifications is input to Equation 7.2 to estimate any potential systematic contribution and listed in Table 7.1.

7.2.8 Polarization Uncertainty

The statistical uncertainties from the TPOL determination of individual polarizations are used here. The following are the values of polarization and their uncertainty for the combined 2018 dataset obtained using Mike Dugger's V4 polarimeter measurements [44]:

- $P_{PARA(0^\circ)} = 0.3420 \pm 0.0063$
- $P_{PERP(90^\circ)} = 0.3474 \pm 0.0065$
- $P_{PARA(45^\circ)} = 0.3478 \pm 0.0063$
- $P_{PERP(135^\circ)} = 0.3517 \pm 0.0065$

Therefore, to very good approximation we assume in this section $P_\parallel \cong P_\perp \equiv P$. We then have

- $P_{0/90} = 0.345 \pm 0.0045$
- $P_{45/135} = 0.349 \pm 0.0045$

This allows us to rewrite the moment-yield expression for asymmetry Σ as:

$$\Sigma = \left(\frac{1}{P}\right) \frac{\tilde{Y}_2^\perp - \tilde{Y}_2^\parallel}{\frac{1}{2}(\tilde{Y}_0^\perp + \tilde{Y}_4^\perp) + \frac{1}{2}(\tilde{Y}_0^\parallel + \tilde{Y}_4^\parallel)} \tag{7.2.2}$$

The fractional uncertainty on Σ can then be expressed as:

$$\left(\frac{\sigma_{tot}}{\Sigma}\right)^2 = \left(\frac{\sigma_P}{P}\right)^2 + \text{everything else} \tag{7.2.3}$$

Therefore, the uncertainty on Σ from TPOL polarization is

$$\delta_{pol} = \Sigma \left(\frac{\sigma_P}{P} \right) \tag{7.2.4}$$

This uncertainty is listed in Table 7.1 along with others.

7.2.9 Combined systematics results

All the above individual uncertainties are added in quadrature to provide the final systematic uncertainty for each orientation. These were calculated separately for 0/90 and 45/135 and given in Table 7.1 and Table 7.2. Most of these are modification to fitting scheme. The largest of the systematics comes from the efficiency correction cutoff. No significant effect has been seen with the rest of the systematics and most are relatively minor.

Systematics	**TBin1**	**TBin2**	**TBin3**
Efficiency correction cutoff	0.0120	0.0134	0.0138
Signal parameters	0.0032	0.0043	0.0064
Background polynomial	0.0019	0.0015	0.0033
Polarization uncertainty	0.0096	0.0105	0.0093
Polarization offset	0.0015	0.0022	0.0041
Fit Range variation	0.0043	0.0041	0.0055
Binning value	0.0052	0.0033	0.0062
Flux normalization	0.0035	0.0059	0.0051
1D lineshape efficiency	0.0004	0.0004	0.0005
Total systematics	**0.0176**	**0.0191**	**0.0209**

Table 7.1: Individual systematics for both 0/90 orientation.

Systematics	**TBin1**	**TBin2**	**TBin3**
Efficiency correction cutoff	0.0118	0.013	0.0136
Signal parameters	0.0035	0.0042	0.0062
Background polynomial	0.0018	0.0017	0.0032
Polarization uncertainty	0.0099	0.0101	0.0093
Polarization offset	0.00147	0.0021	0.0043
Fit Range variation	0.0048	0.0039	0.006
Binning value	0.0054	0.0043	0.0042
Flux normalization	0.0038	0.0046	0.005
1D lineshape efficiency	0.0006	0.0004	0.0004
Total systematics	**0.0179**	**0.0187**	**0.0204**

Table 7.2: Individual systematics for 45/135 orientation.

7.2.10 Pull distributions

We have discussed in detail on the pull distributions from toy MC in Section 6.4.1 with data determined inputs including background shape and proved that the method is a minimum-variance unbiased estimator. The range of the RMS values observed with this study for all t bins is listed below in Table 7.3. Let f denote this measured RMS. This $\delta_{pullRMS}$ is equivalent to multiplying our measured statistical error by this factor f, when added in quadrature.

$$f^2\sigma_{stat}^2 = \sigma_{stat}^2 + \delta_{pullRMS}^2 \tag{7.2.5}$$

Solving for $\delta_{pullRMS}$, we find:

$$\delta_{pullRMS} = \sigma_{stat}\sqrt{f^2 - 1} \tag{7.2.6}$$

We add $\delta_{pullRMS}$, given in Table 7.3, to the measured statistical error in quadrature. An uncertainty resulting from a potential pull mean deviation from zero is also added. In the pull distributions, the pull mean is found to be very close to zero. At a maximum, the pull mean deviates from zero by a factor of $0.05\sigma_{stat}$. Denoting this

scale factor of statistical error by g, this multiplicative factor i.e. 5% of statistical uncertainty is very small and is ignored for the final results.

Pull RMS Error	**TBin1**	**TBin2**	**TBin3**
0/90	0.0108	0.012	0.0096
45/-45	0.0112	0.011	0.0102

Table 7.3: Pull RMS error $\delta_{pullRMS}$ for three$t$ bins and two orientations.

7.3 Final Results

Results from 0/90 and 45/135 data sets are statistically averaged here with errors propagated to the final result. The systematic errors for individual orientations are added in quadrature. However the final systematics are assumed to be fully correlated for two orientations and hence the error weighted average is taken. The final results are given below in Table 7.4 and plotted in Figure 7.9 and Figure 7.10.

t bin	**Σ**	**Statistical uncertainty**	**Systematic uncertainty**
$0.2 < t < 0.35$	0.949	0.024	0.017
$0.35 < t < 0.55$	0.979	0.026	0.019
$0.55 < t < 1.0$	0.856	0.031	0.021

Table 7.4: Table showing the final Σ results with combined statistical and systematic uncertainties .

The analysis herein is a continuation of the theory formalism and analysis technique implemented for the $\gamma p \to \pi^- \Delta^{++}$ beam asymmetry [32]. However, the initial expectation from theorists was that the beam asymmetry would be similar in the $\gamma p \to \eta p$ channel, for reasons expounded below. So far, theoretical inputs are provided by two groups, both are based on Regge models. In high-energy scattering

experiments like GlueX, the beam-target interaction is dominated by production and decays of mesons. Regge phenomenology underlies such processes and provides the theoretical framework for studying high energy scattering. In Regge theory, the angular momentum can take any complex value. The path taken in this complex plane is termed as Regge trajectories also referred as reggeons or Reggised exchanges [28]. Since the final state is the Δ^+ baryon of isospin 3/2, only the isovector mesons contribute to the reaction. Thus, both the models consider the vector meson ρ^0 and axial vector meson b_1 exchanges for the reaction. V. Mathieu, of the JPAC theory collaboration [85], took the model for $\gamma p \to \pi^- \Delta^{++}$ [28] and adapted it for $\gamma p \to \eta \Delta^+$, as the two reactions have the same recoil baryon with spin 3/2 incorporated into the formalism. The only exchanges allowed are the ρ and the b_1, since the exchange Reggeon must have $C = 1$ from the $\gamma\eta$ vertex, which forbids the pion exchange that dominated at small momentum transfer for the $\pi^- \Delta^{++}$ reaction. Additionally, exchanges must have $I = 1$ from the $p\Delta$ vertex, which forbids the ω exchange. This is unlike the otherwise analogous $\gamma p \to \eta p$ reaction as shown in Figure 1.14

Mathieu adapted the $\pi^- \Delta^{++}$ model to the $\eta \Delta^+$ final state and the beam asymmetry turns out very close to one, for both final states similarly to the $\gamma p \to \eta p$ reaction. If only the positive naturality ρ contributed to the reaction, we would expect to measure $\Sigma = 1$. If only the negative naturality b_1 contributed, Σ would be -1. This is because like ηp production there is no negative naturality pion exchange. But the b_1 is expected to be small and thus the dominance of the ρ exchange leads to an asymmetry ~ 1. Mathieu estimated the $\gamma - b_1 - \eta$ coupling by estimating the width $b_1 \to \gamma\eta$ using the known width $b_1 \to \rho\eta$ and using vector meson dominance to turn the ρ into a photon. This was done within the Regge-pole approximation. Other contributions, such as Regge cuts, could change these results but these are very difficult to estimate theoretically. Mathieu's calculations are shown for both his nominal model as well as one where the b_1 contribution has been multiplied by a factor of 10 at the level of the amplitude. The Yu-Kong group has also provided theoretical predictions using the same Regge formalism and exchanges [86]. The Yu-Kong group

has two versions of their model, as shown in Figure 7.9. The Regge propagator used contains a phase term, and these two versions either treat the ρ_0 and b_1 exchanges as having either a complex phase or non-degenerate one. The appearance of the deep dip at $t \approx 0.7\ GeV^2$ is due to the non-degenerate phase for the ρ Reggeon (solid curve, You-Kong 2).

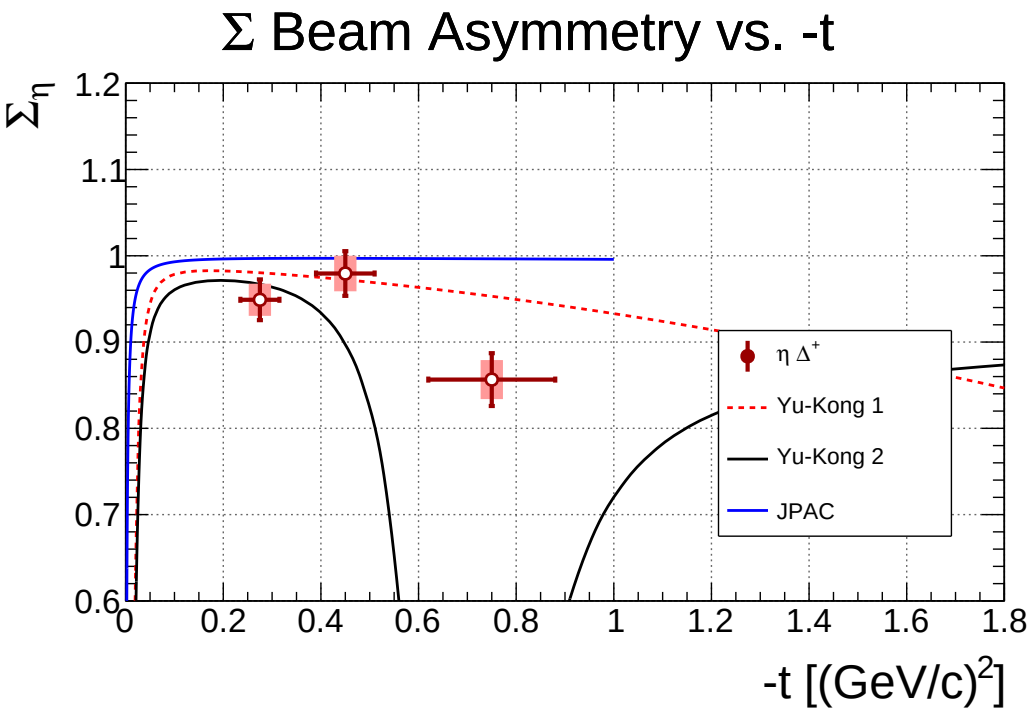

Figure 7.9: Beam asymmetry values Σ_η obtained using 2018 data. Horizontal error bars indicate t-bin width (RMS value). The theoretical curves (black and dotted red) are provided by the Korean theory group. Red-dashed results from both the ρ^0 and b_1 phases chosen complex, where as the solid curve represents the case of both the ρ^0 and b_1 non-degenerate phase. The x axis is t values, the y axis is Σ_η. Vertical error bars are statistical errors. Colored boxes indicate systematic errors.

The results obtained are not consistent with the two theoretical models in the higher t bin. The two models itself are not guaranteed to agree with each other, as choices regarding poorly or unconstrained parameters may differ, along with other subtleties.

Since the channel $\eta\Delta^+$ only differs with the channel ηp at the lower vertex, a comparison is done with previous ηp results as shown in Figure 7.10. The previous ηp results are discussed in Section 1.5.2. Theorists have often performed calculations of photoproduction off the neutron alongside predictions with a proton [87] [88]. This

allows one to infer the relative strength of isospin-0 compared to isospin-1 exchanges, e.g. ρ and ω exchanges. For the π^0 this led to a noticeable differences in predicted production off the proton compared to the neutron. This has not been measured with the required precision, as neutron targets are much more difficult to set up experimentally. This analysis offers an alternative to using a neutron target, thus requiring no changes to the experimental setup.

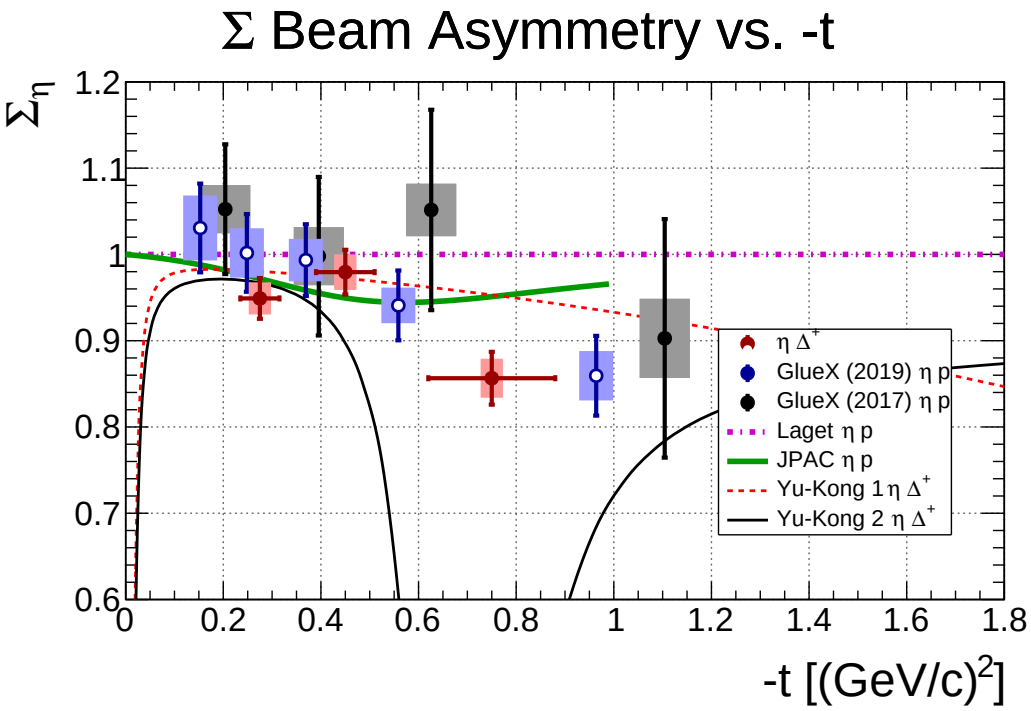

Figure 7.10: Comparison between the results of η Δ^+ (this analysis) and previous results on ηp channel as the JPAC theory Predicted Σ_η to be similar in both these channels i.e. close to 1.The x axis is t values, the y axis is Σ_η. Vertical error bars are statistical errors. Colored boxes indicate systematic errors. The various model predictions for ηp channel such as Laget and Goldstein are also included here.

The results look similar to ηp results, especially towards the higher t bin. The implications if the $\eta\Delta^+$ asymmetry is significantly different from that of the ηp would be difficult to address in theory. It could be due unexpected strangeness, re-scattering, or a breakdown of factorization in the reaction exchange. This could be investigated by looking into the $\pi^0 p/\Delta^+$ and $\pi^+ n/\pi^-\Delta^{++}$ as well to understand if the $\Delta \longleftrightarrow p$ substitution is responsible for the difference or if there is an alternate explanation. The results may help guide modifications to the theoretical models for production and exchange processes.

Similar efforts in beam asymmetry measurements of η and η', but with a recoiling proton, are being currently carried out by others in GlueX Collaboration. With the availability of more data, the previous works which were limited to lower t bins are now extended to higher t bins. The channels used in previous analysis of W. McGinley (CMU) and T. Beattie (U Regina) are extended in Mandelstam-t by T. Erbora and C. Paudel (FSU).

Specifically, the analysis of beam asymmetry for the η' channel is being carried out by C.Paudel using two decay modes: the neutral mode decay $\eta' \to \eta\pi^0\pi^0$ and the charged mode decay $\eta' \to \eta\pi^+\pi^-$; the latter channel has not been analyzed previously by GlueX. His preliminary results shows an agreement of $\Sigma_{\eta'}$ between the two channels and with the previous measurements. T. Erbora is carrying out an analysis on the beam asymmetry of η using neutral mode decay $\eta \to \gamma\gamma$ along with a cross check using charged mode decay $\eta \to \pi^+\pi^-\pi^0$. His preliminary results shows a trend of decreasing Σ_η with increasing Mandelstam-t values, similar to the results showed in this thesis.

Finally, it is noteworthy that the asymmetry for the previously published η proton and the $\eta\Delta^+$ channel in this work, show a decrease in the beam asymmetry at Mandelstam -$t$values greater than 0.4 $(GeV/c)^2$. This drop is not captured in either the JPAC or Yu-Kong-1 models, but it is present in the Yu-Kong-2 model. With the information at this stage, it is not possible to conclude specifics in the model parameters, but the hope is that this work will stimulate improved theoretical calculations in the future.

Chapter 8

Conclusions

8.1 Summary

The GlueX Experiment's principal aim is to study the spectrum of light mesons with special focus on exotic hybrid meson states. This thesis has covered the author's contribution to the ongoing effort of GlueX Collaboration towards this goal, both in service work and a major part as beam asymmetry study of η with a recoiling Δ^+. Understanding the production mechanism of the η meson is crucial, since they are present in many expected exotic meson decay channels.

The service work described in Chapter 3 included the BCAL LED monitoring and the SiPM DR study. The author has carried out the LED monitoring work from 2019 until 2022. Any anomalies observed while monitoring during these run periods were reported internally to the Collaboration and are well documented. The SiPM DR study was carried out by taking dedicated runs during different run periods (2019-2022). The study showed that the pedestal RMS increased over time indicating radiation damage and degradation of SiPMs, with studies ongoing by others. This study has been useful for selecting SiPMs of calorimeter for the Electron Ion Collider (EIC) experiment. The service work has been given over to another graduate student in the group.

The conventional method of directly fitting the angular distribution has been used for previous Σ of π^0 and η measurements published by GlueX. These measurements were done with a recoiling proton. On the other hand, the $\Delta^+ \to p\pi^0$ baryon is a wide, near-threshold resonance, difficult to separate from background. Therefore, a different approach was undertaken in this thesis, to extract the beam asymmetry in $\vec{\gamma}p \to \Delta^+\eta$ by using the Moment Yield Method, following its use in GlueX for the reaction $\vec{\gamma}p \to \Delta^{++}\pi^-$ by Jonathan Zarling [32]. Because the $M_{p\pi^0}$ invariant mass spectrum does not ensure a pure sample of Δ^+ events, one needs to integrate the signal fit function, to extract the moment-weighted yield of Δ^+ candidates. Any non-uniform azimuthal acceptance effects are removed by taking the difference of two orthogonal polarization directions and including the moment terms $Y_4^{\parallel}$ and $Y_4^{\perp}$.

The $\Delta^{++}\pi^-$ analysis [32] showed that this reaction can be explained theoretically by t channel exchange that requires pseudoscalar, vector and tensor components, to describe data up to $|t|$=1.2 (GeV/c)^2. On the other hand, the $\Delta^+\eta$ beam asymmetry behavior is expected to be similar to $p\eta$ and serve as a cross check on the factorization of the respective Feynman diagrams, which both have an η at the upper vertex, and a Δ^+ and a proton at the lower vertex, respectively.

Chapter 4 discussed the data analysis that was conducted which includes the event selection cuts. Chapter 5 provided a thorough explanation of the methodology that was employed. The Monte Carlo simulation studies utilized in the analysis were covered in Chapter 6.

By analyzing GlueX data from spring 2018 run period, the beam asymmetry measurements for the channel $\eta\Delta^+$ was carried out and the final results were shown in Chapter 7. The beam asymmetry final result is dominated by statistical uncertainty. The detailed study on systematics quantified cut variations and was also included in the final results. The results were compared with the previous ηp measurements. The comparison showed that the polarization transfer in η photoproduction does not depend on the lower vertex (i.e. if a spin-1/2 nucleon or a spin-3/2 Δ^+ is produced in the final state). However, the results showed a deviation from theoretical models of the $\eta\Delta^+$ especially towards higher t values. This may help guide modifications to these models for production and exchange processes involving η meson. In addition, the exotics π_1^+, π_1^0/η_1 are photoproduced via the same exchanges as the π^+ and π^0/η, respectively. Understanding the production mechanism for the latter reactions could help identifying exotic mesons, which is the main objective of GlueX.

Continuing analyses by students at FSU will extend the extraction of the beam asymmetry on the η and η' channels to considerably higher values of Mandelstam-t, than those accessed in this study or published GlueX results on the π^0, η and η' beam asymmetries. Of particular interest are deviations of the data from all these experiments at mid- to high values of t, which might prompt theorists to have a closer look at their models and the couplings therein. In conclusion, this work and those by

the FSU students will likely complete the GlueX effort on beam asymmetries of light pseudoscalar mesons, which started with the very first GlueX publication in 2017. Efforts now continue in the extraction of cross sections, Spin Density Matrix Element and Partial Wave Analyses.

Bibliography

[1] GlueX collaboration. H. Al Ghoul et al., first results from the GlueX experiment, AIP conf. proc. 1735, 020001 (2016).

[2] R. L. Workman et al. The Review of Particle Physics. In: PTEP 2022 (2022), p. 083c01. doi: 10.1093/ptep/ptac097.

[3] azoquantum-The standard model Accessed Feb 2023. https://www.azoquantum.com/Article.aspx?ArticleID=14.

[4] A. Salam S. L. Glashow and S. Weinberg. Nobel prize 1979 https://www.nobelprize.org/prizes/physics/1979/summary/.

[5] E. Rutherford. Collision of alpha particles with light atoms. iv. an anomalous effect in nitrogen. philosophical magazine, 90(sup1):31–37, 2010.

[6] J. Chadwick. The existence of a neutron. proceedings of the royal society a: Mathematical, physical and engineering sciences, 136(830):692–708, 1932.

[7] Wikipedia. https://en.wikipedia.org/wiki/Color_charge.

[8] D. Alan F. Halzen. Quarks and leptons: An introductory course in modern particle physics.

[9] M. Gell-Mann. 'The Eightfold Way: A Theory of Strong Interaction Symmetry.' California Institute of Technology, usa 1961.

[10] Wikimedia Commons. https://commons.wikimedia.org/wiki/File:Meson-octet.svg.

[11] Wikimedia Commons. https://commons.wikimedia.org/wiki/File:Baryon-decuplet.svg.

[12] R.L. Workman et al. (Particle Data Group). The Review of Particle Physics (2022), prog. theor. exp. phys. 2022, 083c01 (2022).

[13] Hall D / GlueX Technical Design Report. Gluex-doc 2442, 2014.

[14] G. S. Bali. Qcd potentiology, 2000.

[15] C. Mena. Quark-antiquark potentials in Non-perturbative models.

[16] J. Papavassiliou C.D Roberts J. Rodríguez-Quintero D. Binosi, C. Mezrag. Process-independent strong running coupling. *Physical Review D*, 96(5), September 2017.

[17] C.A. Meyer and E. S. Swanson. 'Hybrid Mesons.' Progress in Particle and Nuclear Physics 82, 21 2015.

[18] L. Liu et al. (Hadron Spectrum Collaboration). 'Excited and Exotic Charmonium Spectroscopy from Lattice QCD.' Journal of High Energy Physics 2012, 126 (2012).

[19] Guo Weiyi Y. Bi, Y. Xiao, Gong Ming, Peng Sun, Shun Xu, and Yi-Bo Yang. Lattice qcd gpu inverters on rocm platform. *EPJ Web of Conferences*, 245:09008, 01 2020.

[20] K.G. Wilson. The Origins of Lattice Gauge Theory https://doi.org/10.1016/j.nuclphysbps.2004.11.271.

[21] J. J. Dudek. 'The lightest hybrid meson supermultiplet in QCD.' Physical Review D 84, 074023 2011.

[22] N. Mathur P. Junnarkar and M. Padmanath. 'Study of Doubly Heavy Tetraquarks in Lattice QCD.' arXiv:1810.12285 (2018).

[23] J. Frison C. Hoelbling R. Hoffmann-S. D. Katz S. Krieg T. Kurth L. Lellouch T. Lippert K.K. Szabo G. Vulvert S. Durr, Z. Fodor. Ab initio determination of light hadron masses. Science. 2008 Nov 21;322(5905):1224-7. doi: 10.1126/science.1163233. PMID: 19023076.

[24] E. S. Swanson P. R. Page and A. P. Szczepaniak. 'Hybrid meson decay phenomenology.' Physical Review D 59, 034016 1999.

[25] R. Kokoski N. Isgur and J. E. Paton. 'Gluonic Excitations of Mesons: Why They Are Missing and Where to Find Them.' Physical Review Letters 54, 869 1985.

[26] A. Irving and R. Worden. Phys. Lett. C 34, 117 (1977).

[27] F. Low G. Chew, M. Goldberger and Y. Nambu. Phys. Rev. 106, 1345 (1957).

[28] JPAC. J. Nys et al. [Joint Physics Analysis Center], Phys. Lett. B 779 (2018).

[29] P. S. Zeits. f. phys. 178, 519 (1964).

[30] H. Al Ghoul et al. (The GlueX Collaboration). 'Measurement of the Beam Asymmetry Σ for π^0 and η Photoproduction on the Proton at E = 9 GeV.' Physical Review C 95, 042201 (2017).

[31] T. Beattie (GlueX Collaboration). 'Measurement of the Beam Asymmetry Σ for η and η' Prime Photoproduction on the Proton at Photon Energy of 8.8 GeV, GlueX-doc' 3829, 2018.

[32] S. Adhikari et al. (GlueX Collaboration). Measurement of beam asymmetry for π Δ^{++} photoproduction on the proton at E_γ=8.5 GeV GlueX Collaboration https://arxiv.org/abs/2009.07326v1.

[33] J. M. Laget. Phys. rev. c72, 022202 (2005).

[34] JPAC collaboration V. Mathieu. Private communication.

[35] A. Donnachie and Y. S. Kalashnikova. Phys. rev. c93, 025203 (2016).

[36] G. R. Goldstein and J. F. Owens. Phys. rev. d7, 865 (1973), g. r. goldstein.

[37] B.G. Yu and K.J. Kong. Private communication.

[38] S. Adhikari et al. The GlueX Beamline and Detector. 2020, arxiv:2005.14272.

[39] Hall D / GlueX Technical Construction Report. Gluex-doc 2511, 2017.

[40] Jefferson Lab. https://www.flickr.com/photos/jeffersonlab/ accessed 2022.

[41] B. Pratt. 'Diamond Radiator Fabrication, Characterization and Performance for the GlueX Experiment.' PhD thesis, University of Connecticut, 2017.

[42] A. E. Barnes. Development of the Tagger Microscope Analysis of Spin Density Matrix Elements for the GlueX Experiment. PhD thesis, University of Connecticut, 2017.

[43] M. Dugger et al. Design and construction of a high-energy photon polarimeter. Nuclear Instruments and Methods in Physics Research , 867(June):115–127, 2017. doi:10.1016/j.nima.2017.05.026.

[44] M. Dugger. https://userweb.jlab.org/ dugger/tripol/makepolvalsv5.tar.

[45] A. Sitnikov A. Somov S. Somov F. Barbosa, C. Hutton and I. Tolstukhin. 'Pair Spectrometer Hodoscope for Hall D at Jefferson Lab.' Nuclear Instruments and Methods A, 795, 376 2015.

[46] E. Pooser et al. The GlueX Start Counter Detector. Nuclear Instruments and Methods in Physics Research, 2019. doi:10.1016/J.NIMA.2019.02.029.

[47] A. Ostrovidov. TOF status. Technical Report GlueX-doc-3030, 2016.

[48] N. S. Jarvis et al. The Central Drift Chamber for GlueX. Nuclear Instruments and Meth ods in Physics Research, 962:163727, 2020. doi:10.1016/j.nima.2020.163727.

[49] L. Pentchev et al. Studies with cathode drift chambers for the GlueX experiment at Jefferson Lab. Nuclear Instruments and Methods in Physics Research, 845:281–284, 2017. doi:https://doi.org/10.1016/j.nima.2016.04.076.

[50] T. D. Beattie et al. Construction and performance of the barrel electromagnetic calor imeter for the GlueX experiment. Nuclear Instruments and Methods in Physics Research. 896:24–42, 2018.

[51] K. Moriya et al. "A measurement of the energy and timing resolution of the GlueX Forward Calorimeter using an electron beam". In: Nuclear Instruments and Methods in Physics Research Section A(2013),.

[52] J. R. Stevens. Status and Initial Performance of the GlueX DIRC. gluex-doc-5733-v1.

[53] A. Somov. Status of the L1 Trigger, GlueX-doc 3320, 2017.

[54] S. Boyarinov et.al. The CLAS12 Data Acqisition System, Nucl. In-2683 strum. Meth.In press (2020). doi:10.1016/j.nima.2020.163698.

[55] C. Kourkoumelis G. Voulgaris, P. Ioannou. Development of a Calibration System for the GlueX Calorimeter and TOF Detectors, GlueX-DocDB-1285.

[56] Z. Papandreou. History and Results of the Barrel Calorimeter Development, GlueX-DocDB-2245-v1.

[57] A. M. Foda et al. BCAL LED Tech Report, GlueX-DocDB-3191-v1.

[58] A. M. Foda et al. BCAL LED monitoring Spring 2019, GlueX-DocDB-5860-v1.

[59] E. Smith. Effect of Reflections on Pulse Integral, Peak and Attenuation Length Effect of Reflections on Pulse Integral, Peak and Attenuation Length, GlueX-DocDB-2622-v3.

[60] A. Somov. Addendum to fadc250 firmware specifications GlueX-DocDB-2776-v3.

[61] V. Neelamana. calorimetry meeting apr 16 2020. `https://halldweb.jlab.org/wiki/index.php/Apr_16,_2020_Calorimeter`.

[62] K. Suresh. calorimetry meeting jun 25 2020. `https://halldweb.jlab.org/wiki/index.php/June_25,_2020_Calorimeter`.

[63] K. L. Janzen. Optimization of Performance Parameters for Large Area Silicon Photomultipliers for use in the GlueX Experiment, M.Sc. Thesis, University of Regina, Regina, Saskatchewan, Canada, 2010.

[64] F. Barbosa et al. Nuclear Instruments Methods In Physics Research Section A (2011) doi: 10.1016/j.nima.2011.11.059. Silicon photomultiplier characterization for the GlueX barrel calorimeter.

[65] E. S. Smith. Development of Silicon Photomultipliers and their Applications to GlueX Calorimetry, GlueX Experiment Document 2913-v5.

[66] P. Degtiarenko et al. Calculation of Radiation Damage to Silicon Photomultipliers in GlueX Experiment, internal document (gluex-doc-1660, feb. 2011).

[67] Neutron irradiation tests are described at this link:. /https://halldweb1.jlab.org/wiki/index.php/SiPM_Radiation_Hardness_TestS.

[68] Github repository containing codes. https://github.com/JeffersonLab/hd_utilities/tree/master/BCAL_analysis.

[69] J. Stevens. https://halldweb.jlab.org/wiki-private/index.php/Spring_2018_Dataset_Summary,Accessed2023.

[70] R. T. Jones et al. Performance of the radphi detector and trigger in a high rate tagged photon beam, nuclear instruments and methods in physics research a 570 (2007) 384. doi:10.1016/j.nima.2006.09.039.

[71] S. Taylor. Gluex reconstruction https://halldweb.jlab.org/DocDB/0016/001650/002/gluex_recon.pdf.

[72] S. Taylor. Track Fitting in GlueX: Development Report V, GlueX-doc 1812, 2011.

[73] S. Taylor. Kalman filter https://halldweb.jlab.org/doc-private/DocDB/ShowDocument?docid=1253.

[74] P. Mattione. Least Squares Kinematic Fitting of Physics Reactions, GlueX-doc 2112, 2016.

[75] H. G. M. Santiago. Angular Distributions, Polarization Observables, Spin Density Matrices and Statistical Tensors in Photoproduction of Two Pseudoscalar Mesons off a Nucleon https://arxiv.org/abs/2102.13104.

[76] H. H. Bingham et al. Phys. rev. lett. 25, 1223 (1970).

[77] M. Dugger et al.(CLAS Collaboration). Phys. rev. c88, 065203 (2013).

[78] E. Pedroni et al. Nucl. Phys. A300, 321 (1978).

[79] E. Pedroni et al. Nucl. phys. a300, 321 (1978).

[80] Z. Baldwin. Generating Monte Carlo with examples 2021, GlueX DocDB.

[81] P. M. Eugenio. GENR8: A General Monte Carlo Event Generator V 1.0 GlueX DocDB.

[82] C. A. Meyer. Coordinate Systems in GlueX, GlueX Experiment Document 4829-v5.

[83] CERN. RooFit document, https://root.cern/manual/roofit/.

[84] A. Austregesilo. `https://halldweb.jlab.org/wiki-private/index.php/Spring_2018_Analysis_Launch`.

[85] . V. Matthieu. JPAC theory collaboration, Private communication 2023.

[86] B. G. Yu and K. J. Kong. Research Institute of Basic Sciences, Korea Aerospace University, Korea. Private communication 2023.

[87] G. Fox V. Mathieu and A. P. Szczepaniak. Neutral pion photoproduction in a regge model. *Physical Review D*, 92(7), October 2015.

[88] J. Nys, V. Mathieu, C. Fernández-Ramírez, A.N. Hiller Blin, A. Jackura, M. Mikhasenko, A. Pilloni, A.P. Szczepaniak, G. Fox, and J. Ryckebusch. Finite-energy sum rules in eta photoproduction off a nucleon. *Physical Review D*, 95(3), February 2017.

Appendix A

Additional invariant mass plots

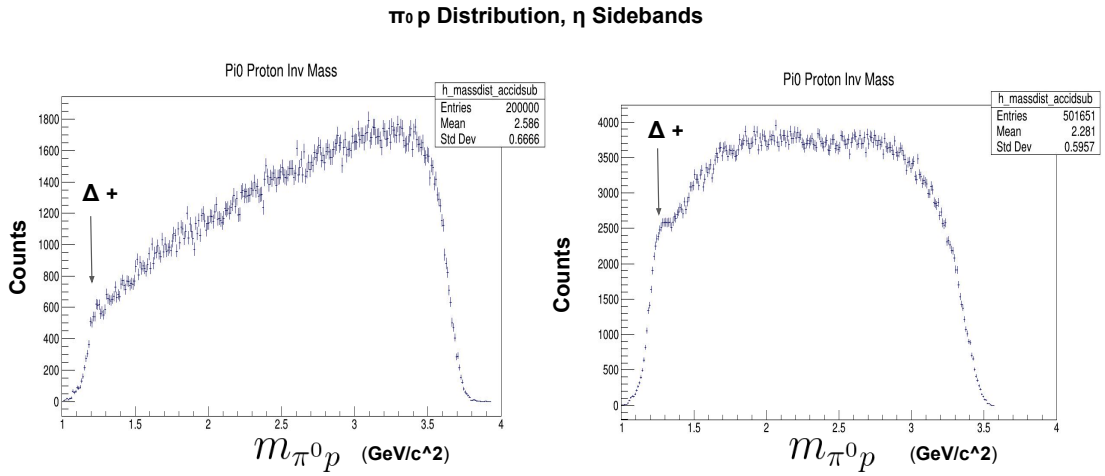

Figure A.1: The invariant mass distribution $m_{\pi p}$ for non η side band. The left plot is for η mass $< 0.5 GeV/c$ and the right plot is for η mass $> 0.6 GeV/c$. From the plots it can be seen that the non η Δ^+ background is large.

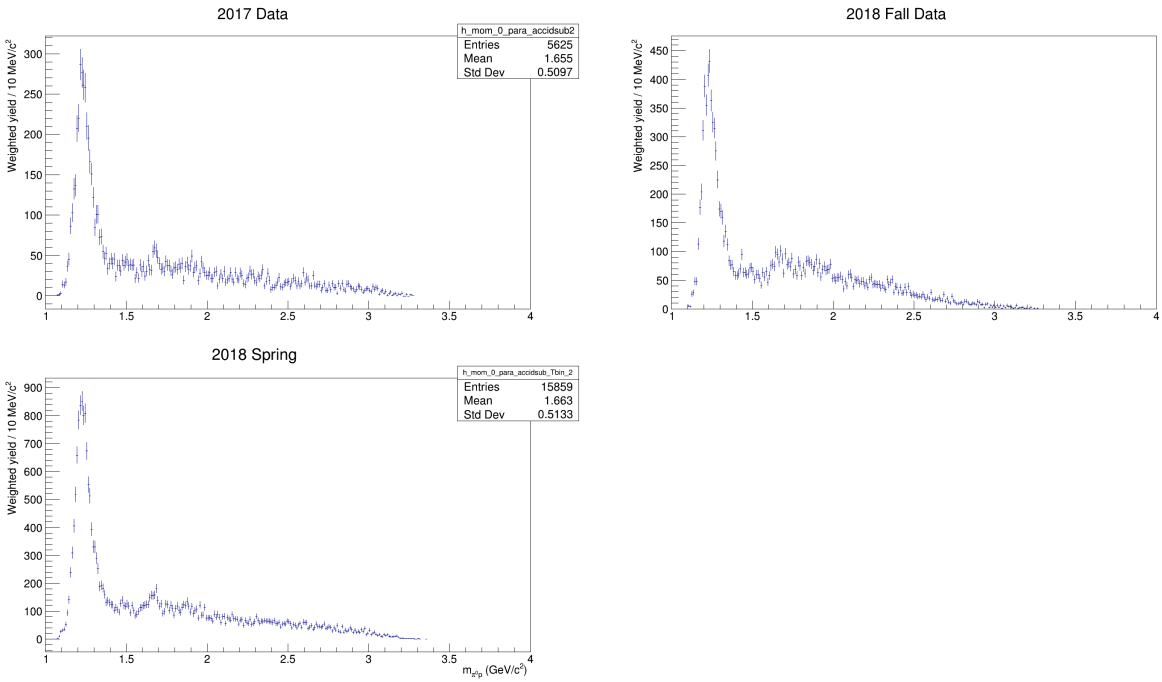

Figure A.2: The top left hand plot is invariant mass distribution $m_{\pi p}$ for 2017 data and the top right hand plot is invariant mass distribution $m_{\pi p}$ for 2018 fall data. The bottom plot is invariant mass distribution $m_{\pi p}$ for 2018 spring data.

Appendix B

Additional 2D efficiency plots

A non-uniform efficiency can be seen in the 2D efficiency plots and also areas where there is near zero efficiency. Initial checks were done by varying some of the event selection cuts and its effect on the 2D plots. Varying the cut on Dalitz plot (listed below) showed the major effect.

- Dalitz plot (Figure 4.7) cut on the 4γ's of both η and π^0 together: $1.4142 < m_{\eta\pi^0}(4\gamma) < 2.45\ GeV/c^2$;

Introducing this cut while other event selection cuts listed in Chapter 5 were kept at nominal values resulted in very low efficiency region at $\cos\theta_{GJ} \approx 0.8$ is shown in Figure B.1. The plots are shown below are with BCAL shower energy 100 MeV. As this cut is really important for including the signal region and reducing background, it was varied slightly to see the effect on the efficiency plots and are given below.

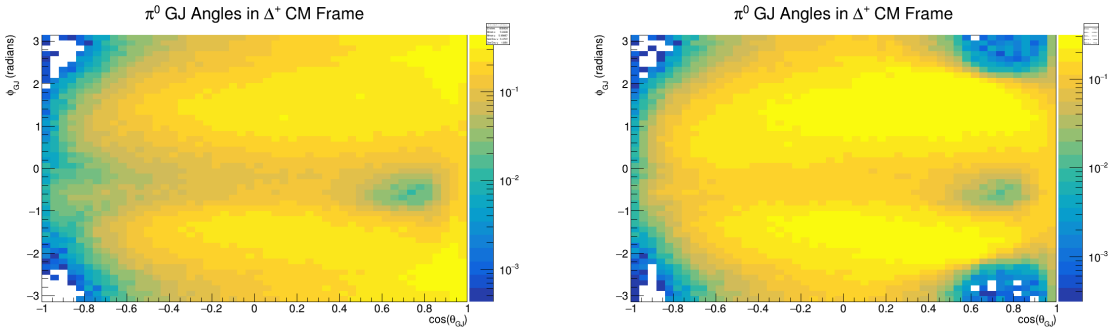

Figure B.1: The left plot is without the Dalitz cut, while the plot on the right is with the Dalitz cut. The x axis is $\cos\theta_{GJ}$, the y axis is ϕ_{GJ} in radians and the z axis (the color code shown on the right side scale) is on log scale.

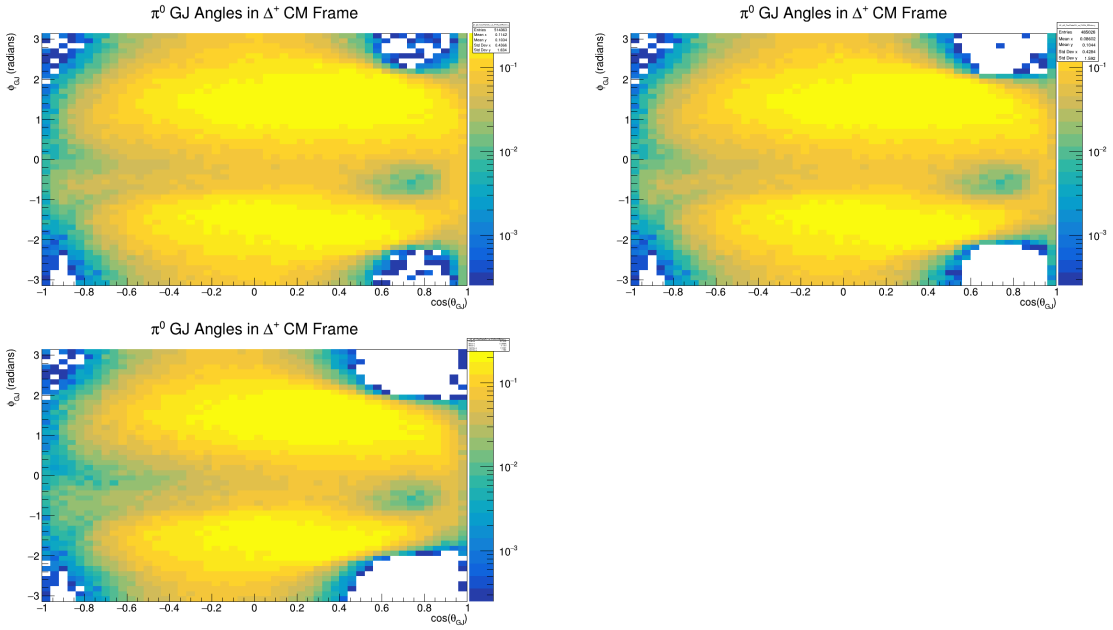

Figure B.2: The top left hand plot is for $1.3142 < m_{\eta\pi^0}(4\gamma) < 2.45 GeV/c^2$. and the top right hand plot is for $1.4142 < m_{\eta\pi^0}(4\gamma) < 2.45\ GeV/c^2$. The bottom plot is for $1.483 < m_{\eta\pi^0}(4\gamma) < 2.45\ GeV/c^2$.. The x axis is $\cos\theta_{GJ}$, the y axis is ϕ_{GJ} in radians and the z axis (the color code shown on the right side scale) is on log scale.

Then it was decided to use the cut value as $1.4142 < m_{\eta\pi^0}(4\gamma) < 2.45\ GeV/c^2$. In order to recover more area the minimum BCAL shower energy was lowered to 50 MeV and efficiency plots were obtained. They are shown below for three t bins and these are used for efficiency correction. It can be seen that most of the area is recovered the very low efficiency is reduced.

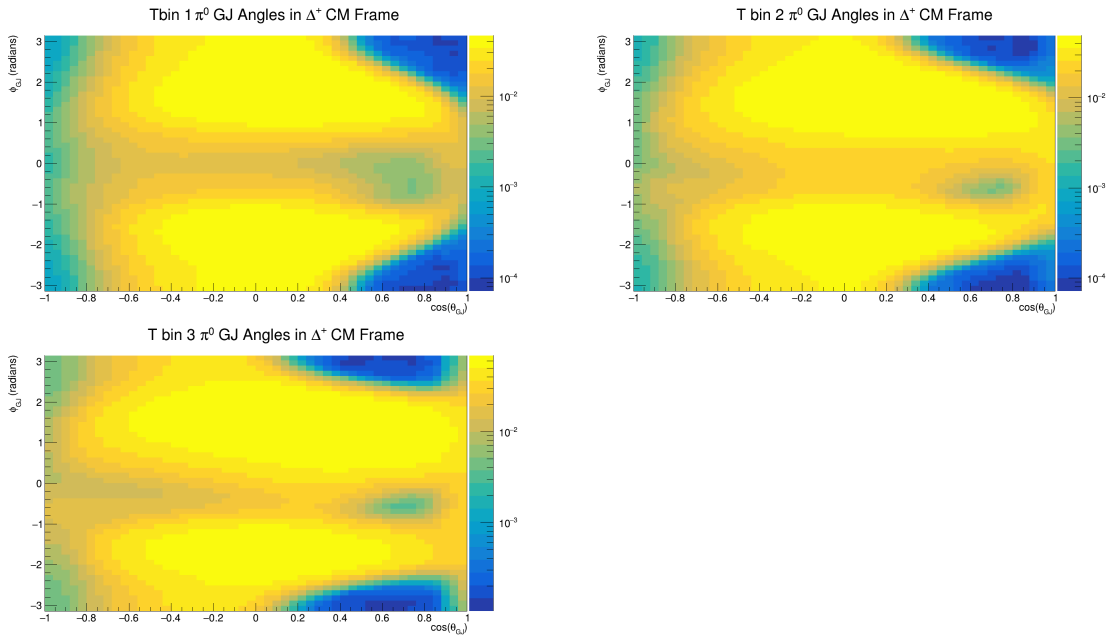

Figure B.3: The top left hand plot is for t bin 1 and the top right hand plot is for t bin 2. The bottom plot is for t bin 3. The x axis is $\cos\theta_{GJ}$, the y axis is ϕ_{GJ} in radians and the z axis (the color code shown on the right side scale) is on log scale.